Dissertations and Theses

9-2019

Hybrid Structural Composites with Energy Harvesting Capabilities

Simon Furnes

HYBRID STRUCTURAL COMPOSITES WITH ENERGY

HARVESTING CAPABILITIES

A Master Thesis

Submitted to the Faculty

of Aerospace Engineering

Embry-Riddle Aeronautical University

by

Simon Furnes

In Partial Fulfillment of the Requirements for the Degree of

Master of Science in Aerospace Engineering

September 2019

Embry-Riddle Aeronautical University

Daytona Beach, Florida

HYBRID STRUCTURAL COMPOSITES WITH ENERGY HARVESTING CAPABILITIES

by

Simon Furnes

A Thesis prepared under the direction of the candidate's committee chairman, Dr. Marwan Al-Haik, Department of Aerospace Engineering, and has been approved by the members of the thesis committee. It was submitted to the Office of the Senior Vice President for Academic Affairs and Provost and was accepted in partial fulfillment of the requirements for the degree of Master of Science in Aerospace Engineering.
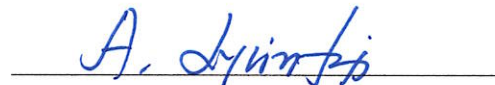
THESIS COMMITTEE

Chair, Dr. Marwan, Al-Haik

Member, Dr. Daewon Kim

Member, Dr. Sirish Namilae

Member, Dr. Fady Barsoum

Graduate Program Coordinator, Dr. Magdy Attia   9.19.2019
                                                             Date

Dean of College of Engineering, Dr. Maj Mirmirani   9/19/2019
                                                             Date

Senior Vice President for Academic Affairs and Provost, Dr. Lon Moeller   9/20/19
                                                             Date

ACKNOWLEDGMENTS

TABLE OF CONTENT

LIST OF TABLES

LIST OF FIGURES

SYMBOLS

m	meter
s	seconds
V	voltage
g	acceleration, m/s^2
μm	micrometer
A	ampere
Q & C	electrical charge, C=A·s
A	ampere
σ	mechanical stress, Pa
Pa	pressure, pascal
ε	mechanical strain
D	flux density, $\frac{C}{m^2}$
E	field strength, $\frac{V}{m}$
ϵ	dielectric permittivity
d	piezoelectrical coefficient, $\frac{m}{V}$ or $\frac{C}{N}$
$mmol$	milli molar concentration, $c = \frac{N}{N_A V}$, number of molecules N present in litre V of solution divided by N_A Avogadro constant
F	Farad, electrical capacitance, s^4·A^2·m^{-2}·kg^{-1}
Ω	ohm, electrical resistance
Z	Electrical impedance, Ωj
C_s	capacitance, F
R_{dc}	DC circuit resistance

R_s	series resistance, Ω
W	watt, power - $kg \cdot m^2 \cdot s^{-3}$
P	power, given in Watt
R_c	resistor added for current measurements, rated in Ω
Hz	hertz
f	frequency in Hz
ω	frequency in radians/s
E	Young modulus
v	Poisson ratio
$tan\ \delta$	dissipation factor

ABBREVIATIONS

PMN-PT	Lead Magnesium Niobate-lead Titanate
PZT	Lead Zirconate Titanate (Pb[Zr(x)Ti(1-x)]O3)
CF	Carbon Fiber
BaTiO3	Barium Titanate Oxide
NW	Nanowire
HFC	Hybrid Fiber Composites
FEA	Finite Element Analysis
FE	Finite Element
MBE	Molecular-beam epitaxy
PLD	Pulsed Laser Deposition
MOCVD	Metal-organic Chemical Vapor Deposition
HVPE	Hybrid-phase Epitaxy
MEMS	Microelectromechanical systems
PEH	Piezoelectric energy harvesting
NBT	*Na0.5Bi0.5TiO3*
BFO	Bismuth Ferrite
FRP	Fiber-reinforced polymer composites
DMA	Dynamic Mechanical Analysis
HFC	Hybrid Fiber Composites
ZnO	Zinc Oxide
SC	Single crystals
FC	Ferroelectric Polycrystalline

PbZr(.52)Ti(.48)O3   A specific PZT type

PMN–0.35PT $(1-x)Pb(Mg_{1/3}Nb_{2/3})O_3-xPbTiO_3$

PZT-5H   A specific commercial PZT type

PZT navy-II(5A)   A specific commercial PZT type

KNNTL:Mn   Chemical designation of a lead free piezoelectrical material

PMN-0.07PT   See PMN–0.35PT with more lead

NBT   Sodium Bismuth Titanate

FWF   Fiber weight fraction

FRF   Frequency Response Function

NOMENCLATURE

Hybrid materials	Composite materials consisting of two or more constituents included in the filler/binding material
Resin epoxy	Reactive polymers that act as a structural adhesive in fiber composites
Carbon fiber	cloth of fibers of about 5-10 μm composed of carbon
Glass fiber	Cloth of fibers made of glass
Finite Element Method	Numerical method where large systems are subdivided into smaller parts which are solved individually before assembled into a larger system equation for the whole system.
Piezoelectricity	Electrical charge released from certain types of materials after applying mechanical stress. Can be inverted where an applied charge generates a deformation of the material.
Multifunctional materials	See hybrid materials.
Energy harvesting	To capture energy from an external source and utilized it for a small device or storage
Material damping	A materials ability to dissipate a small and rapid changing external load
ANSYS®	Stands for Analysis System, a commercial Finite Element solver
Dielectric sensing	A material threshold for shift of charges due to an imposed mechanical load
Electrical charge	physical property of force experienced to materials when placed under an electromagnetic field
Crystalline solids/materials	Solid materials where molecules are arranged in a crystal lattice structure
Unite cell	Smallest group of particles in a material that form a repeating pattern of a crystal structure

Wurtzite unit cell	Crystal structure of various binary semiconducting compounds that due to its non-centrosymmetric are naturally piezoelectric
Constitutive equation	Equation describing the relation between two or more physical quantities
Rhombi crystals	Crystals consisting of 12 mirrored faces having four sides with similar lengths
Orthotropic materials	Subset of anisotropic materials, where material properties differ only along three mutually perpendicular axes of rotational symmetry
Micromechanics	The study of composite materials of the individual constituents that make up these materials
Curie temperature	Temperature where certain materials loses their magnetic properties
Strain	Measure of deformation between particles over a known length of a material
Flux density	The strength of a magnetic field for a certain point on a surface
Poisson effect	Measure of transverse l strain to axial strain compression for a material
Piezoceramics	Solid non-metal piezoelectrical material with highly oriented material characteristics
Ferroelectric	Certain materials that exhibit natural electric polarization that can be switched by applying an external electric field
Conductivity	How strongly a material resist or lead electric current
Hydrothermal growth/synthesis	Synthesis of crystals in an aqueous solution usually at elevated temperature where the weak pull of dipoles slowly grows materials in a crystal like pattern
Young modulus	Mechanical property that measure stiffness of a material
Tensile tests	Tension test of material in one direction
Elasticity modulus	see Young modulus

Open circuit voltage   Difference of electrical potential between two terminals when a device is not connected to any external load such as resistors

Short/ closed circuit   Circuit where current is allowed to travel a path with no to very low electrical impedance

Coherence   Statistics to examine the relation between to signals and estimate their causality (effect and cause)

ABSTRACT

Hybrid materials have received significant interest due to the potential enhancements they provide over traditional materials such as sensing, actuating, energy scavenging, thermal management, and vibration damping. While traditional materials can be utilized for either one of these functions or loadbearing, the hybrid materials are superior as they allow combination of a wide array of functionalities whilst being suitable for load-bearing purposes.

The goal of this thesis is to elucidate the synergistic effects of hybridization of two piezoelectric materials; zinc oxide nanowires (ZnO NWs) and thin film of lead zirconium titanate (PZT) on the mechanical and energy harvesting of beams made from plain-woven carbon fiber reinforced epoxy composites (CFRPs). ZnO NWs have, by contrast, displayed great promises. While not only being a very strong piezoelectric material, it enhanced the mechanical and dynamic properties of the composite due to the increased surface area and mechanical interlocking. However, the aspect of energy scavenging is somewhat limited due to the weak piezoelectrical effects of ZnO nanowires.

In this thesis, the prospects of ZnO NWs are exploited further to improve both their production processes and piezoelectric performance. Combining ZnO NWs grown on carbon fibers combined with other piezoelectrical materials has not yet been implemented but appears to be encouraging. This is the focus of this thesis. Despite that the composite comprising the combination of the two piezoelectric materials showed a minor drop in tensile strength and damping characteristics, the substantial gain in both stiffness (25.8 % increase compared to plain composite) and the electrical power gain (733.94 % more than that for ZnO NWs) is very promising for future application of the hybrid material into

real engineering problems.

A comprehensive study utilizing available commercial finite element software to simulate and foresee the behavior of hybrid materials was also carried out. The simulations agreed qualitatively with the experimental observations and explanations of the discrepancies between the model and experiment setup were discussed. Despite the preliminary promising results, more work is necessary to exploit the full potential of these material by optimizing the design of the energy harvesting devices and establishing more feasible models that treat the electromechanical coupling of these multifunctional hybrid composites more realistically.

1. INTRODUCTION AND LITERATURE REVIEW

1.1 Thesis Objectives and Outline

Hybrid materials, often called multifunctional materials, have received significant interest due to the potential enhancements they provide over traditional materials. These materials can be utilized for a wide variety of applications simultaneously and are, therefore, superior in most aspects to traditional one-function materials.

Functionalities such as sensing, actuating, energy scavenging, thermal management, and vibration damping can be collectively produced by a single material that is utilized in load-bearing structures. This is beneficial over materials providing single attribute such as piezoelectric ceramics which can only be utilized for some of the functionalities but are not suitable for load-bearing applications. Combining two or more materials have, however, shown great promises to counter these limitations and as well open a wide variety of new possibilities that we so far have only seen the beginning off.

The overarching goals of the thesis are to investigate the damping and energy harvesting performance of different hybrid fiber-reinforced polymer composites (FRPs) comprising carbon fibers and different morphologies of piezoelectric materials including zinc oxide (ZnO) nanowires (NWs) and lead zirconate titanate (PZT) films. The effects of the morphology of the piezoelectric phases are investigated.

ZnO NWs have shown great promise due to not only their piezoelectrical characteristics and ease of synthesis, but also due to their proven interfacial strengthening mechanisms for FRPs (Ayyagari, Al-Haik, & Rollin, 2018). On the other hand, PZT; a strong piezoelectric material with superior performance, has never been utilized in FRPs composites in the fashion shown in this research. Utilizing PZT thin

films together with ZnO NWs on carbon fiber could yield high-performance hybrid composite with excellent mechanical properties and energy harvesting capabilities.

This investigation comprises experimental and computational tasks. The experimental tasks entail the growth of piezoelectric nanomaterials over carbon fabrics and fabricating composites of these hybrid reinforcements. Mechanical characterization of these hybrid composites includes dynamic mechanical analysis (DMA), tensile testing, vibration damping and energy harvesting. The damping and energy harvesting experiments will be verified computationally utilizing the finite element (FE) analysis software ANSYS® (Ansys Inc., Pennsylvania, USA).

The outcomes of this research will lead to more efficient damping and higher energy harvesting materials. The research can pave the road to more efficient routes for incorporating the energy harvesting capability into standard structural composite structures such as beams, plates, and shells.

1.2 Thesis Outline

Chapter 1 provides a comprehensive review of the state of the art in energy harvesting materials and their working principles. Additionally, it gives a conceptual review of piezoelectrical materials and details the effects of combining different piezoelectric materials in terms of manufacturability, mechanical performances, and energy harvesting potentials.

Chapter 2 encompasses the experimental part where effort of producing ZnO NWs in more efficient ways is detailed. The effects of the different growth routes are elucidated through different tests for determining static and dynamical performances. The chapters also datils synthesis of pure PZT thin films and a ZnO NW coated with PZT thin

films.

Chapter 3 offers a closer look at the energy harvesting potential and utilization of the different materials outlined in Chapter 2. It starts with a short discussion on the design and optimal device/electric circuit combinations, before culminating into an examination of poling, measurements setups and methodologies for examining the performance of the devices over a wide range of vibration frequencies.

In Chapter 4, finite element analysis (FEA) for the energy harvester is carried out and compared to the experimental results in Chapter 3, different approaches to achieve better performance of the hybrid composites are discussed.

1.3 The Piezoelectrical Energy Harvester – A Brief Description

Vibration-based energy harvesting systems have been extensively studied for use with self-powered systems for the past two decades (Aridogan, Basdogan & Erturk, 2014). Such systems opened a wide variety of new possibilities as they eliminate the need of external equipment such as power sources, signal cabling and design considerations that adds weight, cost, and complexity to systems that demand both resilience and lightweight such as airplanes and space vehicles.

The added weight makes it unfeasible to implement many of the possibilities offered by microelectromechanical systems (MEMS) technology. Alternatively, energy harvesting technologies that scavenge energy available in forms of vibrations, heat, light, radiation, wind and hydrodynamic show great promises into miniaturizing MEMS further, making them safer, more robust and smarter due to better understanding of smart materials behavior (Dagdeviren et al., 2016), (Klingshirn, Meyer, Waag, Hoffmann, & Geurts, 2010); (Liu, Zhong, Lee, Lee, & Lin, 2018).

According to Liu, Zhong, Lee, Lee, and Lin (2018), there are three primary transduction mechanisms; namely: piezoelectric; electromagnetic; and electrostatic, that can be considered for energy harvesting application. Amongst these, energy harvesting with piezoelectric materials has received the most attention due to their higher energy density, inherent reciprocal conversion capability, and simpler architectures as compared to the rest. The article by Liu, Zhong, Lee, Lee, & Lin (2018), provides an extensive review into other potential architectures for energy harvesting.

Piezoelectric energy harvesting (PEH) technologies are used to extract kinetic energy from strain, vibration, and fluids, but in a very basic configuration, it usually consists of a cantilever beam, as shown in Figure 1-1. A tip load or a base excitation is applied to the beam making it deflect. This deflection induces strain through the section of the beam that can be utilized for electrical energy generation with a piezoelectrical material.
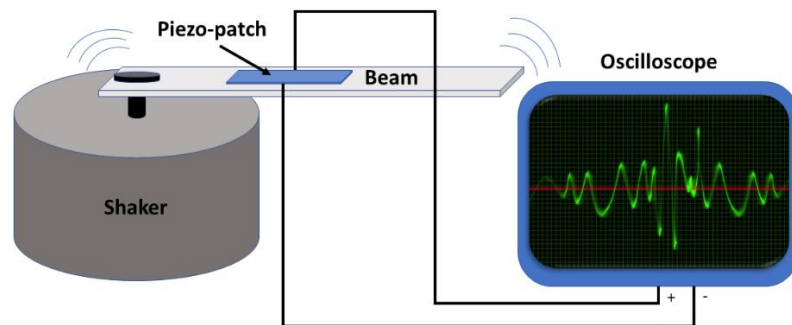
Figure 1-1. Illustration of a simple designed pizoelectric energy harvester where a piezo-patch glued to a beam induce electrical charge to a circuit due to mechanical strain

Deformation can be exploited with piezoelectric materials in a wide array of applications undergoing loads such as vibration, acoustics and other low-energy sources as long as the dielectric sensing of the piezo element is sensitive enough (Kang, Jung, Kang, & Yoon, 2016); (Priya, et al., 2017).

The performance of an energy harvester is not only determined by the piezoelectric properties but as also by the extension of the force providing the mechanical stimuli to the piezoelectric material. This discovery of these effects is largely contributed to Jacques and Pierre Curie work in the 1880's. They realized that when certain crystals are subjected to a mechanical force, they become electrically polarized. Tension and compression generated a voltage of opposite polarities, in proportion to the displacement or applied force. This behavior was named the piezoelectric effect; from the Greek word "piezein," which means press or squeeze (Kermani, Moallem & Patel, 2008).

Thanks to the work of Lippmann in 1881, (Priya et al., 2017) the converse of this relationship was confirmed by the Curie couple. Under exposure of an electrical field, the piezoelectric crystals expanded or shortened in accordance with the polarity of the field and proportional to the strength of the field. Simply put, the crystals can not only be used to generate an electrical force but can also be utilized inversely to produce mechanical power. This phenomenon was later formulated by Voigt, which soon after became the standard for understanding these phenomena (Voigt, 1910). Before going further into the overall formulation, a brief discussion on the atomic and molecular origins of piezoelectric materials is of importance.

1.4 Micromechanics of Piezoelectric Materials

To understand the piezoelectric effect, a closer look at the individual molecules that make up the crystal are necessary. Solid materials are made up of crystals, often referred as to crystalline materials (Hook & Hall, 2010). Some examples of such crystalline materials are iron, aluminum, silicon, rocks, ice, diamonds and others. These materials have an ordered arrangement of atoms or ions in their natural state and are

formed by repeating a symmetric pattern called unit cells in the space. The atoms residing

in these cells, as shown in Figure 1-2 for zinc-oxide (ZnO), are held together by various

covalent, metallic, or ionic bonds. Worth noting that the difference in material behavior

for the ZnO between the zinc-blende and the wurtzite unit cell where the first one

produces solid cubic of ZnO. Furthermore, for crystalline solids, we usually divide them

into three distinct groups of crystalline, polycrystalline, and amorphous where materials

such as metals and zinc oxide are polycrystalline.
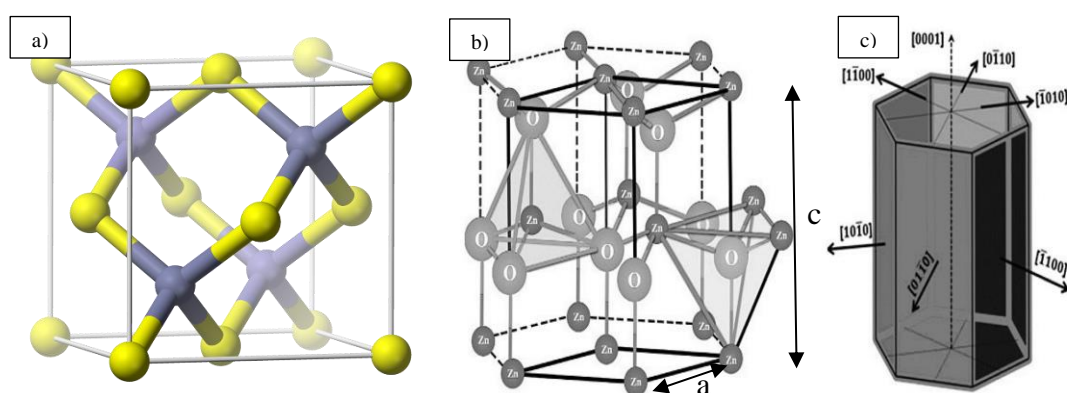
Figure 1-2. a) A zincblende unit cell (Wikimedia Commons , 2015) b) Hexagonal wurtzite crystal structure of ZnO, c) Hexagonal prism of ZnO crystal showing crystallographic faces. (Adegoke, et al., 2018)

For illustrative purpose, we will focus on the ZnO structure. The atomic bonding

is primarily ionic (Zn^{2+}–O^{2-}). As seen in the figure mentioned above, the ZnO crystal

structure has a tetrahedrally coordinated bonding geometry. The hexagonal wurtzite of a

ZnO is uniaxial and has a distinct axis called the c-axis. The axes in the plane

perpendicular to the c-axis and are called a-and b axes and are separated by 120° angles.

Interesting enough, as will be shown later, this nanoscale hexagonal structure would also

be predominant on the macro level seen upon hydrothermal growth. The orientation and

faces of wurtzite lattice are denoted by the Miller indices. For our ZnO structure the c-

axis is referred to as [0001] and the surface perpendicular to this axis as (0001) plane.

ZnO bond has a considerable degree of polarity caused by the very strong electronegativity of oxygen along the c-axis [0001] (Klingshirn, Meyer, Waag, Hoffmann, & Geurts, 2010). As can be seen in the wurtzite structure, the higher allocations of the oxygen atoms are in one of the tops or bottom planes perpendicular to the c-axis. This non-centrosymmetric crystal structure, together with the high polarity, gives rise to piezoelectricity. The work of (Wang 2004); (Klingshirn, Meyer, Waag, Hoffmann, & Geurts 2010) offer more details on the molecular level basis of piezoelectricity.

For other piezoelectric materials, identical molecules and micro-level setup are seen as well, but different types of atoms and structures may be driving the polarity. Other piezoelectric materials often utilized in industry and researches are Quartz, Lead Zirconated Titanite (PZT), Barium Titanite ($BaTiO_3$) and Polyvinylidene Fluoride (PVDF). However, the complete list of piezoelectric materials, considering weak piezoelectric materials are never-ending and expands over natural materials such as silk, bones, and a wide variety of semiconductors and polymers.

Piezoelectric materials are made up of ions or molecules with different polarization direction and setups, as presented in Chapter 1.4. In a piezoelectric material, the level of piezoelectricity is not only determined by the crystal type but also by how the molecules are arranged relative to each other. Each molecule has a polarization, where one side is more electrically charged than the other side (i.e., dipoles), where an imaginary polar axis runs through the molecule. As seen in Figure 1-3, in a single crystal will have all the polar axes point out along one direction, whereas in a polycrystal they will multipoles along different directions. In this situation, the polycrystal will have no

or a feeble piezoelectrical effect.
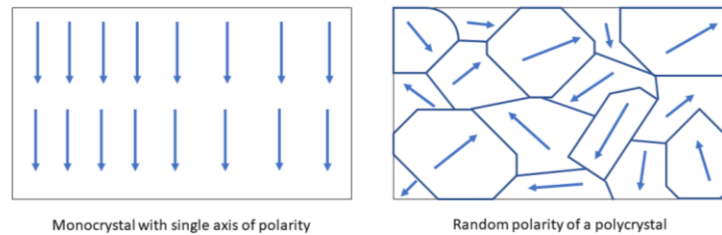
Figure 1-3. The difference between the polarity in a mono and a polycrystal.

Despite that a monocrystal has asymmetric polarization direction, it will not produce a net charge due to the molecule's atomic setups. Contrary to a polycrystal, which might with the help of heating at Curie temperature (Kermani, Moallem & Patel, 2008) poling could be utilized to arrange the crystals poles along the same direction as shown in Figure 1-4. This will produce a net polarity that can be exploited in polycrystalline piezoelectric material.
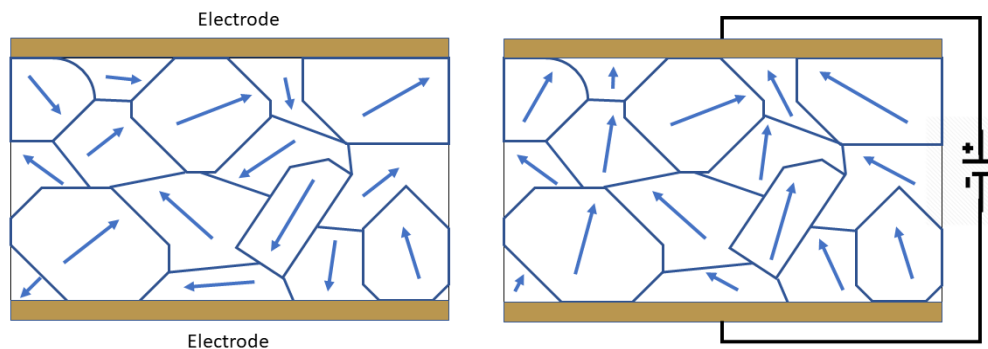
Figure 1-4. Illustration of change in polarity of a piezoelectric material after applying a DC electric field.

1.5 The Piezoelectric Effect: Constitutive Formulation

Even though Voigt formulated the piezoelectric phenomena first, the mathematics required to understand it was complicated and no viable applications were suggested prior to World War I, (Kermani, Moallem & Patel, 2008). One of the first applications was ultrasonic detector for submarines. Since then, piezoelectric materials found their

way in a growing array of applications such as: microphones; accelerometers; signal-filters; actuators; and so on.

The constitutive equations for piezoelectric materials were described by Lippmann (Lippmann, 2009), and later formulated into today's' standard in the field, IEEE (IEEE Standard on Piezoelectricity, 1988), based on the principle that for a piezoelectric material the electrical and mechanical constitutive equations are coupled as described in equation (1-1).

$$\begin{Bmatrix} \sigma \\ D \end{Bmatrix} = \begin{bmatrix} C^E & -d \\ d^T & \epsilon^{\varepsilon} \end{bmatrix} \begin{Bmatrix} \varepsilon \\ E \end{Bmatrix}$$
(1-1)

where σ denotes stresses and ε is the mechanical strain, the D ($\frac{C}{m^2}$) is the flux density, E ($\frac{V}{m}$) is the field strength. ϵ denotes relative permittivity, usually denoted by equation (1-2).

$$\epsilon = \bar{\epsilon}\epsilon_0 \text{ with } \epsilon_o = 8.855 \; x \; 10^{-12} \left(\frac{F}{m}\right)$$
(1-2)

For rhombic crystals and composites with orthotropic properties, the dielectric permittivity, matrix consists only of three entities, equation (1-3).

$$\begin{Bmatrix} D_1 \\ D_2 \\ D_3 \end{Bmatrix} = \begin{bmatrix} \epsilon_{11} & 0 & 0 \\ 0 & \epsilon_{22} & 0 \\ 0 & 0 & \epsilon_{33} \end{bmatrix} \begin{Bmatrix} E_1 \\ E_2 \\ E_3 \end{Bmatrix}$$
(1-3)

Furthermore, from equation (1-1) C stands for the stiffness matrix, and d for the piezoelectric coefficient matrix measured in $\frac{m}{V}$ or $\frac{C}{N}$ and relates strain to the electrical field.

Fully populated, for an orthotropic material that possesses polarization along the z-direction (see Figure 1-5), the constitutive equation are given by equation (1-4). Most common piezoelectric materials can be described as reasonably accurate as orthotropic,

and therefore this is considered for the future discussion. (Topolov, Bisegna & Bowen, 2018).

$$\begin{Bmatrix} \sigma_1 \\ \sigma_2 \\ \sigma_3 \\ \tau_{23} \\ \tau_{31} \\ \tau_{12} \\ D_1 \\ D_2 \\ D_3 \end{Bmatrix} = \begin{bmatrix} C_{11} & C_{12} & C_{13} & 0 & 0 & 0 & 0 & 0 & -d_{31} \\ C_{12} & C_{22} & C_{23} & 0 & 0 & 0 & 0 & 0 & -d_{32} \\ C_{13} & C_{23} & C_{33} & 0 & 0 & 0 & 0 & 0 & -d_{33} \\ 0 & 0 & 0 & C_{44} & 0 & 0 & 0 & -d_{24} & 0 \\ 0 & 0 & 0 & 0 & C_{55} & 0 & -d_{15} & 0 & 0 \\ 0 & 0 & 0 & 0 & 0 & C_{66} & 0 & 0 & 0 \\ 0 & 0 & 0 & 0 & d_{15} & 0 & \epsilon_{11} & 0 & 0 \\ 0 & 0 & 0 & d_{24} & 0 & 0 & 0 & \epsilon_{22} & 0 \\ d_{31} & d_{32} & d_{33} & 0 & 0 & 0 & 0 & 0 & \epsilon_{33} \end{bmatrix} \begin{Bmatrix} \varepsilon_1 \\ \varepsilon_2 \\ \varepsilon_3 \\ \gamma_{23} \\ \gamma_{31} \\ \gamma_{12} \\ E_1 \\ E_2 \\ E_3 \end{Bmatrix} \quad (1\text{-}4)$$

This equation can be simplified furtherly by considering planes of symmetry and different degrees of piezoelectric coupling. For instance, for a transversely isotropic material, the coupling is characterized by:

$$d_{32} = d_{31} \ \& \ d_{15} = d_{24} \quad (1\text{-}5)$$

This holds for the most used piezoelectric materials such as PZT and BaTiO$_3$, but other materials do not comply with this such as PMN-PT (Brockmann, 2009); (Kermani, Moallem & Patel, 2008).

Again, by observing the overall constitutive equation, some essential aspects can be realized. By applying a deformation (force) in the 3-direction, as shown in Figure 1-5, it is directly observable that the magnitude of flux density is governed by d$_{33}$.
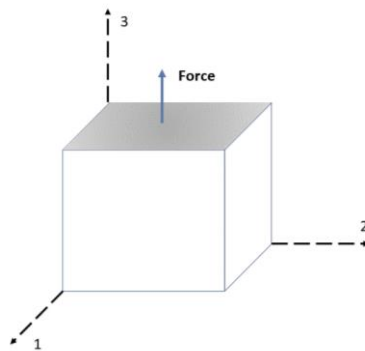
Figure 1-5. Principle plane and coordinate system of an anisotropic material's constitutive equation where a force is pulling on the 33-plane.

Moreover, due to this elongation along the 3-direction, i.e. Poisson's effect,

shrinkage will be observed along direction 1 and 2. The flux density of this strain will be

determined by d_{31} and d_{32}, that are identical for piezoceramics.

Usually, d_{15} is the largest of all coefficients for common piezoelectric materials. A

shear deformation would be governed by this coefficient, and it is often utilized for

making torque-based actuators (Glazounov, Zhang & Kim, 1998).

Due to these directional effects, d_{33} is sometimes called longitudinal extension

mode, d_{31} transverse extension mode, and d_{15} transverse shear mode. Moreover, d_{36} is

named longitude-shear mode.
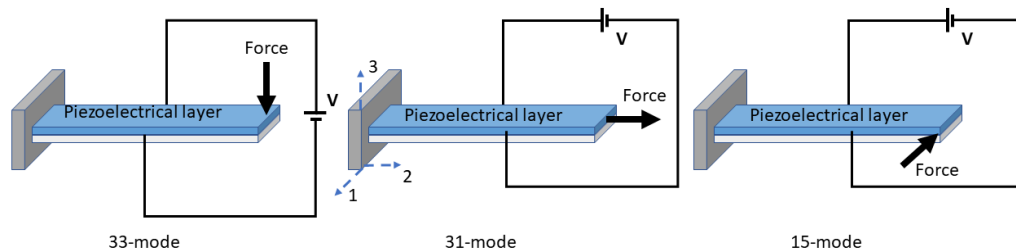
Figure 1-6. Illustration of different types of main mode energy harvesting devices.

As shown in Figure 1-6, different ways for utilizing the differential effects of

piezoelectric materials are shown schematically. Due to practical concerns, it is usually

unfeasible, or not useful, to make devices capable of utilizing multiple piezoelectric

coefficient modes as the need for numerous electrodes attached to different faces of the

material adversely complicate the production process.

Lastly, it is essential to highlight that the electromechanical coupling is not

entirely linear, as shown by Brockmann (2009) for PZT. There are several non-linear

effects that are influential. However, under standard laboratory conditions, the

assumption of linear behavior has been proven to be adequate Further studies of this non-

linearity, can be found in the work of (Chan & Hagood, 1994); (Ghandi & Hagood

1996); (Kermani Moallem & Pater 2008); (Kim & Kwak, 2004).

1.5.1 Simplification Due to Planes of Symmetries

For a meaningful comparison and further discussion of piezoelectric energy harvesting technology, a look at how symmetries affect the material properties of piezoelectric material is essential. Usually, only few properties for a piezoelectric material are available, and to fully apply these properties correctly in analysis, an overview of their interactions and simplification is outlined here.

For instance, the stiffness matrix for an orthotropic material has nine independent elastic constants.

$$
\begin{Bmatrix} \sigma_1 \\ \sigma_2 \\ \sigma_3 \\ \tau_{23} \\ \tau_{31} \\ \tau_{12} \end{Bmatrix} = \begin{bmatrix} C_{11} & C_{12} & C_{13} & 0 & 0 & 0 \\ C_{12} & C_{22} & C_{23} & 0 & 0 & 0 \\ C_{13} & C_{23} & C_{33} & 0 & 0 & 0 \\ 0 & 0 & 0 & C_{44} & 0 & 0 \\ 0 & 0 & 0 & 0 & C_{55} & 0 \\ 0 & 0 & 0 & 0 & 0 & C_{66} \end{bmatrix} \begin{Bmatrix} \varepsilon_1 \\ \varepsilon_2 \\ \varepsilon_3 \\ \gamma_{23} \\ \gamma_{31} \\ \gamma_{12} \end{Bmatrix}
\tag{1-6}
$$

For composites with unidirectional fibers with a plane of isotropy along the transverse direction, the numbers of constants reduces to 5.

$$
C_{22} = C_{11}, \qquad C_{23} = C_{13}, \qquad C_{55} = C_{44}
$$
$$
C_{66} = \frac{1}{2}(C_{11} - C_{12})
\tag{1-7}
$$

If every plane of material is isotropic, this reduced the stiffness to two independent constants,

$$
C_{33} = C_{22} = C_{11}, \qquad C_{23} = C_{13} = C_{12},
$$
$$
C_{44} = C_{55} = C_{66} = \frac{1}{2}(C_{11} - C_{12})
\tag{1-8}
$$

Likewise, for transversely isotropic piezoelectrical materials, the dielectric permittivity matrix can be written as, (Brockmann, 2009).

$$
\epsilon_{22} = \epsilon_{11}
\tag{1-9}
$$

And for isotropic materials

$$\epsilon_{33} = \epsilon_{22} = \epsilon_{11} \qquad (1\text{-}10)$$

1.5.2 Materials Exhibiting the Piezoelectric Effect

Before going into a more detailed discussion of other possible aspects of hybrid composites, a review of common piezoelectric materials would be beneficial. The overview emphasis is on the dielectric constants and stiffness. The permittivity of each material will not be discussed as this property is a minor contributor to the overall performance with respect to energy harvesting applications. For example, while the permittivity of piezoelectric materials changes within a single order of magnitude, the d_{33} parameter can change several orders of magnitudes, making it far more important contributor than permittivity.

In this chapter, only conventional piezoelectric materials are presented. Weak dielectric materials such as bone, silk, etc. will not be considered as they would be too weak for any practical energy harvester devices and are therefore not included in Table 1-1. SC denotes single crystals, FC is ferroelectric polycrystalline, and NW is nanowire. The table only presents some types of ferroelectric materials and are sorted by d_{33}, and do not include a full overview of all available materials for production or research. A more comprehensive overview is given by Wei et al. (2018) and for lead-based materials by Kang, Jung, Kang and Yoon (2016).

Here, dielectric constants have the unit pf pC/N, dielectric permittivity F/m and compliances, S is given in 1/Pa^{-12}. Compliance relates to stiffness through

$$[S] = [C]^{-1}$$
$$(1\text{-}11)$$

Table 1-1

Overview of Properties of Common Piezoelectric Materials

	z-Quartz[a]	ZNO[b]	ZNO[c]	PVDF	PbZr(0.52)Ti(.48)O3[d]	BaTiO3[e]	PMN–0.35PT[e]	PZT-5H[e]	PZT navy-II[f]	KNNTL:Mn[e]	PMN-0.07PT[e]
Type	NW	Sputter film	SC	film	FC	FC	FC	FC	FC		
S_{11}^E	12.77	10.13	6.4	E=8.3 GPa	E11=154 to 175 GPa	7.92	13.2	10.8	16.4	33.4	18
S_{12}^E	-1.79	-4.6	-1.93	G12=3.5 GPa	E22=142 to 168 GPa*	-3.8	-3.96	-3.28	-5.74	-7.36	-31.1
S_{13}^E	-1.22	-2.2	-2.53		E33=142 to 168 GPa*	-1.28	-6.05	-3.41	-7.22	-25.8	8.4
S_{22}^E	12.77	10.13	6.4			8.05	13.2	10.8	16.4	33.4	11.2
S_{33}^E	9.6	6.58	8.35			7.92	14.7	11.6	18.8	57.7	49.06
S_{44}^E	20.04	26.32	14			11.9	33.4	28.3	47.5	12.8	14.9
S_{55}^E	20.04	26.32	14			30.2	33.4	28.3	47.5	12.8	69.4
S_{66}^E	29.1	29.41	17			13.6			44.3	13.5	13
d_{31}	$d_{11}=-2.3$	-5.5		22	-38	-189	-133	-128	-171	-260	610
d_{32}	$d_{12}=-2.3$	-5.5		3		-24.5	-133	-128	-171	-260	-1883
d_{33}	$d_{25}=0.67$	10.29	14.3 to 26.7	-30	80±25,	225	270	315	374	545	1030
d_{15}	$d_{14}=-0.67$	-11.84				126	936	482	584	66	1188
d_{24}	$d_{26}=4.6$	-11.84				269	936	482	584	66	167
$\varepsilon_{11}^\sigma/\varepsilon_0$	4.52	446.13		12		265	4610	2640	1730	400	3564
$\varepsilon_{22}^\sigma/\varepsilon_0$	4.52	446.13		12		2680	4610	2640	1730	400	1127
$\varepsilon_{33}^\sigma/\varepsilon_0$	4.68			12		2130	3270	2490	1730	650	4033

Note. [1] Mechanical quality factor * Magnetron sputtering on Si-substrates and tested on these substrates.
** Material is not fully orthotropic - All values reported at room temperature
   a) (Piezo Data: Quartz, 2019) b) (Özgür, et al., 2005) c) (Zhao, Wang & Mao, 2004) d) (Liu et al., 2011) and (Marshall et al., 2011) e) (Topolov, Bisegna & Bowen, 2018) f) (Piezo Data: PZT-5H, 2019)

The following provides a brief overview of piezoelectric materials behavior, characteristics, and manufacturability considering their usability for energy harvesting devices starting with Quartz, famous for being the first material discovered to have piezoelectric behavior. Since then it has found a wide variety of practical applications; however, these applications are limited by a weak piezoelectric effect and non-optimal symmetry (i.e., does not experience any effect on the d_{33}-direction). Natural quartz has a stable crystal structure, low thermal expansion, high fusion temperature, and high

Young's Modulus, but suffers from the inclusion of impurities, bubbles, cracks, and twinning which significantly reduce its performances and repeatability (Oliveira Araujo, Rollo, Foschini, & Fortulan, 2017). Synthetic quartz, on the other hand, performs better, (Kholkin, Pertsev & Goltsev, 2008), but still, the electrical performances are in the lower range compared to the non-ferroelectric crystalline materials such as zinc oxide.

Zinc oxide is not new to the field, with studies dating back to 1935 (Özgür et al., 2005). It has found a wide variety of uses such as light-emitting diodes, acoustic wave devices, lasers, photodetectors, chemical/biosensors and surface acoustic wave (SAW) devices (Ozgur, Hofstetter & Morkoc, 2010) due to its high optical transmissivity, high conductivity and excitation binding energy (60 meV), large electromechanical coupling and since it is affordable and easy to produce. Other benefits include chemical safety and nontoxic nature.

The nanostructure morphologies of ZnO can be nanowires, nanobelts, nanotubes, nanoring's, springs, and nanohelices (Gao, Song & Jin Liu, 2006). ZnO can be grown via several routes whereas the chemical-vapor transport was the first, showing that ZnO has a strong tendency to grow with a strong (0001) preferential orientation on various substrates such as glass, sapphire, and diamonds (Özgür et al., 2005). Other techniques are magnetron sputtering, molecular-beam epitaxy (MBE), pulsed-laser deposition (PLD), metal-organic chemical vapor deposition (MOCVD) and hybrid vapor-phase epitaxy (HVPE).The various synthesis methods allow the ability to grow structures such as NWs on flexible surfaces (Gao, Song & Jin Liu, 2006); (Masghouni, Bourton, Philen & Al-Haik, 2015). ZnO NWs possess extremely high elasticity that can sustain high degrees of bending without cracks (Zhang et al., 2015). As shown in Table 1-2, ZnO

exhibits an excellent quality factor.

In Table 1-2, some piezoelectric materials are mentioned with their representative quality factor (Q-factor). Usually, a higher Q-factor indicates a lower rate of energy loss, and vibrations die out more slowly. This makes a higher Q-factor an attractive parameter in deciding on materials used for a device (Elahi, Pasha & Khan, 2014). It should be noted that the quality factor depends on temperature and resistance in the device. Furthermore, it is often frequency dependent.

Table 1-2

Mechanical Quality Factors

Material	ZnO[a]	BaTiO$_3$ [b]	PVDF[c]	PZT-5A[c]	Morgan Matroc PC4[d]	KNbO3[e]
Quality factor	430-1600	1300	10	75	600	900

Notes. a) (Mortada, Blondy, Orlianges, Chatras & Crunteanu, May, 2015) b) (BaTi03 Specifications, 2019) c) (Eovino, 2015) d) (Guillon, Thiebaud & Perreux, 2002) e) (Brockmann, 2009)

Poly(vinylidenefluoride) (PVDF) whose piezoelectricity was discovered by (Kawai, 1969), exists in two phases called α and β, where the β phase can only be piezoelectric after processing of the material by mechanical stretching and electrical poling. PVDF carries several benefits over other piezoelectric materials: it does not dipole at high loads (Butler & Sherman, 2006), outstanding mechanical flexibility, excellent chemical resistance, and is cheaper than most piezoelectric ceramics (Zhang et al., 2006).

PVDF can be produced in a variety of ways such as by synthesis from VDF monomer vinylidene fluoride, emulsion, suspension, solution-based (Xia & Zhang, 2018) that gives an end product in the form of a film. Thin films down to 20 μm have been reported in devices. For energy harvesting purposes, PVDF has some popularity not only

due to its flexibility and stability but also because it's out of resonance performance is as good as for PZT ceramics.

The piezoelectric materials discussed so far exhibit poor piezoelectric properties compared to the piezoceramics. In 1944 strong piezoelectric effect was discovered in barium titanate ceramics ($BaTiO_3$) (Uchino, 2010). $BaTiO_3$ has a remarkable higher coupling coefficient, but the downside is curie temperature not far off room temperature. This induces an aging effect leading to losing its strong effects over time (Uchino, 2010) and (Gao, Xue, Liu, Zhou, & Ren, 2017). It has been found useful in a wide variety of applications such as semiconductors, positive temperature coefficient resistors, ultrasonic transducers, and piezoelectric devices (Petrović, Bobić & Stojanović, 2008). $BaTiO_3$ synthesis technique depends on cost, quality of powders, and the starting material, as well as a successful ferroelectric transition. It is reasonably stable and easy to produce compared to its weaker predecessors (Uchino, 2010).

To overcome some of the shortcomings of $BaTiO_3$, various material combinations were tried out. From these trials, the PZT material was discovered (Uchino, 2010). PZT spans over a wide variety of ceramics, soft and hard with different compositions. Hard PZT often shows lower, but more stable properties after aging, whereas soft PZT shows higher properties but are sensitive to aging (Jin, 2011) and often fracture prematurely (Guillon, Thiebaud & Perreux, 2002). PZT500-series covers usually all different types of soft lead-tribunate (Advanced Electro Ceramics, 2019). Even though the name soft implies some degree of flexibility, they are considerably stiffer than flexible piezoelectric materials such as PVDF. The so-called PZT fibers, made via electrospinning, shows excellent electrical performance and high latitude where the mechanical flexibility can be

optimized by controlling the ratio of PZT to polymer for the fibers (Dagdeviren, et al., 2016).

Some types of PZTs can be grown hydrothermally, and into NWs as well, yet, the complex synthesis on growing them on certain substrates limits their practical application. Malakooti et al. (2016) proposed more viable methods that could be of interest for a hybrid composite device. The NWs were grown on a substrate titanium-thin film spin-coated with PZT sol-gel and then heat-treated at 175 to 225 °C in a steel container kept at these temperatures from several hours to days with a PZT solution. This substrate, with the PZT-NWs, was then incorporated into a carbon fiber harvesting device, as shown in Figure 1-7. A peak voltage of 0.35 V was reported. Uchino (2010) has published a comprehensive review of all the different types of PZT and their origin in his paper.
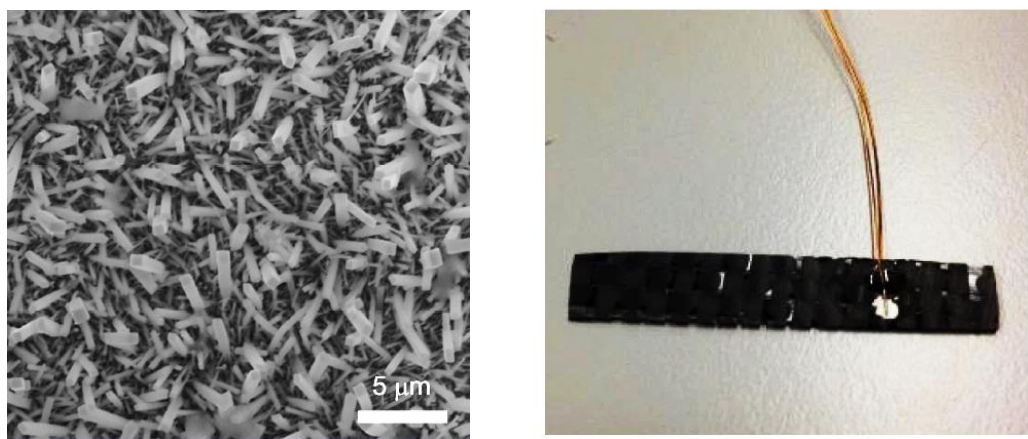
Figure 1-7. Vertically grown PZT NW and their later incorporation into a carbon fiber-based energy harvesting device, (Malakooti, Zhou & Sodano, 2016)

One important aspect to note here is the prohibition and restriction of lead usage in electronic. The European Union and Japan are working on regulations in this regard (Song, Zhao & Wang, 2017), which has led to a surge on studies in lead-free alternatives. Sodium-potassium niobate (KNN) has received a lot of attention due to its remarkable properties

and domain engineered structures (Brockmann, 2009). This material is shown to have a high mechanical quality factor with increasing vibration levels, whereas PZT degrades under such conditions. However, KNN is still challenging to produce, but the work of Saito et al. (2004) shows promising results comparable to the production of PZT patches.

Other investigations are refocusing on $BaTiO_3.Na0.5Bi0.5TiO_3$ (NBT) *S*odium Bismuth Titanate which has been reported to achieve the same level of output energy of BaTiO3, while having a significant higher curie temperature. Bismuth Ferrite (BFO) is another material under scrutineer and is both ferroelectric and ferromagnetic and shows great promises, but it is not fully understood how it works. Wang et al. (2003) have demonstrated promising thin films studies of BFO. For a compressive review of different lead-free piezoelectric materials, a review article by Aksel and Jones (2010) constitutes an excellent source.

Lastly, as seen in Table 1-1, PMN-PT based piezoelectric materials possess high piezoelectric constants; up to four times higher than bulk PZT. As shown by Xu et al., (2013) these can be grown hydrothermally and can be used in nanocomposite materials and could have a wide potential for hybrid composites in achieving higher power levels. They produced output currents that was six times higher than any other reported devices from their nanowires grown from PMN-PT sol-gel dispersed in distilled water and cured in an autoclave at 200 °C for 24 hours.

1.6 Hybrids of Non-Piezoelectric Materials and Piezoelectric Materials

The previous presentation outlined briefly some of the most crucial development and usage of piezoelectric materials up to date. It is out of the scope of this thesis to thoroughly research each negative and positive aspect of each material and their current development status. One example here is Barium Titanate where Gao, Xue, Liu, Zhou and Ren (2017) have discovered better performing materials with d_{33} even higher than 600 pC/N, more than most PZTs. Such work is continuously ongoing, and there are probably a variety of such developments that can potentially be included in the device developed in this research. However, such a review of current studies could be a review article on its own and have therefore barely been scratched during this work. The goal here has been to establish an overview for the further discussion of device designs and later potential.

When discussing the usage of piezoelectric materials, they usually took the shape of different types and size of patches glued to a plate or beam. This has, though, limited the full material's potential, and defined it usage to specific designs and operating conditions, besides, to give limited design flexibilities and a high likelihood of breaking the patch when fabricating the device. Fortunately, research into the creation of hybrid materials embedded with piezoelectricity has identified a variety of materials that can provide two or more functionalities such as loadbearing, sensing/actuating, structural health monitoring (SHM), power generation, damping, dynamic sensing, and vibration control.

The potential of these hybrid materials is only limited by the researchers' imagination. Some novel examples here are piezoceramics fibers that were implemented

into composite helicopter blades to reduce vibration due to aerodynamic forces (Bent,

Hagood & Rodgers, 1995) and structural batteries in the skin of a small aircraft that

maintain weight but increase endurance by 9.6 % (Thomas, Keennon, DuPasquier,

Qidwai, & Matic, 2003).

Hybrid and multifunctional materials do not imply only combinations of

piezoelectric materials, such as the example with skin batteries above. Another example

is self-healing composite materials were microencapsulated epoxy embedded into the

laminate acts as a healing agent if a region is damaged (White, et al., 2001).

According to the findings by Lin and A. Sodano (2008) the combinations of

piezoelectric materials and fibrous materials furnished both load bearing and device for

sensing and actuation. Additionally, weight is conserved when functionalities are

integrated into one material, and by using conductive fibers, the inner fiber can be used as

an internal electrode, drastically reducing electronic complicity and reduce impedance

compared to interdigitated electrodes (Sodano, Lloyd & Inman, 2006). A schematic of

novel multifunctional fiber is shown in Figure 1-8.
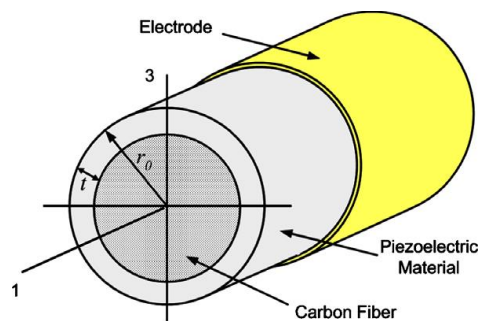
Figure 1-8. Schematic of a multifunctional fiber (Lin & A. Sodano, 2008)

Starting in 1993, PZT fibers were embedded into a fiber-reinforced plastic and

demonstrated the potential for creating multifunctional structures (Hagood & Bent,

1993). Illustration in Figure 1-9 gives an overall impression of how such hybrid fibers

were designed.
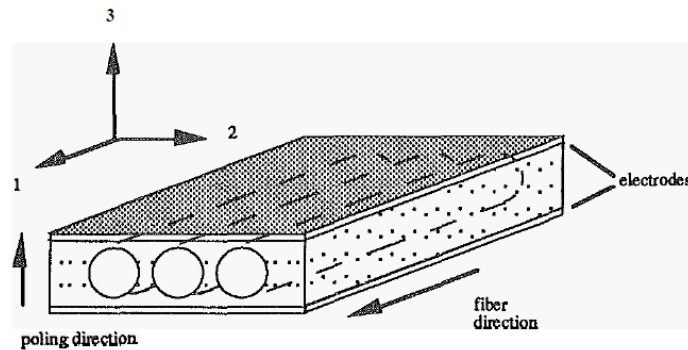
Figure 1-9. PZT fiber reinforced plastic composite (Hagood & Bent, 1993)

However, these early studies showed a significant reduction in the materials

strength due to the processes entailed in the piezoceramic fibers and their considerable

large diameter compared to the reinforcing material (Bowland, Zhou & Sodano, 2014).

Therefore, a raise to a different design was necessary, where the piezoelectric materials

instead would cover a stronger fiber in the middle. This has drastically minimized the

complexity, and the work done by Lin and Sodano (2009) on $BaTiO_3$ showed excellent

performance; however, the overall structural strength was unsatisfactory.

Alternatively, production methods based on hydrothermal growth of nanowires

onto a substrate has shown to not only retain the mechanical performances but also

improve them (Bowland, Zhou & Sodano, 2014) for $BaTiO_3$ NW and for ZnO NWs

(Masghouni, Bourton, Philen & Al-Haik, 2015).

Bowland, Zhou and Sodano (2014) utilized a hydrothermal growth technique for

$BaTiO_3$ that has previously been developed by Zhou, Tang and Sodano (2013). The

investigation stated that a 20-fold improvement in power density over an energy harvester

by ZnO NWs is achieved for nanowires alone. The hydrothermal process was lengthy and

required a solution temperature of up to 240 C° for up to three days where TiO_2

nanoparticles were seeded on the fiber surface. These will later react with Ba^{2+} that was added to the solution. The $BaTiO_3$-covered fibers retained 74 % of its original strength. It should be noted that exposure to water for raw carbon fibers effects negatively its loss tangent, storage modulus, and the on-axis and off-axis stiffnesses and strengths.

Even though the piezoelectrical effects for ZnO NWs seems to be weaker than PZT and $BaTiO_3$ counterparts, the addition of ZnO has a positive side effect in the form of increased tensile strength Masghouni (2014) and Ayyagari, Al-Haik, and Rollin (2018) showed that damping and fracture strength are increased by hydrothermally growing of ZnO on to carbon fibers. Lin, Ehlert and Sodano (2009) reported a 113 % increase in interfacial shear strength.

In both studies above, ZnO NWs were grown on carbon fibers at a relatively low temperature (less than 90 C°) after a process developed by Wang (2004) and repurposed for carbon fiber. The process involves sputtering of ZnO amorphous seeding layer, and later growth of ZnO NWs from these seeds via hydrothermal processing. Some results are shown below, where performance is reported in Table 1-3.

Zhang et al. (2015) showed how microfiber/nanowire hybrid structures yield dramatically higher flexibility and durability for wearable nanogenerators through their unique technique of covering separate Kevlar fibers with ZnO NWs.

Looking specifically at piezoelectric materials combined with fiber composites such as glass, Kevlar and carbon fibers, Qin, Wang and Wang (2008) showed the usage of ZnO nanowires on textile fibers for wind energy and body-movements loads, and as can be seen in Figure 1-10 (d) the flexibility of the material is impressive. A cellulose-based paper substrate has also been used together with ZnO (Gullapalli et al., 2010).
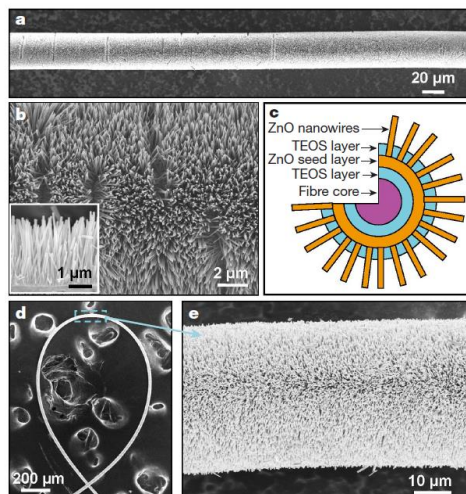
Figure 1-10. Kevlar fibers coated with ZnO nanowires, where d) shows the flexibility and e) the density of ZnO NW during bending (Qin, Wang & Wang, 2008).

The research discussed so far produce somewhat the same amount of harvested energy output, however, Liao et al. (2014) have proven that even higher performance is achievable. Their carbon fiber with gold coated ZnO NWs on top of paper wrapped around each fiber gave a voltage output of 17 mV, proving that their production can power a practical device. The seeding and growth were completely hydrothermal.

The work by Pan, Li, Guo, Zhu and Wang (2011) showed even better results and some of the benefits of using the carbon fiber itself as an electrode. However, their technique of growing ZnO NWs- film and etching it onto fibers is labor some and would be time-consuming for larger applications.

1.6.1 Combination of Piezoelectric Materials

The current status on hybrid composite materials with piezoelectric characteristics show that only low energy levels are achieved, especially when the composite structure is vibrated outside of its resonance frequencies. As seen in Table 1-3, the combination of the previously mentioned piezo material shows promising synergy effects.

Table 1-3

Overview of Different Piezoelectric Energy Harvester Performances.

Description	d33/d31	Power	Volt	Current	Comment
BaTiO3 CF	31.6 pm/V/-5.4 pm/V		16.4 mV		Root mean square voltage, at 0.5g (Bowland, Zhou & Sodano, 2014)
ZnO NW CF		0.16 nW/cm^2	3.4 mV	24.4 nA	Beam at resonance peak, no acceleration reported (Masghouni, Bourton, Philen & Al-Haik, 2015)
ZnO Kevlar			1.8 mV	4.8 pA	Nanogenerator for wearable (Zhang et al., 2015)
ZnO CF with ZnO paper		51nW/cm^2	18mV	35nA	200 ZnO NW coated fibers Contact force applied. (Liao et al., 2014)
ZnO NW film and CF			3 V	200 nA	ZnO NW film wrapped around CF. CF used as one electrode. (Pan, Li, Guo, Zhu & Wang, 2011)
ZnO NW and PZT				270 nA	A device with ZnO NW grown on an ITO-glass substrate (No Jeong et al. 2013)
ZnO NW and BaTiO3				105 nA	Push-device. 7 times larger current than only ZnO and 3 times more than pure BaTiO3 was reported (Chang et al., 2016)
ZnO NW and PVDF		0.2 V	10 nA	2uW/cm^2	Plane shaped generator made under a low frequency mechanical motion (Lee et al., 2012)

To the author's knowledge, no cited investigation has tried synergizing these effects for hybrid fibers composites (HFC).

A wide variety of combinations of piezoelectric materials have been proposed. BaTiO$_3$-reinforced PVDF composite was shown by Kakimoto, Fukata and Ogawab (2013) to increase the harvested power by 26 % compared to pristine PVDF. However, hot rolling and thermal pressing make this technique unsuitable for HFC.

By using PZT with PVDF, Tiwari and Srivastav (2015) showed an improved d$_{33}$ from -32 pC/N to 84 pC/N for a thin film. The films were produced via a casting technique; from ceramic powder that was hot-pressed, stretched and kept at temperatures up to 1280 °C for a longer duration.

PZT particle reinforced polymer, promote PVDF by the inclusion of fillers such

as carbon nanotubes, graphene, metal oxides, ceramics fillers with KNN and PVDF-graphene. Mishra, Krishna, Singh and Das (2017) presented a recent review.

No et-al. (2013) showed how hydrothermally grown ZnO NWs could be combined with PZT by a sputtering technique. From their work, it was shown that the average current improves significant (270nA) compared to both ZnO NW alone (0.5nA), and PZT thin films alone (9nA).

Similar work, but with $BaTiO_3$, was carried out by Chang et al. (2016). They reported an improved average current by seven times compared to pure ZnO, see Figure 1-11.

Here, hydrothermally grown ZnO NWs were infused with $BaTiO_3$ by a magnetron sputtering technique. This was built into a push device based on an n-type silicon substrate. One interesting note here is that the thin $BaTiO_3$ layer (50 nm), and the authors note that the space between the ZnO NWs must not be fully occupied by $BaTiO_3$ which will leave little room for the ZnO strain confinement effect. Both papers showed the need for annealing of the piezoceramics (900 C° for $BaTiO_3$ and 600 C° for PZT), nonetheless, for $BaTiO_3$ and ZnO NW, no polarization was conducted.
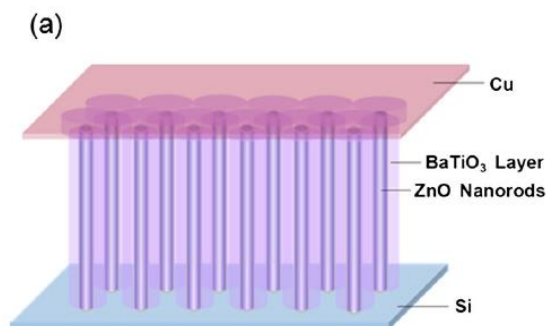
Figure 1-11. Illustration of a device with ZnO NWs covered by sputtered $BaTiO_3$ (Chang et al., 2016).

Another research worth mentioning here is that of Lee et al. (2012) on ZnO NWs/ PVDF hybrid for wearable clothing purposes. Flexible fibers were used together with a thermal evaporation seeding technique for ZnO grown on a thin layer of gold acting as an underlying electrode. PVDF was added by a dipping method. The ZnO was seen to be working as a great droplet collector, and therefore, hydrophilic to the PVDF solution. This device was deemed practical by a wearable clothing powered by movements of the elbow.

2. STATIC AND DYNAMICAL MATERIAL TESTING

2.1 Introduction

From the literature review, it is evident that certain types of multifunctional materials (hybrids) have benefits not only of being able to encompass several smart functionalities such as sensing and actuating but can also enhance the mechanical properties of the host material.

The benefits of ZnO NWs grown on fibers become especially evident and this material is therefore a natural choice for further studies. Reports indicate up to a 43 % increase in the damping coefficient when conducting impulse tests on ZnO-CF composite beams (Masghouni & Al-Haik, 2013), with a 5% decrease in natural frequency. Despite that, 113 % of interfacial shear strength, 37.8 % increase of lamina shear strength and 38.8 % increase of the lamina shear modulus (Lin, Ehlert & Sodano, 2009) were reported by single fiber/epoxy tests, which more than surpass some of the adverse side effects. Other research (Ehlert, Galan & Sodano, 2013) reported that the peak pull-out load increases by 390 % for single fibers when comparing Kevlar composite sheathed with ZnO NWs to bare Kevlar fibers. Impact resistance improvement of 66 % was reported too.

These citations highlight some of the mechanical benefits of adding ZnO NWs to a composite material. However, ZnO has a relative weak piezoelectric effect compared to other materials such as PZT and $BaTiO_3$. This chapter will investigate some of the mechanical consequences when ZnO NWs are combined with another piezoelectric material to improve a composite structure piezoelectrical performance.

PZT was combined with ZnO NW on a silicon testbed due to its elevated

piezoelectric properties (Fujisawa, Iwamoto, Nakashima & Shimizu, November, 2012). However, up to the author's knowledge, there are no published studies on combining such materials with CFRPs so far. Only one investigation pointed out some degree of mechanical strength loss of encompassing PZT thin layers onto composite fibers (Bowland, Zhou & Sodano, 2014). The possibility that this trend is also applicable to the methods discussed here will be addressed.

2.2 Discussion on Materials and Production Methods

The choice of materials and methods conforms to previous research done on ZnO NW and carbon fiber (Ayyagari, Al-Haik & Rollin, 2018) and utilizes plain-woven carbon fabric from Hexcel Inc. (Stamford, CT, USA) designated as 6000k HexTow™ IM7. This plain-woven carbon fabric is unseized in order to enhance binding of nanomaterials to the carbon surface as sizing acts a buffer between the fiber and the matrix.

Kao, Chen, Young, Lin and Kung (2012) reported that the short circuit current density, open-circuit voltage, and energy conversion efficiency increase with the length of ZnO nanowires. Therefore, to increase the efficiency of an energy harvester, an optimal process of seeding and ZnO NWs growth should focus on obtaining longer NWs.

Seeding is the process of adding a material with a weak dipole so that it will attract other materials with a weak dipole in a solution bath later. Several seeding techniques are commonly reported for ZnO NWs such as sputtering, dipping, microwave seed coating, and electromechanical deposition method. A mosaic of results from four standard practices for seeding and growth of ZnO on single carbon fiber is shown in *Figure 2-1*.
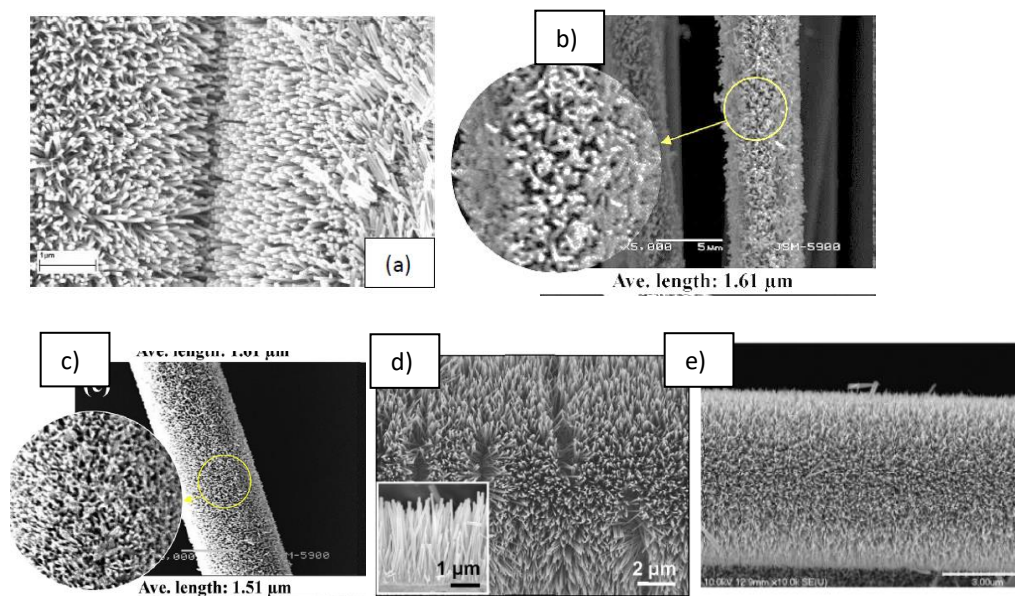
Figure 2-1. Results of different seeding and growth methods for ZnO NW; a) RF-magnetron sputtering and hydrothermal growth, (Masghouni, 2014), b) Hydrothermal seed coating and growth (A.Song, Kwang Lee, Bang & Kim, 2016) c) Microwave seed coating and growth by microwave, (A.Song, Kwang Lee, Bang & Kim, 2016) d) Hydrothermal seed coating and growth (Qin, Wang & Wang, 2008) and e) Dip coating at 150 °C for 10 min and then hydrothermal growth (Lin, Ehlert & Sodano, 2009).

One important observation of these investigations is that the ZnO NWs must fully enclose the fibers to avoid any short-circuiting, and therefore, a dense growth is needed. There are no published recommendations on which method presents the best mechanical and dynamical properties, but it is reasonable to assume that a higher number of ZnO NWs is associated with a better piezoelectric response. It is furthermore reasonable to assume that a very dense ZnO NWs layer could limit the epoxy infusion and restrict ZnO NWs movement, which would worsen both the mechanical and piezoelectric properties. Taking these assumptions into consideration, the techniques shown in Figure 2-1 a), d) and e) seem most promising for growing long and dense layers of ZnO NWs.

In this thesis, the RF magnetron sputtering technique was preferred due to the prolonged aqueous exposure used in hydrothermal seeding technique. It was reported that

exposure for an extended time to aqueous solutions drastically worsened the fibers'

mechanical and dynamical properties (Ayyagari, Al-Haik & Rollin, 2018); (Masghouni,

2014).

However, for growing ZnO NWs on carbon fibers the choice of methods is

limited. Usually, a hydrothermal growth with different molar solutions of HMTA

(Hexamethylenetramine–hexamine; $(CH_2)_6N_4$) and zinc acetate hexahydrate

$(Zn(O_2CCH_3)_2(H_2O)_2)$ is performed. Physical vapor deposition was also reported, but

with lower aspect ratios (length to width) making them impractical for energy harvesting

functions.

Xu et al. (2009) has published a comprehensive study of the growth parameters of

ZnO NWs, such as how to optimize the reaction temperature, time, precursor

concentration, and capping agent. They showed that having a solution concentration of 1

mmol/L at a temperature of 80 °C, for about 30 hours gives ZnO NWs with the highest

aspect ratio.

They also concluded that HMTA acts as a weak base, slowly hydrolyzing the

water and gradually releasing hydroxide ions which improves the growth of NWs. If OH^-

is released too quickly, Zn^{2+} will disappear quickly from the solution, leaving less Zn^{2+}

available for growth. Furthermore, the ammonia in water will dissociate into ammonium

(NH_4^+) and hydroxide (OH^-). The process can be described by the five major chemical

reactions listed below.

$$(CH_2)_6N_4 + 6H_2O \leftrightarrow 4NH_3 + 6HCHO$$

$$NH_3 + H_2O \leftrightarrow NH_3 \cdot H_2O$$

$$NH_3 \cdot H_2O \leftrightarrow NH_4^+ + OH^-$$

$$Zn^{2+} + 2OH^- \leftrightarrow Zn(OH)_2$$

$$Zn(OH)_2 \xrightarrow{\Delta} ZnO + H_2O$$
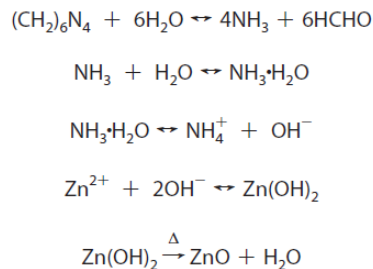
Figure 2-2. Five major chemical reactions for hydrothermal growth.

2.2.1 Speeding Up Growth Time and NWs Length

An essential aspect of this research was to see if a faster growth method is achievable. Xu et al. (2009) used growing times of 6 to 48 hours. Relevant papers on ZnO NWs gown on carbon fiber report growing times between 4 to 8 hours using convection ovens. These prolonged soaking times of carbon fibers are damaging to the fibers, as previously discussed.

However, some research indicates great promise for using microwave technology for rapidly growing ZnO NWs with results matching and even surpassing NWs length commonly reported for convection ovens. Masghouni and Al-Haik (2013) reported 1.62 μm long NW after 4 hours in the oven, Song, Lee, Bang and Kim (2016) achieved 1.68 μm NW on carbon fiber for just 10 min with a 2.45 GHz microwaves under a maximum output of 700W. This is a 95 % reduction in production time compared to Masghouni' s work.

Liu, Hong, Ge, Liu and Xu (2014) showed that even longer NWs can be achieved by continuously replenishing the growth solution with a fresh solution. They reported lengths from 3.4 μm to 17.2 μm with growth times from 1 to 5 hours on a fluorine-doped tin oxide (FTO) glass in a 2.45 GHz microwave ran at 640 W. Teflon tubes were used to supply and extract solution from the microwave oven. Even though the ZnO NWs was

grown on an ideal substrate, this demonstrates some of the possibilities made available by

continuously adding a fresh solution.

Unalan et al. (2008) reported identical trends using a commercial microwave.

They also found that the growth can be initialized at power levels as low as 120W. The

reduction in time was attributed to the rapid heating of the reaction precursor up to

crystallization temperature and their shorter crystallization times were associated with the

rapid dissolution of precipitated hydroxides by the microwave heating. Figure 2-3

illustrates the similarities between the use of a furnace oven and microwave oven for the

final growth, where the microwave oven took a fraction of the time compared to furnace

oven growth.
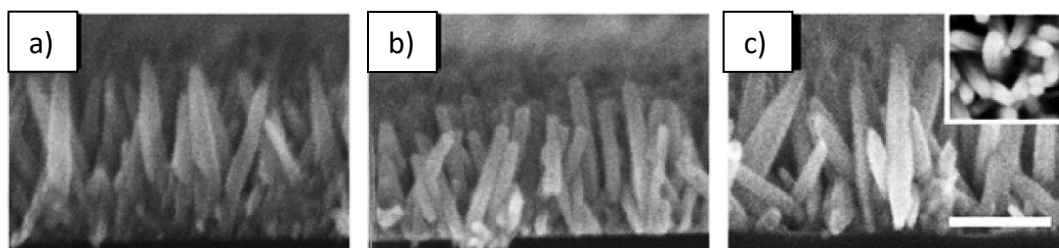
Figure 2-3. Showcasing the difference in ZnO NWs growth from a) furnace for 90 min, b) microwave at 120W for 30 min and c) microwave at 700 W for 6 min (Unalan et al., 2008).

With these observations in mind, it would be preferable if identical or even better

growth can be achieved. The three research groups reported here used expensive

microwave ovens designed for industrial use. It would, therefore, be interesting to see if

the same trend would be feasible utilizing household microwave ovens.

For the current experiment, a woven carbon fiber cloth from Hexcel Inc.

(Stamford, CT, USA) designated 6000k HexTow™ IM7 was initially sputtered with 75

nm ZnO layer using an RF-magnetron sputtering system (ATC Orion Sputtering, Systems

from AJA International, Inc.) at 75 W to 140W under 3mTorr vacuum. Some of the

cloths were sputtered on both sides; others on one side only. Presented below is an

overview of the growth results investigated with a FEI Quanta 650 scanning electron

microscope (SEM, now Thermo-Fisher Scientific, Hillsboro, OR, USA). Different

molarities of zinc acetate dihydrate $C_4H_{10}O_6Zn$ and HMTA $(CH_2)_6N_4$, (Alfa Aesar,

Tewksbury, MA, USA) at 98 to 99+ % purity was used to study the effect on length and

density. All experiments were conducted in the convection oven at 90 ºC.
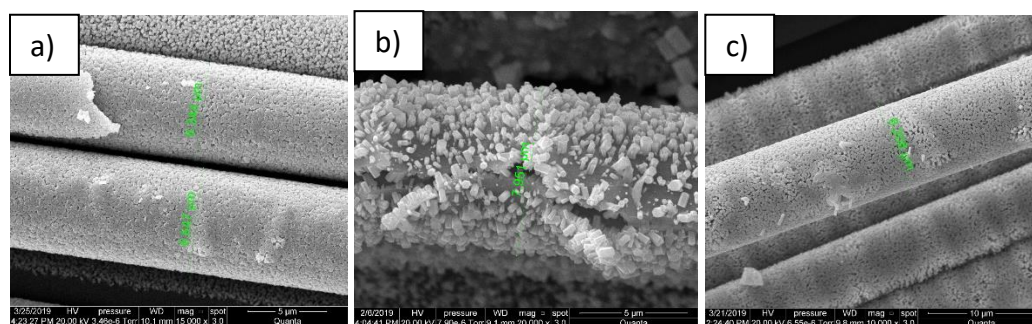
Figure 2-4. Conventional oven growth of ZnO NWs for 8 hrs. using a) 1800 ml 40 mmol solution with three layers of woven CF, b) 1200 ml 80 mmol solution , and c) 1200 ml 40 mmol solution.
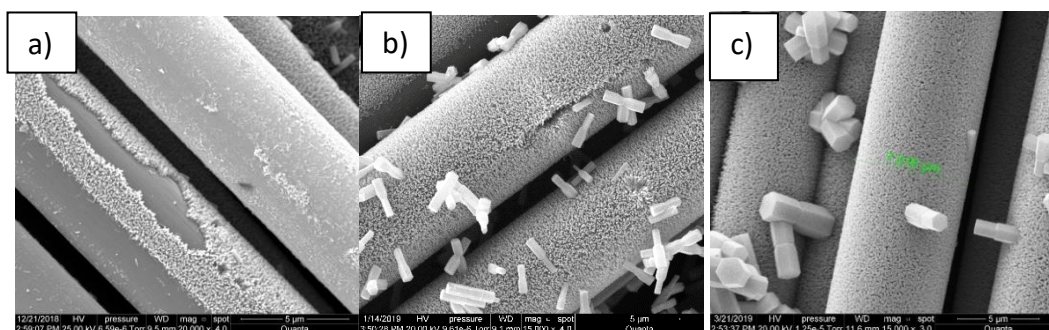
Figure 2-5. Microwave growth of ZnO NWs using a) 1350W microwave 30 min at 50 % power with 40 mmol – cleaned by sonication, b) 1350W microwave with heat up on 100 % power for 5 min, followed by 30 min on 20 % effect. This was repeated with a fresh 40 mmol solution, and c) 40 min at 70 % power with 80 mmol solutions. Solution amount for each setup was 900 ml.
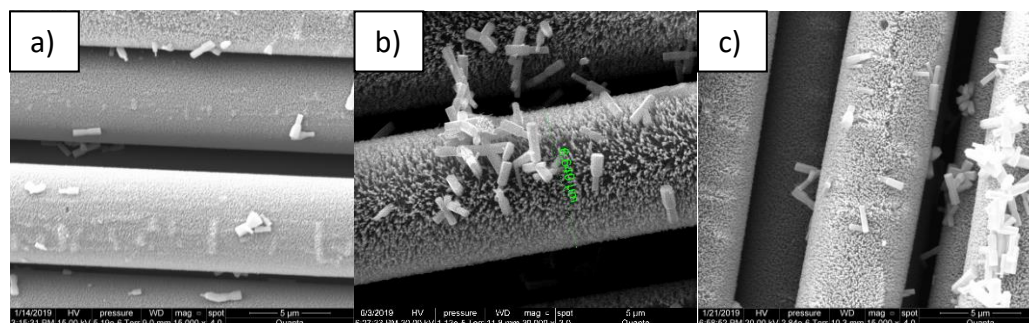
Figure 2-6. Microwave growth of ZnO NWS. All experiments utilized 40 mmol solutions for a) 20 min at 20 % of a 1000W microwave, b) 1250 W microwave changed solution 4x times at 10 % for 25 min with 5 min 100 % heat up. Sputtered on both sides ND c) 1350W microwave on 20 % for 30 min with 5 min heat up, repeated twice.
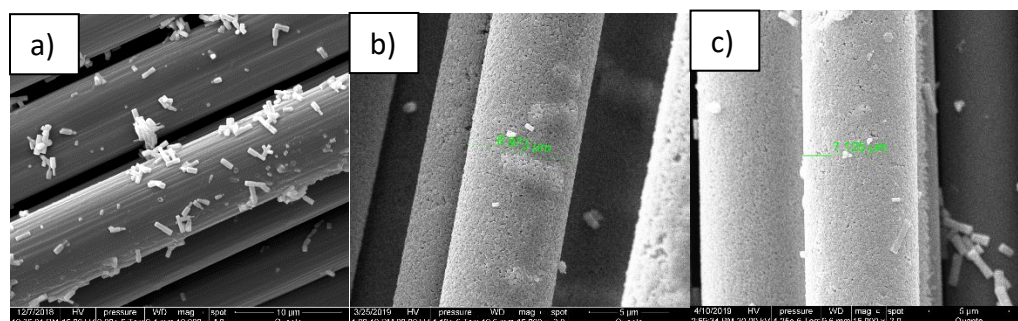
Figure 2-7. ZnO NWS growth for a) 8 hours in the conventional oven where the substrate was a sized CF cloth b) Conventional oven for 8 hours with 80 mmol solution and two CF clothes c) Heated in microwave oven at 100 % and then placed in a conventional oven at for 4 hours. Process repeated twice with 80 mmol 900 ml solution.

Figure 2-4 illustrates some of the initial trials in the conventional oven, where the process was intended to speed up by combining multiple CF-cloths in a single solution. This seemed, however, to deplete the solution too soon. Figure 2-4 (b) Indicates that initial ZnO layer was too thick, leading to non-uniform growth, whereas in Figure 2-4 (c) a good growth result was obtained.

Figure 2-5 and Figure 2-6 show the attempt with the microwave oven, where trials with the solution being rapidly heated up to a boiling point, and then kept at a 10 to 20 % effect for a longer duration appeared to be favorable. Replenishing with a new solution and repeating the process appeared to strengthen the growth.

Figure 2-7 shows some different results, where Figure 2-7 a) demonstrates why a de-sized ply is necessary for effectively binding the seeding layer and initializing a desirable radial directed growth pattern since the sized carbon fiber did not allow seeding particles to adhere to the fiber which resulted in poor growth of the ZnO NWs.

2.3 Experimental Production Method

After carefully studying the results of changing the growth parameters conducted in section 2.2.1, the benefits of using a typical in-house microwave oven become apparent with long and consistent NWs and rapid growth rate. Additional advantages are less exposure time to the solution for the fibers reduces the strength degradation and allows a more rapid process that saves time and increases the production rate. Based on these findings, the growth will be carried out via the microwave process where the cloth was exposed to 5 min rapid heat up at 100 % effect and then 25 min at 10 % was chosen. The process was repeated twice to ensure the excellent NW lengths.

For mechanical testing purposes, it is interesting to compare the specimens based on carbon fibers with ZnO NWs prepared in the microwave to specimens based on bare carbon fibers. In addition to this, no published research, up to the author's knowledge, has probed how the sputtering of a PZT thin film alters the mechanical performances of carbon fiber laminates.

Five configurations of composites specimens were investigated: plain, ZnO NW, heat-treated, only PZT and lastly with ZnO NW and PZT together. Each specimen utilized a 6000k HexTow™ IM7 woven cloth, which is a unique surface-treated and sized cloth. For the sample with ZnO NWs, the woven carbon fabric was seed-sputtered at 75 W under a vacuum of 3 torr by a ZnO target until an initial thickness of 75 nm was

reached. Each cloth with deposited seeding was immersed in equimolar growth solution of 40 mmol zinc acetate dihydrate $C_4H_{10}O_6Zn$ and HMTA $(CH_2)_6N_4$ at 98 to 99+ % purity (Alfa Aesar®, Tewksbury, MA, US,). The growth solution components were prepared individually by mechanical sonication via a Vibra-Cell VCX 500 (Newtons, CT, USA) tip ultrasonic processor for 20 min before mixing and sonicating for additional 20 min. The solution was heated in a 1.6 cu. ft household microwave oven (1250 W, NN-SN7555 Panasonic, Newark, NJ, USA) at 100 % power for 5 min for rapidly achieving the growth temperature and for 25 min at 10 % power to maintain the growth temperature. The process was repeated twice. After the growth, the CF-cloths were dried in a convection oven at 90 C° for at least 24 hours to remove any moisture effectively.

The carbon fabric specimens with PZT had a 200 nm thick layer $(PbZr(.52)Ti(.48)O3)$ deposited from a 3.00" diameter × 0.250" thick target (Kurt J. Lesker, Jefferson Hills, PA, USA) sputtered under 75W and 5mTorr. A lower vacuum than 5mTorr could not be achieved while maintaining the plasma, and a ramp up and down the rate of 0.1 W/min was found necessary for successfully initializing plasma.

All specimens, including those with PZT films and a non-treated set, were annealed using a 3-inch tube quartz tube furnace (OTF-1200x from MTI Corporation, Richmond, CA, USA). Heat treatment is essential to consolidate the PZT, as the sputtering results in an amorphous phase PZT thin film that needs to be sintered (No et al., 2013). The annealing was conducted after the work of Frunza et al. (2011). They found that a thermal treatment at 650 C° for 1 hour with a 5 C°/min heating rate was ideal for sintering.

It is worth mentioning that, these investigations deal with ideal thermally resistant

substrates (e.g. silicon wafer) rather than carbon fiber substrates. As was shown by Feih and Mouritz (2012), the carbon fibers modulus degrades significantly with elevated temperatures when exposed to air, but not as much in an inert atmosphere. However, tensile strength was reported to drop by almost 50 % both for air rich and inert gas atmospheres. All other material attached to the specimens, such as fiber tapes, was removed before treatment to avoid external impurities.

All these considerations, therefore, consolidated the post-treatment of the sputtered PZT films into five steps. (1) Clearing out any other gases in the tube furnace for 2 min with inert gas of N_2 at a flow rate of 3000 standard cubic centimeters per minute (sccm). (2) Vacuum pumping for 2 min of to ensure an inert environment. (3) Setting N_2 flow rate to 2000 sccm while heating the furnace by a rate of $5C°/min$ until 650 C°. (4) Keeping a constant temperature of 650 C° for 1 hour under 2000sccm N_2 flow rate.(5) Allowing the furnace cool down naturally while maintaining a N_2 flow rate of 2000 sccm.

In Figure 2-8, the difference between a sputtered and annealed specimen can be observed as well as the samples being prepared in the furnace tube.

Figure 2-8. a) Left: ZnO NW sputtered with 200 nm PZT before (left) and after (right) heat treatment b) The specimens before heat treatment in the furnace tube.

After sintering, the PZT thin film changed color from brown/yellow into white.

Furthermore, it can be observed that combining more than one specimen with ZnO thin

films at once into the furnace resulted in samples being covered with a layer of soot. See

Figure 2-9. This was surprising, as the atmosphere was inert, and both the tube and the

carbon fiber specimen were visually free of external impurities.

Figure 2-9. Sooted specimen after heat treatment of multiple samples together.

Access to X-ray diffraction (XRD) was not available at the time this thesis was concluded, and the source of the sooting was therefore unclear. Nonetheless, as seen in Figure 2-10, there are apparent dissimilarities between a) ZnO NWs, b) ZnO NWs with PZT thin film and c) sooted ZnO NWs with PZT thin film indicating some accidental material changes are occurring.
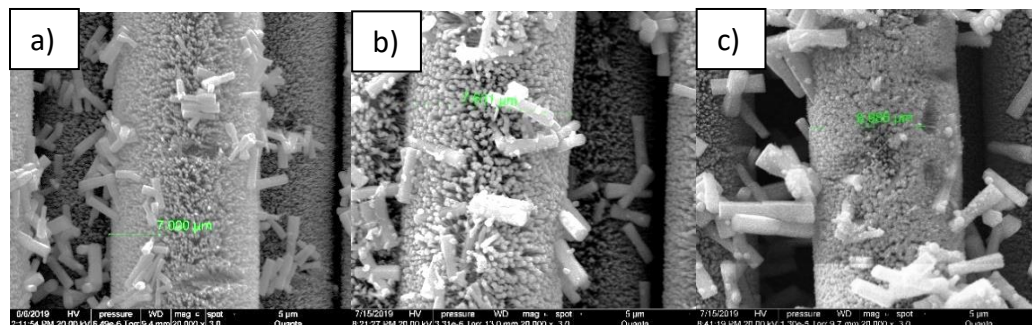
Figure 2-10. SEM micrographs of carbon fibers with a) Pure ZnO NW, b) ZnO NWs coated with 200 nm PZT film after heat treatment, and c) Sooted ZnO NW coated with 200 nm PZT film after heat treatment.

Preparation of the composites based on the five different fibers configurations followed the ASTM D5687. Each setup consisted of two layers of the material in interest, with any piezoelectrical content only present at the interfacing sides. Preparation of the laminates was done via a vacuum-assisted composite press hand-layup process. The matrix comprised Aeropoxy™ (PTM&W Industries, Inc., Santa Fe Springs, CA, USA) PR2032 epoxy resin and PH3665 hardener in a 100:27 weight mixture as recommended by the supplier. When mixed, the viscosity was reported to be 925-975 cps and the glass transition temperature, Tg, 91 °C.

The composites were first cured for 1 hour under a high vacuum (0.8 Torr), followed by a 2-hour post vacuum curing in a composite press heated to 90 ℃ and pressure of 2 tons (Wabash MPI, Wabash, IN, USA). Fiber weight fractions after curing were reported at 77.3 % for non-treated laminates, 86.12 % for heat-treated laminates,

81.8 % for ZnO NWs, 79.7% for PZT alone and 86.7 % for the ZnO NWs and PZT configuration. These weight fractions are relatively high compared to standard composites, but when considering how amenable the IM7 cloth is and how little room there is left for epoxy between fibers when pressing only two layers together, the high percentage makes sense.

Prior to the tensile tests, the laminates were prepared and cut into strips following the ASTM standard D3039/D3039M-08 with abraded G-10 tabs bonded to the ends using the same resin as for laminating. The strips had a size of 0.5"x5.0". The tensile tests were conducted using an MTS Criterion™ Model 43 machine (MTS, Eden Prairie, MN, USA) with an extensometer, MTS 634.12E-24, having a 1 in gauge length to record strain at a rate of 0.01 mm/min. The strain was measured using an MTS extensometer.

A separate batch of specimens was prepared similarly for Dynamical Mechanical Analysis (DMA). DMA elucidates the elastic and viscoelastic behaviors of a given material by applying a sinusoidal force. Properties of interest here are tan (δ), storage modulus, loss modulus, and the change in glass temperature (Tg). Tan (δ), also called loss factor, denotes the damping capabilities of the material by measuring the loss of energy from an inflicted force into the material, defined by the ratio of the loss (E'') to storage (E') moduli. Storage modulus measures the sample's elastic nature, while loss modulus gives information about how energy is dissipated internally in the sample.

For this experiment, a PerkinElmer DMA 8000 (Walkham, MA, USA) was utilized in a 3-point bending fixture. Following a setup developed by Goertzen and Kessler (2007), specimens of approx. (45 x 10 x 0.5 mm) were prepared, and two different sweep modes were run based on either temperature or frequency. For the

temperature mode, a frequency of 1 Hz was set while the temperature was ramped from

30 to 140 °C at a 2 °C/min rate. The frequency sweep was run from 1 to 40 Hz at 30°C.

Both tests were reported with a force and strain of 2N and 0.03 mm, respectively.

2.4 Results and Discussion

2.4.1 Tensile Testing Results

The stress vs. strain curves were obtained for each representative composite

configuration and used to create the chart seen in Figure 2-11. This figure indicates the

on-axis tensile strengths and Young's moduli acquired at up 0.30 % of the strain value.

Glass fiber was also tested for incorporating the correct material properties to the FE-

analysis shown in section 4.
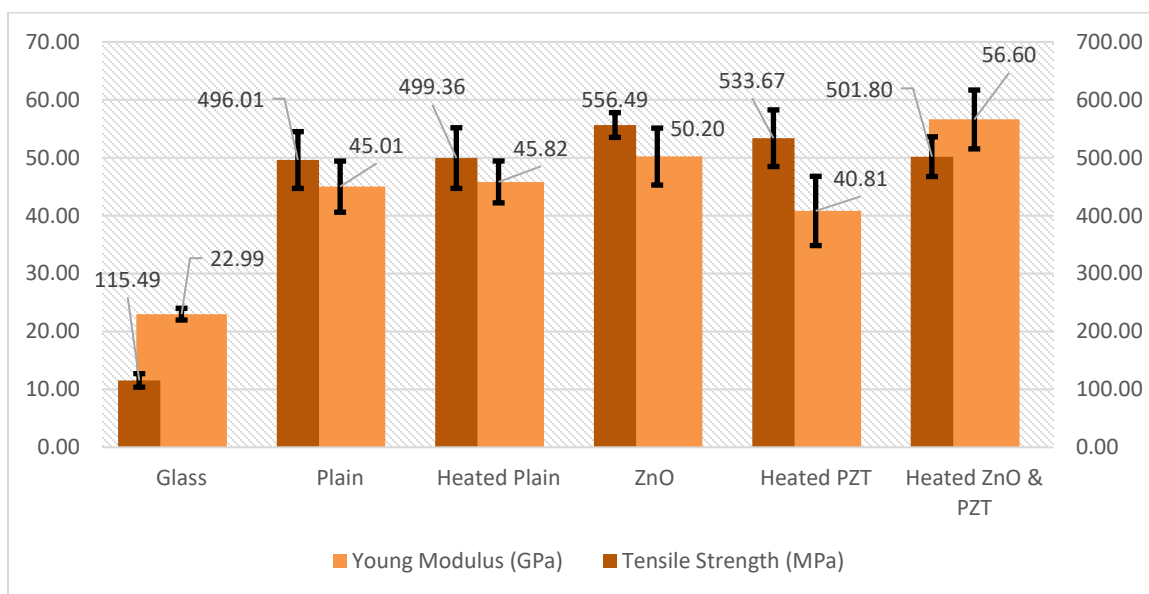
Figure 2-11. Tensile strengths and apparent Young's moduli for composites based on
different surface treatment of IM7 HexTow and a glass fiber sample. The error bars
indicate standard deviation (SD).

An increase of apparent Young's modulus by 1.8 % for heated and by 11.54 % for

surface treated with ZnO NWs growth was observed compared to non-treated laminates

(plain). An increase by 0.67 % and 12.2% in tensile strength was observed for these

samples. These data agree well with other published research; a 20.5 % increase in strength (Masghouni, 2014).

Nevertheless, the 1.8 % improvement in stiffness for samples being heat treated in the furnace was surprising and is likely due to carbonization occurring at elevated temperatures in inert environments when carbon fiber structures are converted into the graphite crystal structure which improves the modulus of the fiber. In their research, Wang, Zheng and Zheng (2011) have shown that such carbonization occurs at the temperature levels used here.

A noticeable decrease in Young's modulus, by 9.32 % compared to plain cloth, was observed for laminates sputtered with only a 200 nm layer of PZT and heat treated. PZT alone, as indicated by Bowland, Zhou and Sodano (2014) can worsen the mechanical strength characteristics of the hybrid composites. The non-ductile nature of PZT was, however, shown to improve the tensile strength of the laminates by 7.6 % compared to non-treated plies likely due to its stiffening of the laminate fibers.

The samples with combination of ZnO NWs and PZT thin films show an improvement of Young's modulus by 25.8 % and tensile strength improvement of 1.2 % compared to plain fibers. Compared with ZnO NWs a significant improvement of the Young's modulus by 12.8 % whereas the tensile strength decreased by 9.82 % for the combined material.

For the ZnO NWs/PZT sample, the gain in Young's modulus is significant, while the unchanged tensile strength compared to plain CF sample indicates that the laminate will not be degraded by the addition of PZT when ZnO NW are present. Even though the increases can be attributed somewhat to the addition of ZnO NW, the stiffness gains

surpass both reductions in strength and modulus due to heat treatment and shows no degradation due to the addition of PZT, but rather a strengthening. It is possible that the naturally stiff PZT material acts as a support structure for the ZnO NW grown radially around the carbon fibers and prevents the NW from bending, resulting in a more rigid material.

2.4.2 DMA Results

Four different subsets of data were extracted from the DMA, where two data sets emphasize storage modulus and two other data sets focus on damping, are presented as tan delta (δ).
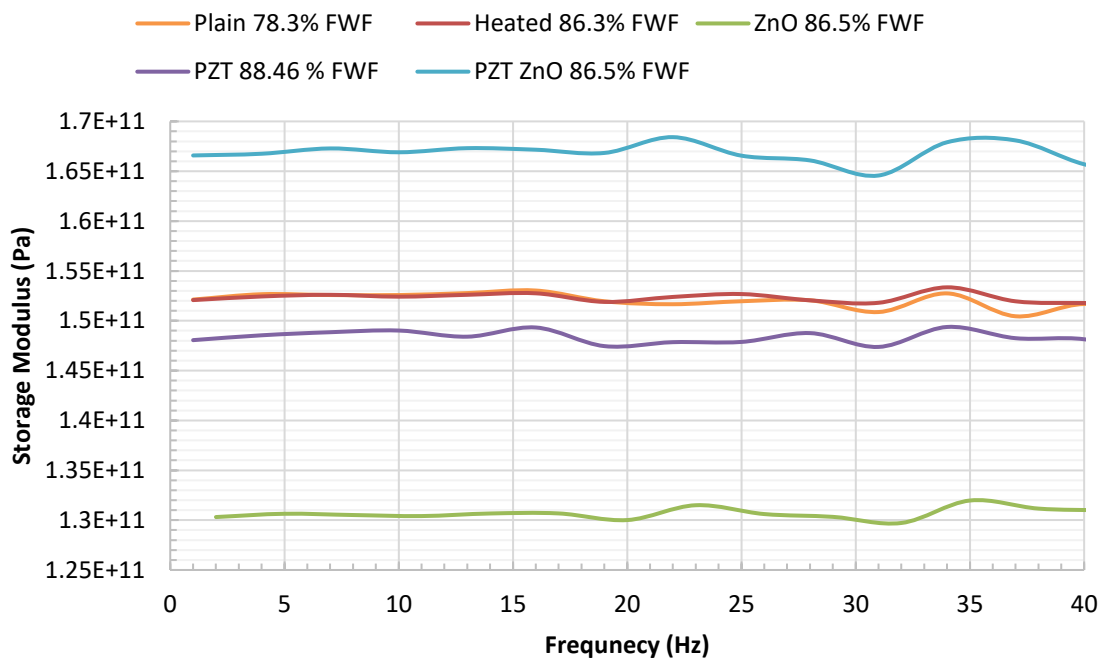
Figure 2-12. Storage modulus of the different FRPs measured from 1 to 40 Hz.
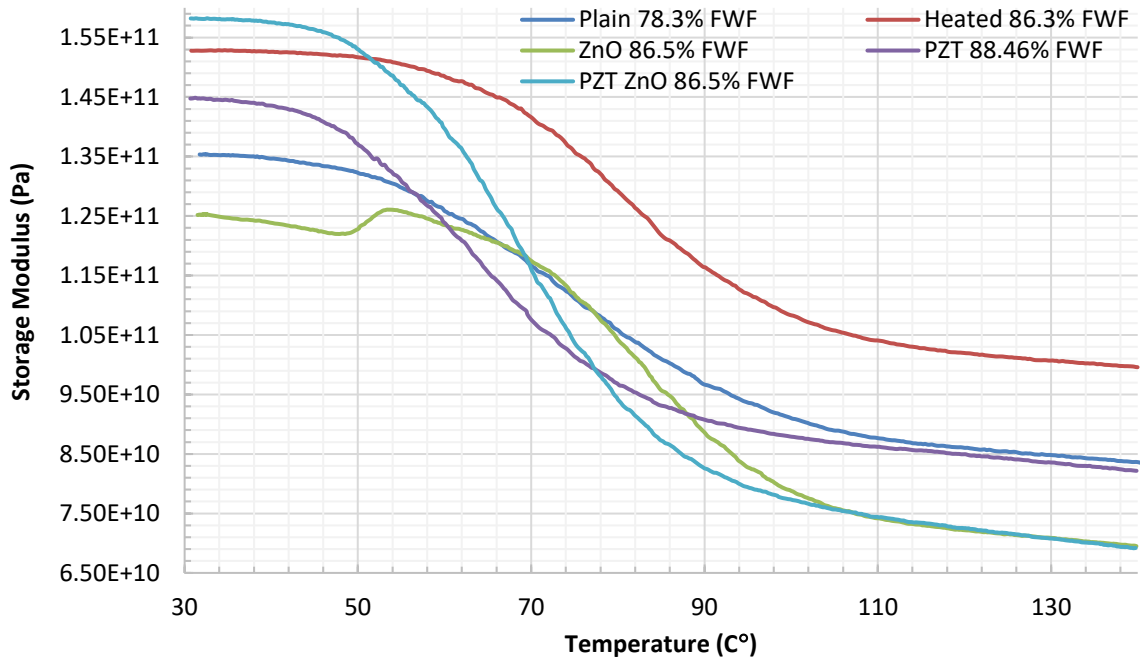
Figure 2-13. Storage modulus of the different FRPs measured from 30 to 140 C°.
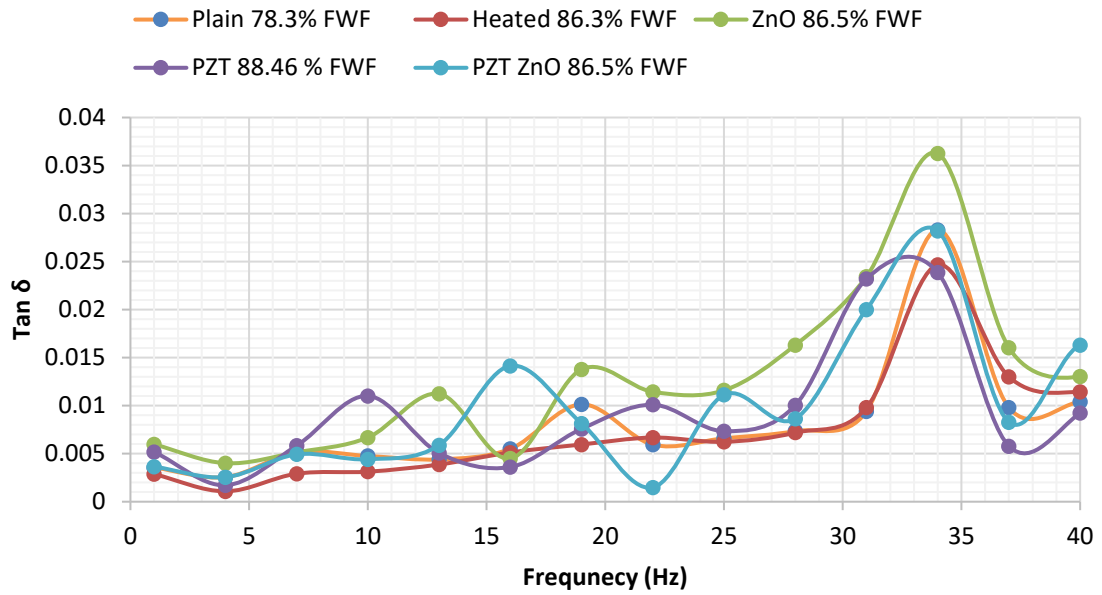
Figure 2-14. Tan δ for the different FRPs configurations measured from 1 to 40 Hz.
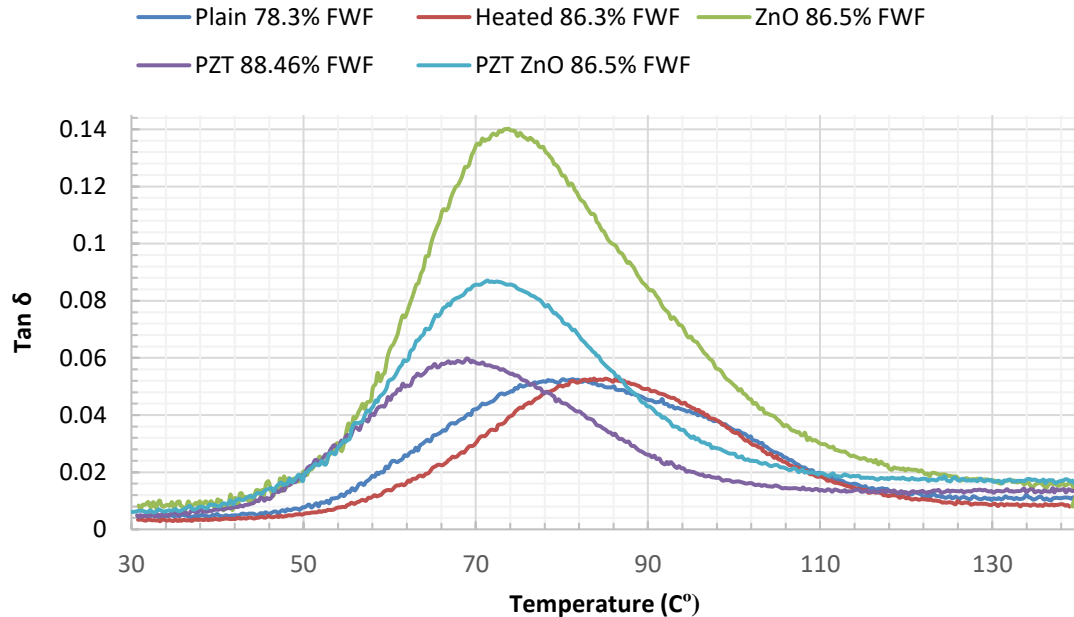
Figure 2-15. Tan δ for the different FRPs configurations measured from 30 to 140 C°.

In the results presented above, the respective fiber weight fractions (FWF) are shown. As seen in numerous different DMA-tests, the outcome is influenced by the FWF, where high fibrous composites are usually more elastic, stiff, brittle, and experience low damping characteristics (Dong & Gauvin, 1993); (A.Pothan, Oommen & Thomas, 2003); (Dutra, Soares, Campos & Silva, 2000).

For the storage modulus, the different FRPs follow this trend, where the materials with the higher apparent Young's modulus exhibit the highest storage modulus. However, this was not the case for FRPs with ZnO NWs, heat-treated cloths and one of the PZT sputtered cloths. The latter is most likely an outlier due to the limited amount of available data. As Figure 2-11 indicates, the composite sample based on the PZT sputtered cloth displays the lowest apparent Young's modulus, but also exhibits the second-highest storage modulus as shown in Figure 2-13. In Figure 2-13, the heat-treated specimens see an offset compare to the plain FRPs, which is not seen in Figure 2-12 nor

for Young's modulus in Figure 2-11.

Though both heat-treated and PZT FRPs show some offset likely due to a limit in the test data, the significant difference in pure ZnO NWs piques interest. The results correspond well with the limited amount of published research on DMAs on these hybrid composites. Skandani, Masghouni, Case, Leo, and Al-Haik (2012) and Boroujeni, Al-Haik, Emami and Kalhor, (2017) reported identical trends where the radially grown ZnO NWs on CFRPs interfacing layers enhanced the elastic modulus while drastically reducing the laminate storage modulus.

A drastic reduction of storage modulus is, nonetheless, compensated by an increase in the damping parameter, as seen in Figure 2-14 and Figure 2-15. This impact is not only seen when radially grown ZnO NWs are utilized but has also been observed, although weaker, for randomly grown ZnO NWs (Ayyagari, Al-Haik & Rollin, 2018).

Improvements in tan δ from a plain fiber composite was found to be 28.6 % at 34 Hz and as high as 168.4 % the glass transition temperature, for the ZnO NWs FRPs. The composite based on combination of ZnO NWs and PZT thin film showed only an increase of 10.3 % at 30 ℃ and virtually no increase at 34 Hz compared to the plain fiber composite.

From the literature, Skandani, Masghouni, Case, Leo, and Al-Haik (2012) saw an improved tan δ with their ZnO NWs hybrid composite of up to 50 %, while Boroujeni, Al-Haik, Emami and Kalhor (2017) reported an improvement of 47 % at their frequency-dependent DMA-studies. The distinction of tan δ found in this study could be credited to the production method, where the microwave process might have negatively affected the damping performance of the fibers. However, it is more likely that the high fiber fraction

reported in this study, where the ZnO NWs FRP here attained FWF of 86 % compared to 60 % for aforementioned studies, is accountable for the substantial discrepancy.

The results of Figure 2-14 are likely strongly influenced by this high FWF; smaller epoxy weight fraction resulting in poor bonding between the composite laminae leading to inadequate damping dissipation that is visible when performing the frequency sweep test. Dong and Gauvin (1993) have confirmed that there is a linear relationship between the loss of damping between laminae of a composites and its fiber volume fraction.

One further aspect worth pointing out is the negative impact the addition of PZT thin film has on the FRPs. While heat treatment in an inert atmosphere seems to have little to no effect, the PZT layer degrades the damping parameter by 15.4 % at 34 Hz and by 12 % at 1 Hz under 30 C°. The brittleness of PZT and its high stiffness, allowing only a minimal deflection and less energy dissipation, are likely behind these disparities.

The addition of ZnO NWs improve the damping drastically and furnish the FRPs with better damping characteristics than the plain composite. Damping enhancement are attributed to frictional slippage between the ZnO NWs and the polymer matrix as well as dissipation due to the piezoelectrical effect (Skandani, Masghouni, Case, Leo, & Al-Haik, 2012); (Küpfer & Finkelmann, 1991).

Therefore, with the incorporation of a PZT thin film, one would expect the piezoelectric supplemented damping to increase, which did not occur here, demonstrating that it is rather the frictional slippage the most influential contributor to the damping enhancement.

Finally, it is noteworthy that the infusion of ZnO NWs and PZT causes the

transient temperature of the FRP to shift backward, from around 81 C° to 74 C° for ZnO NWs FRP and 71.3 C° for the composite with ZnO NWs/PZT combination. Even though it is reasonable to assume that that intrusion of the piezoelectric nanophase in the epoxy matrix would slow down any creep and other heat influenced assets, the increase in thermal conductivity due to the addition of ZnO NWs and PZT is most likely countering this improvement (TurkoV, V., Rudyk & Rudyk, 2016); (Lee, Zhang, Bar-Cohen & Sherrit, 2014).

2.5 Conclusions

In this chapter, several synthesis routes and mechanical characterization techniques were utilized for improving the mechanical performance of hybrid fibrous composites (HFCs) based on one or two piezoelectric nano phases. The hydrothermal degradation of the FRPs, cost, and the production time could be reduced drastically by utilizing commercial microwave ovens. Mechanical tests showed that this process had no impact on ZnO NWs FRP when compared to previous research on identical HFCs.

Due to the potential enhancement of energy harvesting capabilities of hybrid composites by adding a PZT thin film, additional tests were performed to study its impact on an array of material properties. While a sputtered PZT thin film required additional heat treatment at high temperatures (650 C°), no degradation of the carbon fibers was reported. A combination of ZnO NWs coated with PZT thin film was shown to enhance significantly the stiffness of the material by 25.8 % compared to plain FRPs and 12.8 % compared to composites with ZnO NWs.

Composites with PZT thin film alone showed a degradation of 9.32 % in Young's modulus, which indicates that the synergy effects of combining ZnO NWs and PZT to the

FRPs are influential in terms of stiffness, storage modulus, and tensile strength. However, only a slight increase in damping, tan δ (10.3 %), was observed together with a decrease in the glass transition temperature for the new hybrid FRP (Tg dropped from 81 ℃ to 71 ℃), indicating that the enhancement of stiffness and potential piezoelectrical effects comes at a cost for the HFCs with combination of piezoelectric nanophases. .

3. INVESTIGATION OF HYBRID MULTIFUNCTIONAL DEVICES FOR ENERGY HARVESTING

3.1 Introduction

One promising feature of the HFCs is their energy scavenging potential from small mechanical excitations. Several promising devices were reported and were tabulated earlier in Table 1-3. The table present wide variety of achievable performances where Masghouni, Bourton, Philen, and Al-Haik (2015) reported performance peak of 3.4 mV and 24.4 nA compared to Pan, Li, Guo, Zhu, and Wang (2011) who reported the impressive performance of 3 V and 200 nA for their push device.

In this chapter, an investigation on how to achieve hybrid composites with enhanced energy harvesting performance is studied. By utilizing novel manufacturing routes, nanoelectrodes design, and proper materials combinations, better performing devices can be fabricated, which envisioned to bring the hybrid material technology closer to industry implementation.

3.2 Materials and Experimental Methods

The composites were prepared following the procedures outlined in Chapter 2. Three different device setups were prepared; based on carbon fibers with ZnO NWs alone, PZT thin film alone, and ZnO NWs and PZT combination while for analyzing the devices, several tools were utilized, such as electrical impedance analyzer, picoammeter, and a frequency response measurement setup.

Impedance is the measurement of resistance in a circuit exposed to current while voltage is transferred through the piezoelectric element. Under direct current (DC), impedance is strongly related to the resistance of a two-terminal circuit, but under an

alternating current (AC) the impedance possesses both magnitude and phases. Piezoelectrical materials usually exhibit a substantial impedance. In the current experiment, the impedance was measured using Hioki IM3570 (Hioki E.E. Corporation, Nagano, Japan).

An additional important aspect of the piezoelectric device performance is poling, as discussed in chapter 1. Simple tests were therefore implemented to see how poling affect the devices utilizing the presented test rig. Oscillating the beam at the 1st observable natural frequency, the peak performances were measured using a Keithley model 6487 Picoammeter (Keithley Instruments, LLC, Cleveland, OH, US) connected to LabView® interface through a GPID to USB connection.

From the literature (Frunza et al., 2011), (No et al., 2013), it was shown that poling is necessary for PZT despite being weakly polarized after the sputtering (Haccart, Cattan & Remiens, 2002). For ZnO NWs, however, the literature provides mixed suggestions. Masghouni, Bourton, Philen and Al-Haik (2015) and No et al. (2013) both poled their devices, while Chang et al. (2016) and Lin and Sodano (2008) achieved noticeable results without poling.

To study the effects of poling, a DC-voltage power source, Kikusui PMX35-3A (Kikusui America, Inc, Torrance, CA, US) was used to apply 30 V at different time intervals. After polarization was carried out, the devices were tested via different setups, namely; current tests and voltage data acquisition (DAQ) for frequency-response functions (FRF). The setups can be seen in Figure 3-1.
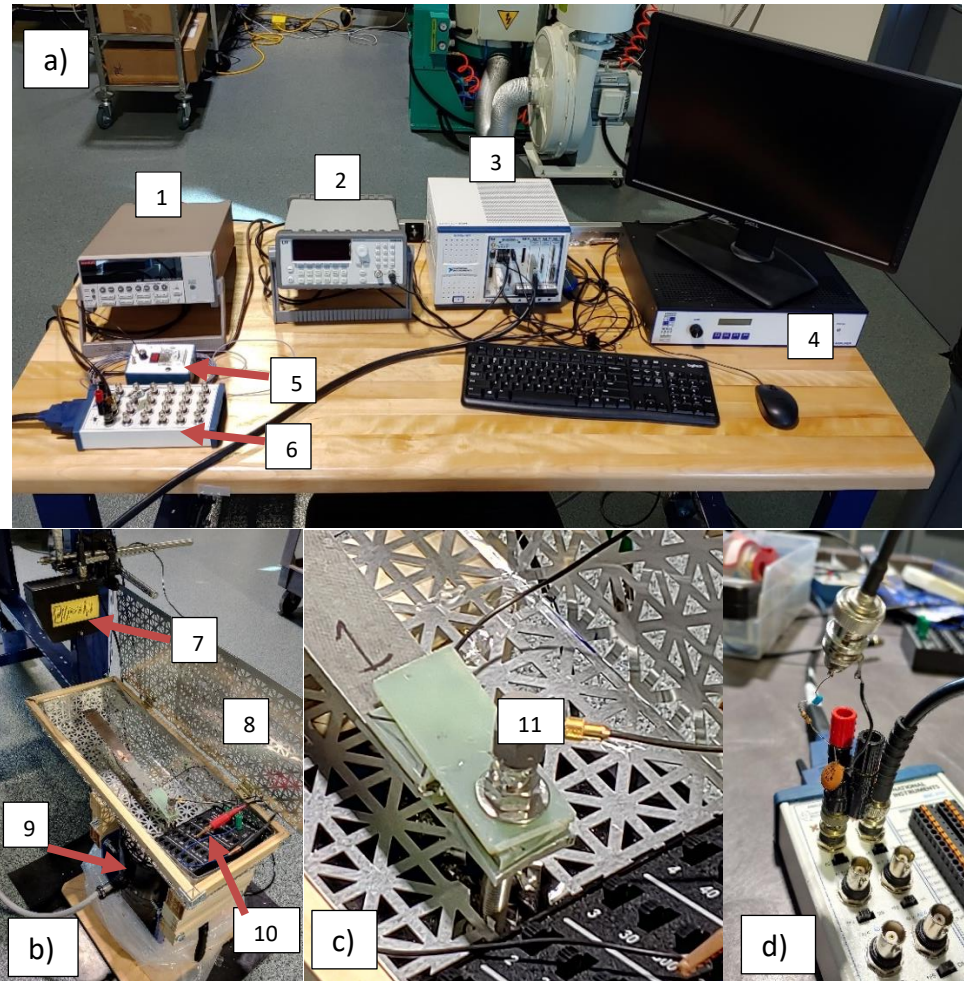
Figure 3-1. a) Data acquisition and control instruments, b) Setup of Faraday cage onto the shaker, c) Mounting for the accelerometer, and d) Modification of input for zeroing of signals with capacitors and resistances.

Table 3-1

Overview of Test Setup Types of Equipment

No.	Type and designation
1	Keithley model 6487 Picoammeter
2	Kikusui FGA5050 Waveform generator
3	Computer with NI-DAQ support and LabVIEW™ (National Instruments, Austin, Texas, US)
4	TMS 2100E21 Signal Amplifier (The Modal Shop, INC, Cincinnati, OH, US)
5	Model 480D06 Signal Amplifier (PCB, Depew, NY, US)
6	BNC-2110 Connector block, National Instruments
7	Laser, DTS-200-100 (MTI Instruments, INC, Albany, NY, US)
8	Faraday cage, self-made. Grounded.
9	TMS 2060E, Electrodynamic Shaker, The Modal Shop
10	Model RS-500, adjustable resistance box (Elenco Electronics, Wheeling, IL, US)
11	Accelerometer, Dytran Model 3055D1 (Dytran Instruments, INC, Chatsworth, CA, US) Sensitivity: 9.92 mV/g

Table 3-1 identifies the basic setups for the experiments. For necessary

performance testing, a picoammeter probed the current output of each configuration by

exciting them with the electrodynamic shaker. The picoammeter provides precise current

measurements but is slow and perform internal data processing and are therefore less

functional for frequency response function (FRF) measurements study.

For FRFs, instruments with little to no post-processing of the data are necessary.

Here the NI-DAQ system came in handy, where an accelerometer would monitor the

input enforced by the shaker, and proper circuit wiring directly on the device through a

variable resistance box would read the output from the device.

An FRF is a characteristic of a system response measured after applying a known

input. To carry out the FRF, one must measure the spectra of both the input force and the system vibration response. Setting X(jώ) as the input and Y(jώ) as the system output then the FRF denoted by H(jώ) is given by the equation (3-1).

$$H(j\omega) = \frac{Y(j\omega)}{X(j\omega)} \qquad (3\text{-}1)$$

The FRF represent a wide array of information about the device over a spectrum of frequencies and is an ideal methodology for characterizing the performance of each configuration while another vital signal processing tool here is coherence. Coherence, C_{xy} (sometimes called magnitude-squared coherence)is a statistic for examining the relationship between two signals; x and y and can adequately estimate the relation between the input and output data sets. Values of coherence are bounded such that $0 \leq C_{xy} \leq 1$, and any ideal linear input to output conditions would always equal to one. Signal noise or a non-linear relation between the output/input signals will lower the coherence.

Due to the limitation of the in-house built acquisition setup described earlier, a different system (Dr. Philen's group at Virginia Tech) was utilized. The acquired voltage levels of the device were in a low-noise spectrum of the DAQ-system above, and it was, therefore, necessary to use a more sensitive setup, as seen in Figure 3-2.
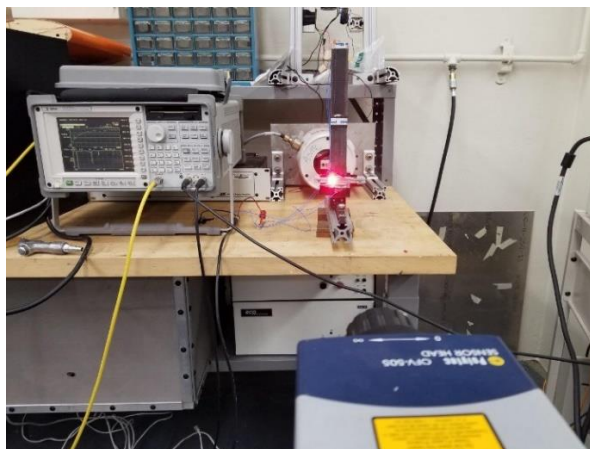
Figure 3-2. FRF setup for attaining higher sensitivity on the HFCs beams.

Here an Agilent 35670A dynamic signal analyzer (Agilent Technologies, Santa Clara, CA, US) was utilized to obtain the FRF and coherence of each composite beam device through recording the vibration speed with an OFV-505 laser system from Polytec (Polytec, Irvine, CA, US) pointed at the base of the beam device. The hybrid device was excited with a permanent magnet shaker, LDS V408, controlled by an LDS PA100E power amplifier (Brüel & Kjær, Nærum, Denmark). A Faraday cage could not be implemented in this part of the experiment.

3.2.1 Stepped ZnO Device

A device was built as shown in schematic Figure 3-3. This was of the same design that previously adopted by Masghouni (2014) with the idea that two side growth around the fibers would increase the energy harvesting potential.
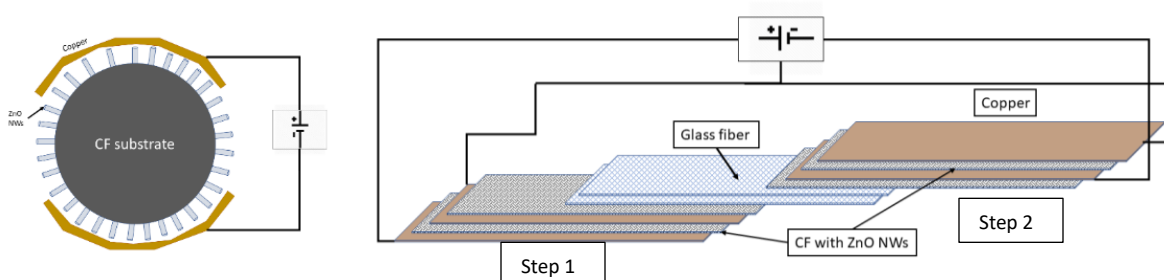
Figure 3-3. Schematic of the device on a fiber scale and overview of the full device scale.

Due to the limited size of the sputtering chamber (approx. 240x240 mm), a stepped beam design was chosen to produce a large enough structure that would verify the method at relatively low frequencies as well as each step required two layers of carbon fiber to be stiff enough not to bend, but still thick enough so the resonance frequencies would occur at the lower frequency bandwidth. For electrodes, 350 nm of copper film was sputtered on both sides at 75W and 3mT. By using conductive silver epoxy (MG Chemicals, 8331) electrodes with a thin copper sheet were prepared for later soldering of wires. Between each stepped layer of carbon fiber cloth, two-layer of glass fiber were inserted to isolate the steps and prevent the piezoelectrical effect from canceling each other out (Zhu, Worthington & Njuguna, 2009) when combining multiple piezoelectric devices.

After using a wet hand-layup process, applying vacuum and using the press to cure the device, abraded G-10 tabs were glued to one of the ends with the same resin used for the laminating, (i.e. Aeropoxy). The significantly stiffer tabs compared to the stiffness of the 2-layered beam would impose clamped beam conditions when the beam was later tested in a vibration shaker. Finally, beam segments were carefully cut out from the laminate using a tile saw. Water jet cutter use was avoided due to the toxic residue of PZT.

3.2.2 Stepped ZnO Device with Improved Electrodes

The initial stepped device outlined in section 3.3, was shown to provide a relatively low power level. An effort was invested to see that if the device itself can be enhanced into a more effective harvester. Ideas encircling circuiting on nano-level looks promising. For example, Pan, Li, Guo, Zhu, and Wang (2011) reported significant

increased harvested power gain by utilizing the carbon fiber itself as a circuit. Following on this idea, the circuiting was modified as shown in Figure 3-4.
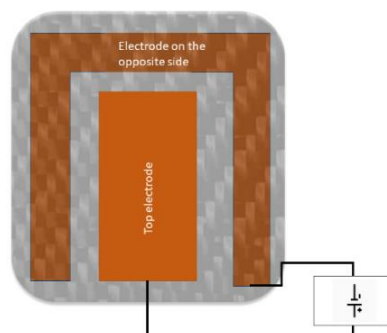
Figure 3-4. Illustration of how electrodes were applied on each step of the device.

In the illustration above, only the top electrode would be in contact with the top surface of the piezoelectric material, while the bottom electrode for the ZnO NWs would be contacting the carbon fibers. Carbon fiber itself is a highly conductive material, and the 6000k HexTow™ IM7 exploited in this research possesses an electrical resistivity of 1.5×10^{-3} ohm-cm; compared to 1.68×10^{-6} ohm-cm for copper.

Utilizing the carbon fabric as one electrode is beneficial in obtaining a better electrical connection between the ZnO NWs and its substrate. Based on this concept woven sheet with ZnO NWs grown only on one side was prepared as specified in chapter 2. The side covered with ZnO NWs, had a 350 nm thick copper layer magnetron-sputtered, while the opposite side has a stream of copper encapsulating the top electrode. Cardboard was used to mask the surface cover. See Figure 3-5.

Figure 3-5. Samples after being sputtered by copper and prepared with electrodes.

Silver epoxy (MG chemicals, 8331) was then employed to bond copper strips for later wiring. The fiber circuiting for the device is illustrated in Figure 3-6.
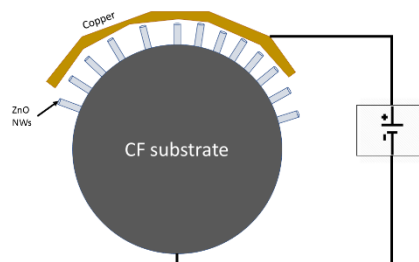
Figure 3-6. Fiber scale circuit modeling for the revised ZnO NWs device.

The final device was set up and manufactured in the same manner, as shown in section 3.2.1.

Figure *3-7* shows how the device was layered during the hand-layup in process.

Figure 3-7. Wet layering of the stepped device with refined electrodes

3.2.3 Devices With PZT Thin Film

Due to the success of the revised electrode device, as shown later, both the PZT

including devices, were manufactured using the same setup. Their fiber wise circuiting is

shown in *Figure 3-8*. It is assumed that the PZT thin film circumference the ZnO NWs.
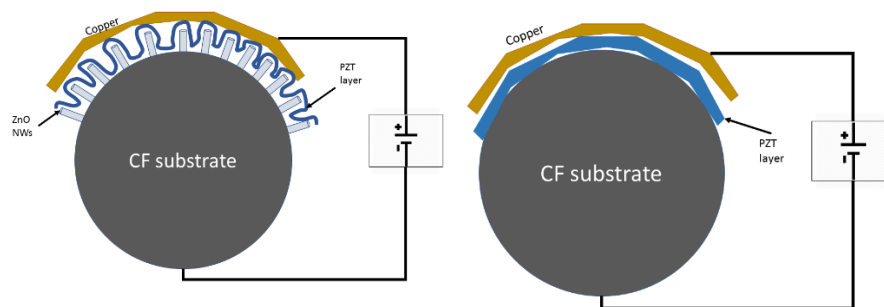
Figure 3-8. Fiber circuiting for the different setups with PZT layer.

3.2.4 CF Beam with Commercial PZT Patch

Due to the lack of relevant literature on energy harvesting with a simple piezoelectrical patch glued on a CF-laminated beam was designed for benchmarking of equipment and later FE-analysis. The benchmark device consisted of plain carbon fiber laminates produced in the same way illustrated in chapter 2. A PZT Navy II patch from APC International, Ltd. (Makeyville, PA, US) was glued on top of the beam section cut from the original laminate. The patch was glued close to the clamped end of the (186mm×18mm×0.5mm) beam using silver epoxy (MG chemicals, 8331) as shown in Figure 3-9. For beam fixture at the clamped edge, two Abraded G-10 tabs were bonded to each side of the end using the same resin (i.e. Aeropoxy) shown before.

Figure 3-9. Simple CF-beam with a commercial PZT patch glued close to the clamped end

3.3 Results and Discussion

3.3.1 Effect of the Faraday Cage
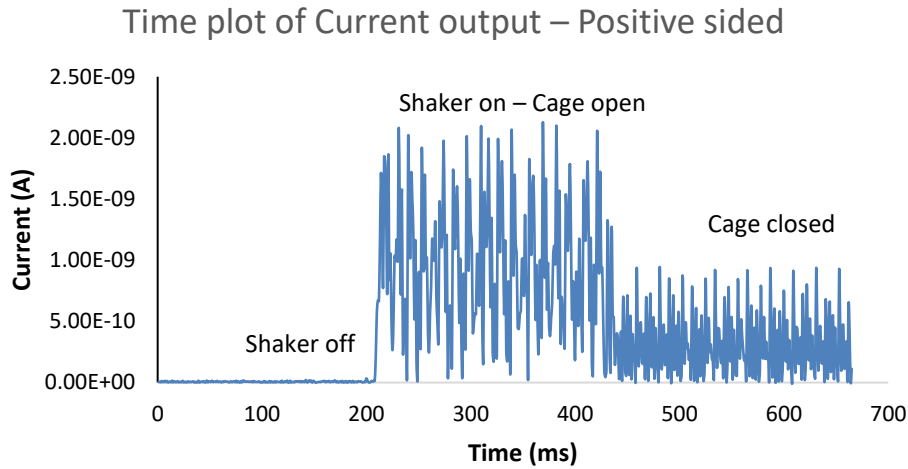
Figure 3-10. Plot indicating the efficiency of eliminating external noise by the Faraday cage.

Impact of the Faraday cage can be seen in Figure 3-10. While the TMS 2060E electrodynamic shaker was quickly pinpointed to be the most significant external source of noise, the Faraday cage effectively eliminated a substantial amount of it.

3.3.2 Impedance Measurements of The Devices

The measurements from the impedance analyzer of each method are shown in Table 3-2 where Z denotes impedance, C_s is static capacitance, R_{dc} is DC resistance, and R_s describe active resistance in series. The numbering of the types describes each device number, while the second number describes which step on the device from the clamped edge of the device. 01 denotes the step closest to the clamped edge, while 02 is the step at the free end.

Table 3-2

Overview of Device Impedance, Capacitance and Resistance

No.	Type	$Z(\Omega j)$	$C_s(F)$	$R_{dc}(\Omega)$	$R_s(\Omega)$
01-01	ZnO first type	0.688	-0.032	0.688	0.688
01-02	ZnO first type	0.008	-0.024	0.008	0.008
03-01	ZnO first type	0.793	-0.021	0.792	0.792
03-02	ZnO first type	6.54	-37.5n	6.06	6.53
01-01	ZnO new design	9.72M	0.162p	nAn	0.215M
01-02	ZnO new design	2.136	-19.6m	2.13	2.13
02-01	ZnO new design	634.263	2.04m	635.02	634.00
02-02	ZnO new design	3.23	-2.55	3.22	3.22
03-01	PZT and ZnO	26.48	0.091	26.54	26.54
03-02	PZT and ZnO	2.88	-0.021	2.88	2.88
05-01	PZT	10.99	-30.7	11	10.99
05-02	PZT	1.1k	0.3m	1k	991
07-01	PZT	2.65	-27.6k	2.65	2.65
07-02	PZT	491.9	-2.25	507.7	489.5
08-01	PZT and ZnO	12.56	-39m	12.11	12.56
08-02	PZT and ZnO	1.85M	0.987n	15M	0.262M

For piezoelectrical devices, a higher impedance number Z means a better achieving device. Usually, the capacitance should be in the pico Faraday (pF) range. It was, therefore, surprising to see most of the devices accomplish impedance values in the lower spectrum. Previous research (Masghouni, 2014) reported an impedance of 10.75 MΩ and capacitance of 0.472 pF for ZnO NWs devices. Only some of the steps in this study gave the same reading indicating either short-circuiting or low piezoelectrical performances.

3.3.3 Poling of Devices

Due to the discussion in the literature provided earlier on the efficiency of poling, a small poling test was conducted as shown in Table 3-3, which show the peak measured current. The measurements were taken during a 2 to 20 Hz sweep using the Keithley 6487 picoammeter and with a 1M Ohm resistance in series with the device.

Table 3-3

Poling test of different setups

Device type	No poling	15 min	30 min	45 min	60 min
ZnO	1.19nA	1.82nA	4.69nA	2.09nA	1.94nA
PZT	5.15 nA	6.17 nA	8.27 nA	8.47 nA	8.97 nA
ZnO + PZT	25.2nA	28.8nA	33.7nA	33.1nA	29.4nA

The table above demonstrates that poling has a significant effect on all the materials combination investigated in this section. Interesting enough, the ZnO NWs seems to exhibit the largest percentage gain due to poling with a 294.1 % increase from 0 to 30 min. The pure PZT sputtered device achieved a 60.58 % gain, while the ZnO NWs and PZT device reported a 33.73 % increase. The large difference in gain could somewhat be attributed to the limited number of devices purposefully tested for poling results, but other factors are likely influential.

ZnO NWs are reported to be self-polarized due to their unique molecular build up (Baruah & Dutta, 2009) where strong opposite electrical fields are reported on each end of a NW. It is not unlikely that a poling will align these polarized faces of the NWs in the same direction, and thus attributed to the percentage gain. However, ZnO NWs experience a current peak loss after 30 min indicating that at a certain time threshold the

polarization is breaking down the naturally self-polarized nature of the NW.

Sputtered and sintered PZT thin films are reported to be partly polarized due to the random alignment of material grains after a sputtering process Frunza et al., (2011) reported as well good polarization results for their PZT thin film after 30 min poling at 30 V. The loss of gain after 30 min could be attributed to breakdown of polarities in addition to cracking due to additional residual stresses induced because of the orientation switching as discussed by Marshall et al. (2011). They reported a 121% change as well due to polarization, which agree well with the results here considering their experiment were done on silicon substrates.

Finally, the ZnO NWs and PZT combined device likely experienced a combination of the aforementioned factors, while the highly non-uniformity of the combined material likely introduce a high degree of random polarization which bolster the natural piezoelectrical affect the non-smooth surface of the material combination make polarization less effective, as discussed by several authors experimenting with PZT thin films (Marshall et al., 2011); (Baruah & Dutta, 2009); (Liu et al., 2011).

3.3.4 Current Sweep From 0.1 to 80 Hz

The Keithley 6587 picoammeter was preset to the current at a rapid rate. The waveform generator was set up to perform a frequency sweep from 0.1 to 80 Hz with an amplitude of 500 mV. With the amplifier for the electrodynamical shaker set to ¼, this would in terms of acceleration represent approximately 2g of input force.

All the devices were running in three different setups with one for each step, and later, each step in parallel (parallel circuits increase current flow) utilizing the variable resistance boxes preset to 1M Ohm. The current tests had two purposes. First, to

experimentally verify the generated charge of the device, but as well to nullify that the overall small output electrical signal is artificially produced charges and not piezoelectrical.

Here, a protocol developed by Wang (2008) came in handy. The linear superposition model they proposed is stating that the output current should increase linearly when two or more devices are connected in parallel. The reasoning behind this is that resistors, capacitors, inductors, and diodes do not show the linear superposition effect and therefore, a piezoelectrical device must be behind the increase.

It should be noted that the measurements were initialized manually and that the picoammeter commence a fair degree of post-processing of the data before sending it to the acquisition software, LabVIEW©, making it necessary to manually fit the plots from each step and the parallel setup, introducing potential offsets. The scenarios should therefore only be considered as confirming trends and not considering the magnitude. In Figure 3-11 the circuit diagram is shown.
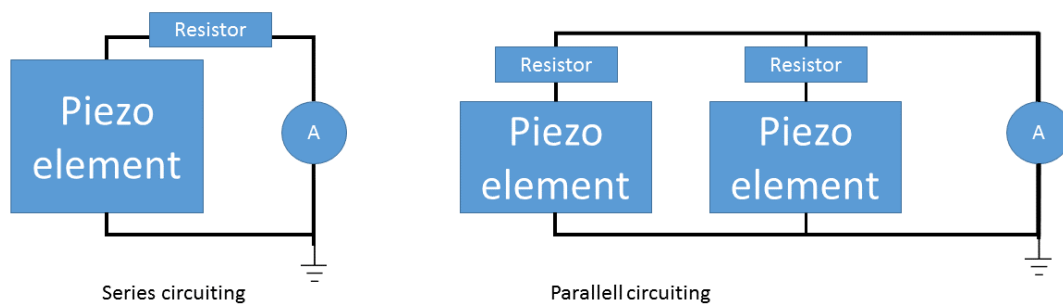
Figure 3-11. Circuiting for the current analysis.

First ZnO NWs Device
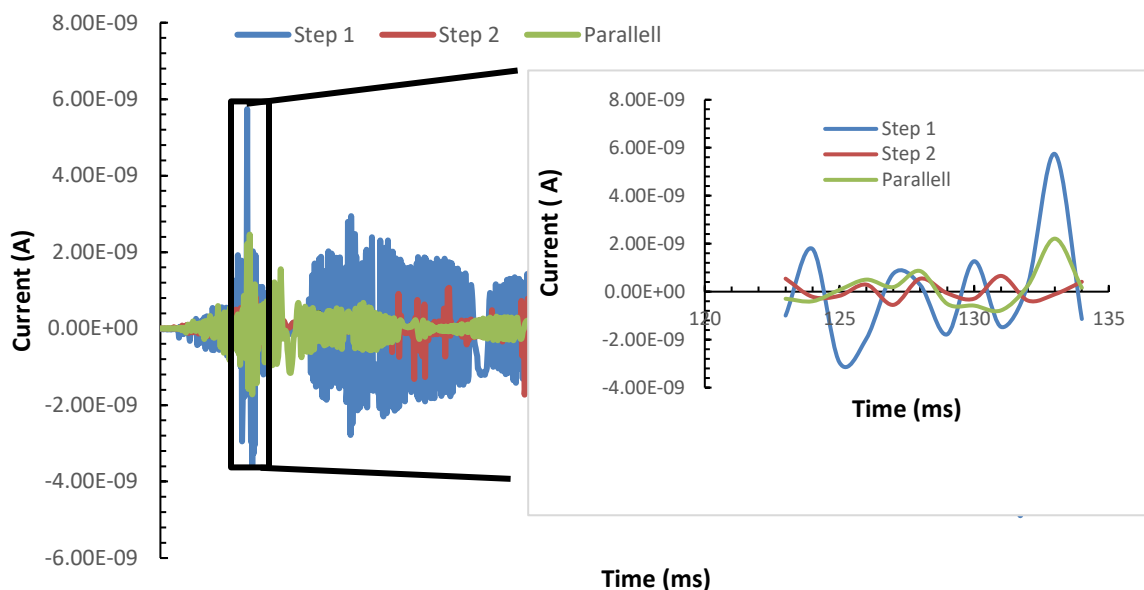
Figure 3-12. Overall output from the first stepped device no 03, with a focus on a smaller dataset (right).

Following the protocol by Wang (2008), this device is either faulty or does not possess significant piezoelectrical effects. The registered current is very low and lay only 1nA over the registered value for noise, as seen in Figure 3-10. The impedance for the first ZnO NWs devices were low, indicating a short-circuiting that would make the machine faulty. Maximum peak-to-peak current, registered for Step 1, which is not centered around zero, amount to 9.3nA.

ZnO NW Device – Revised Electrodes

For the rest of the devices, only a smaller timeframe was extracted for the overall time set to study the maximum output from the device. Due to the internal processing by the Keithley 6487 picoammeter before data acquisition, estimation of the frequency would prove to be arduous. For all the plots, there is a visible shapeshift from the 1 step, 2 steps, and parallel. This can be attributed to the instruments processing, moreover to how each step circuit interfere with the current phase when they are in a parallel circuit.
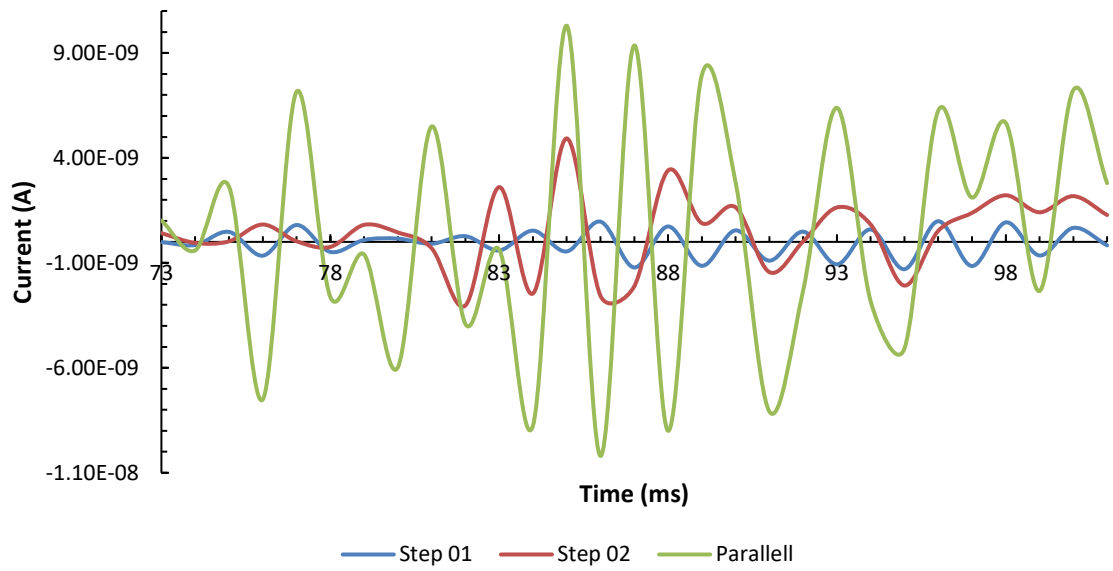
Figure 3-13. Current readings from the revised designed beam 01.

PZT Only Device
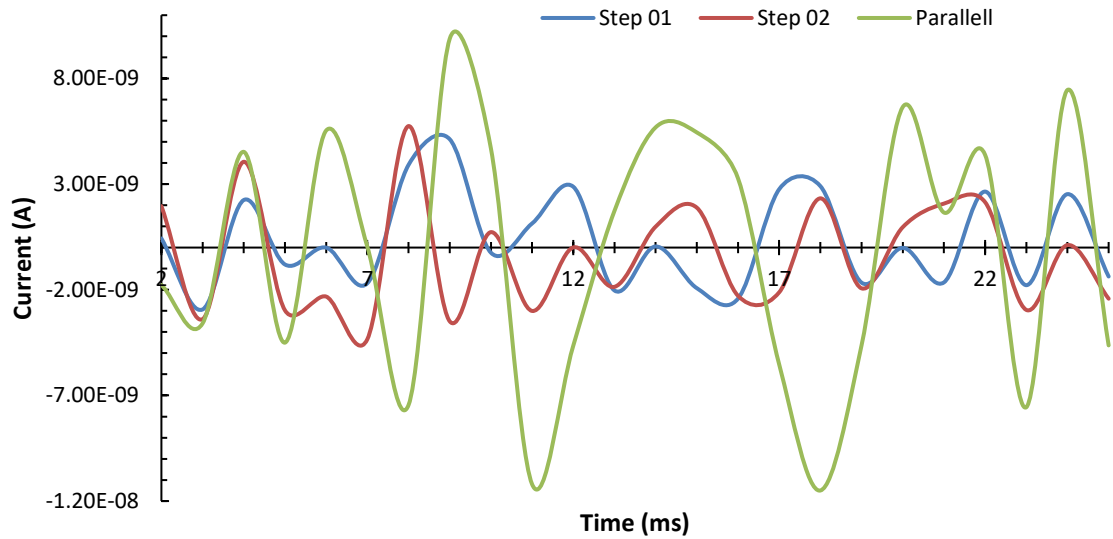
Figure 3-14. Current text from the revised PZT single device no 05.

PZT & ZnO Device
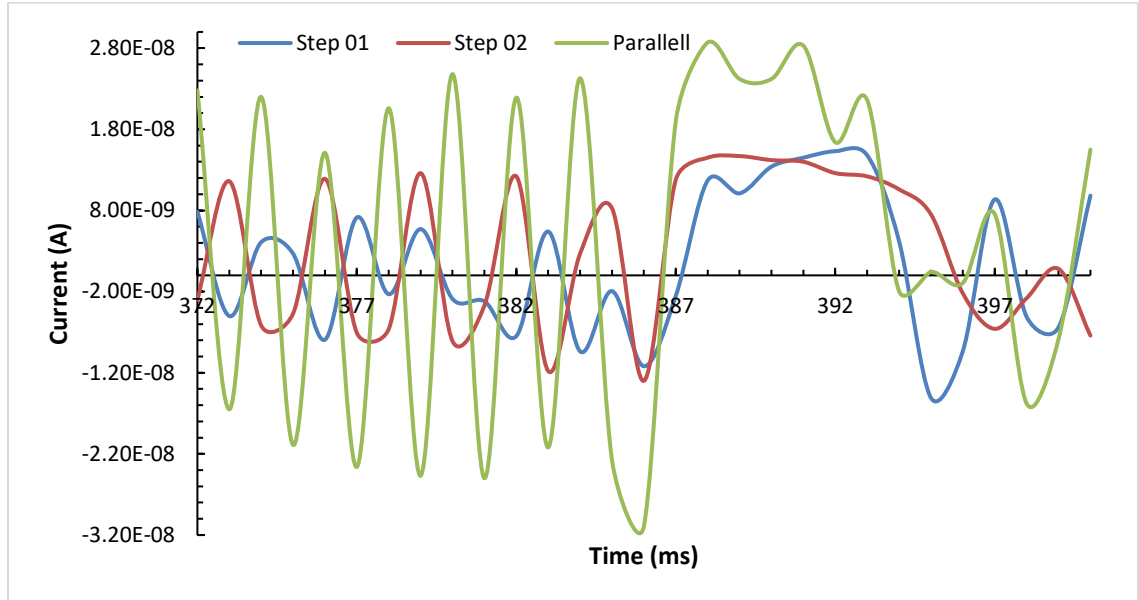
Figure 3-15. Current readings from the combined ZnO NW and PZT device no 08.

Figure 3-13, Figure 3-14 and Figure 3-15 indicate that a piezoelectrical effect is taking place. Table 3-4 tabulates the maximum output currents and power in terms of Watt. (W). The power was calculated from the measured current and the equivalent resistor from each device step defined by eq 3-1 and 3-2, subscript T denotes the total circuit.

$$R_T = \frac{1}{R_1} + \frac{1}{R_2} \tag{3-12}$$

$$P_T = R_T I_T{}^2 \tag{3-2}$$

Table 3-4

Tabulated maximum peak to peak currents taken from parallel circuiting $R_{1\&2}$=1 MΩ

Device type	Peak-Peak max current	Power	Increase to ZnO NWs
ZnO NWs	20.5 nA	0.2101 nW	---
PZT	24.6 nA	0.3026 nW	44.00 %
ZnO NWs & PZT	59.2 nA	1.7523 nW	733.94 %

The results correspond well with identical trends seen for experiments by other research groups, section 1.7, where ZnO NWs have been combined with other piezoelectrical materials. As seen in Table 3-4, the device utilizing combination of ZnO NWs and PZT thin film exhibits synergy in power generation by drastically surpassing both the performances of the ZnO NWs and PZT thin films individual devices promptly establishing the viability of the hybrid devices.

However, the nature of the measurement techniques makes the outcome only useful to verify performance trends and overall conformability to the proposed procedure earlier to check that the device is piezoelectrical. Therefore, it became necessary to employ other performance measuring techniques to draw more conclusive results.

3.3.5 FRF of The Devices

For taking FRF, the NI-DAQ system was utilized together with the variable circuit box in series with the device. The composites beams were exited using the same electrodynamical shaker as described earlier under a 2g load. A power spectrum of the input data shows that the acceleration input was stable for most of the frequency spectrum.
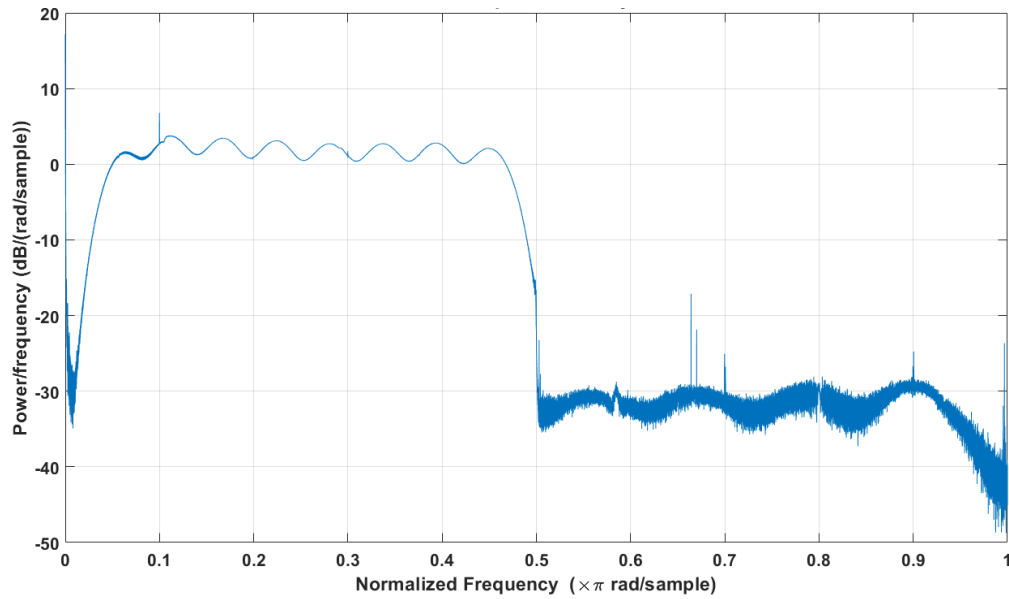
Figure 3-16. Power spectrum of the acceleration input.

The Welch power spectral density estimate plots in normalized frequencies, which is necessary to convert to regular frequency based on the sampling frequency, see equation (3-3).

$$freq = normalized\ Hz * sampling\ Hz \qquad (3\text{-}3)$$

From the plot, the shaker will input a relatively flat spectrum from 62.47 Hz to 560.16 Hz. The sampling rate was at 1200 samples per second (s/s). The readings and relevant FRF data will be presented for each device below.

Benchmark Beam

The input to the shaker as well as the readings from the patch are shown in Figure 3-17 and Figure 3-18 together with its respective FRF. This data will be further discussed in the next chapter. The input readings were taken with a resistance of 2.0kΩ in series with the patch. The results of this device will be detailed in section 4, as part of the FE-analysis.
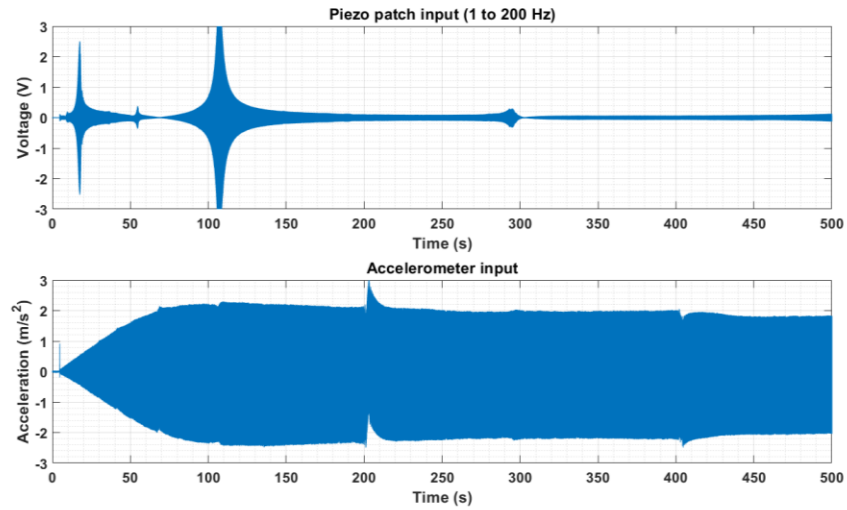
Figure 3-17. Readings received from the piezo-patched based on applied input (acceleration) by the shaker.
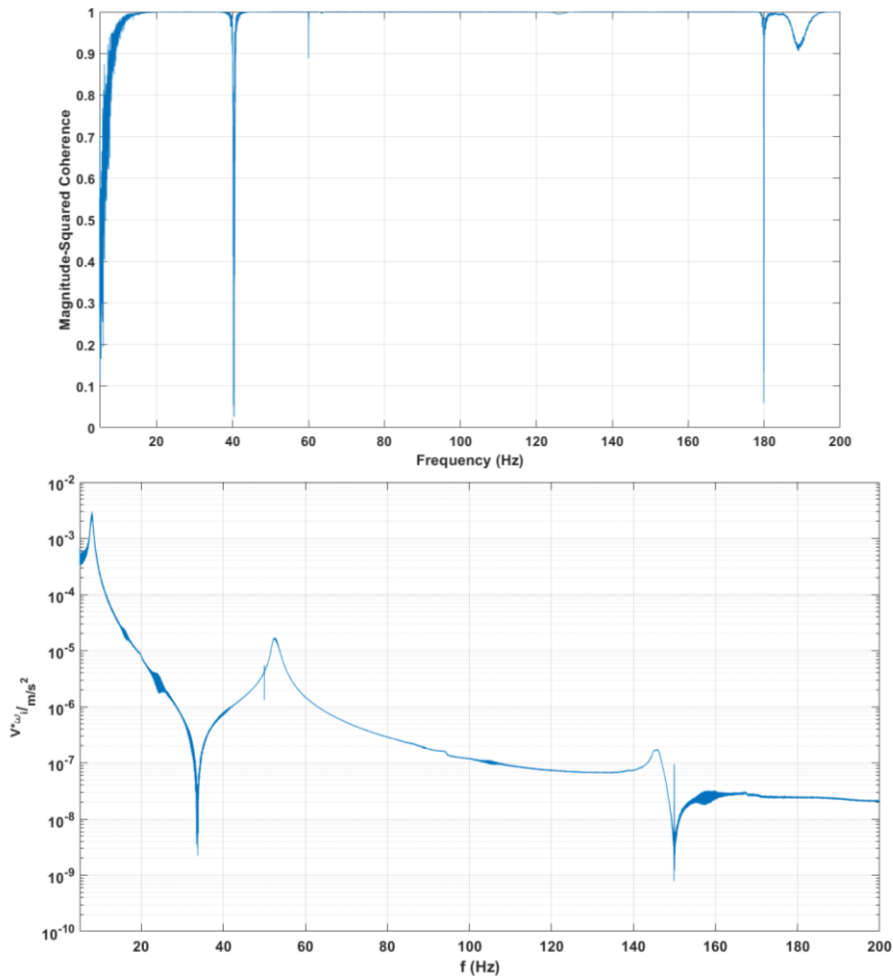
Figure 3-18. Coherence and FRF for the benchmark problem for a specter of 1 to 200 Hz

ZnO NWs Stepped Device
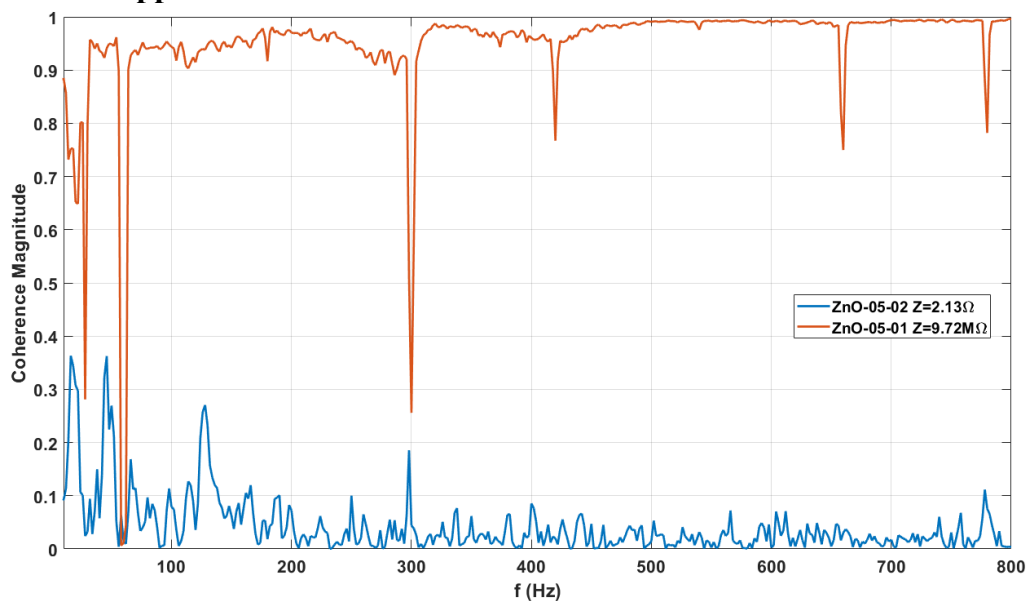
Figure 3-19. Coherence for stepped ZnO NWs device.
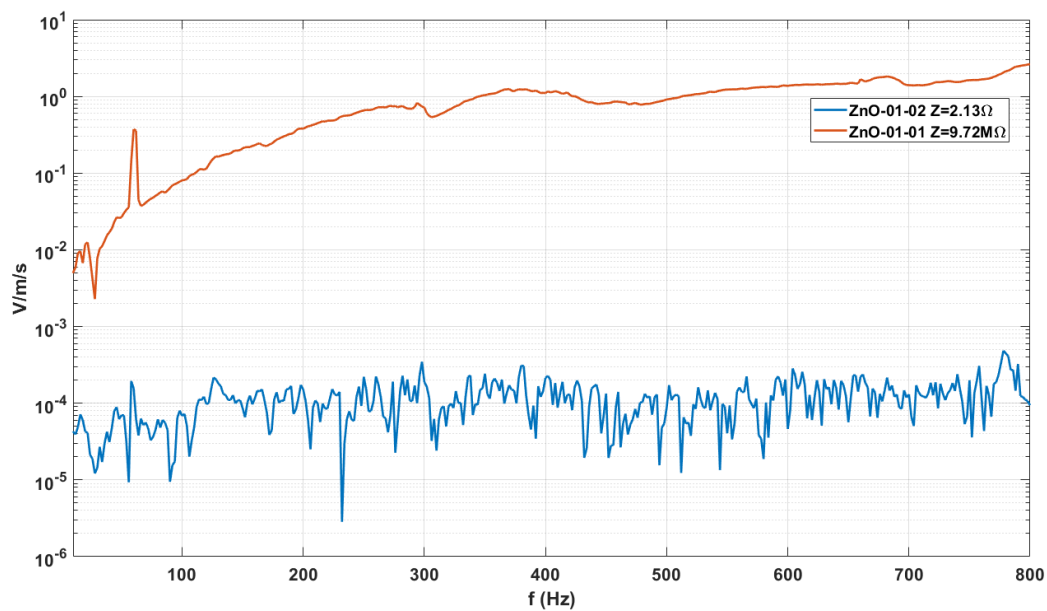
Figure 3-20. FRF for stepped ZnO NWs device

PZT Stepped Device
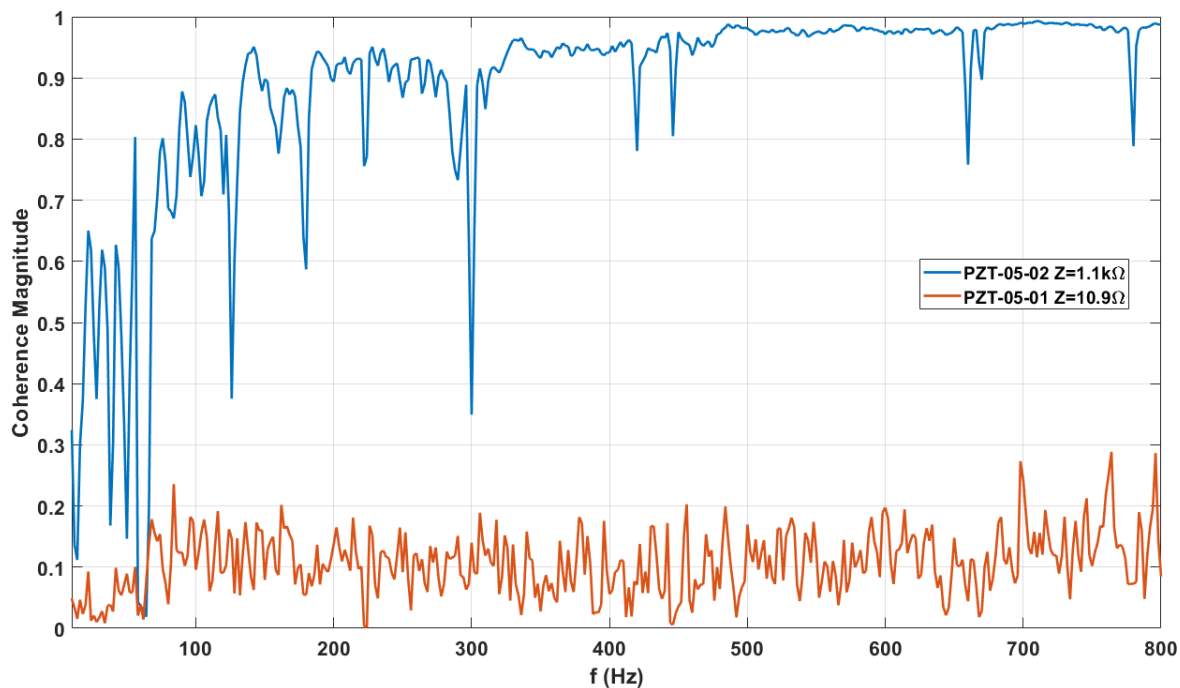
Figure 3-21. Coherence for the PZT stepped device.
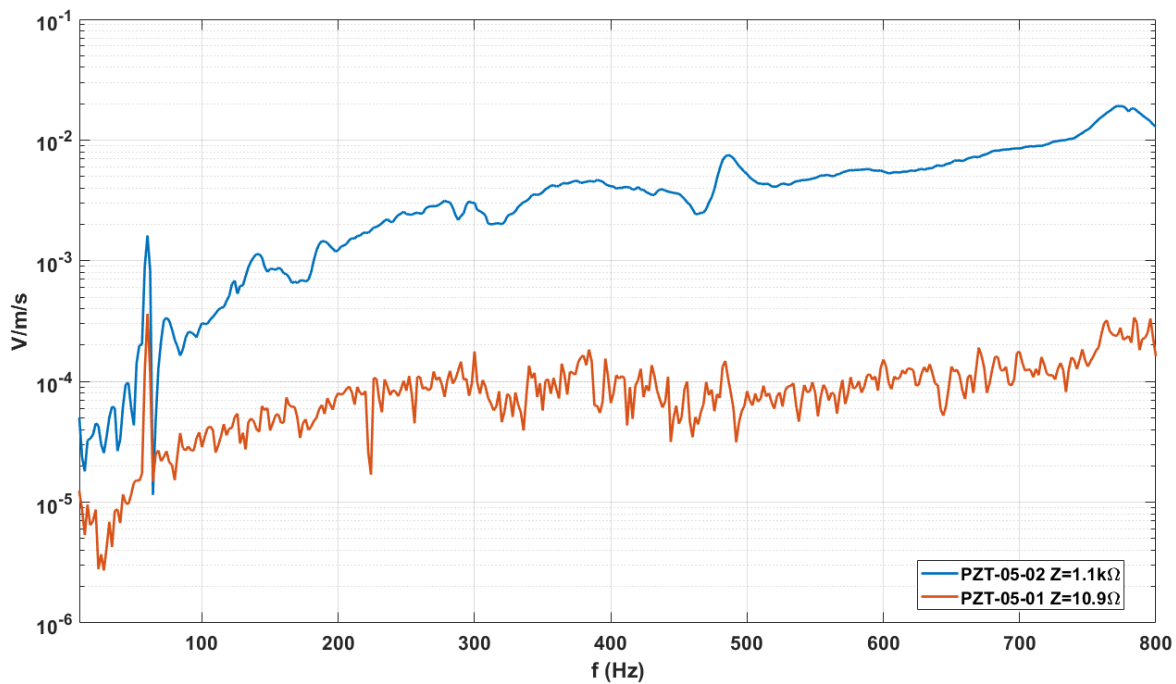
Figure 3-22. FRF for PZT stepped device.

ZnO NWs and PZT Device
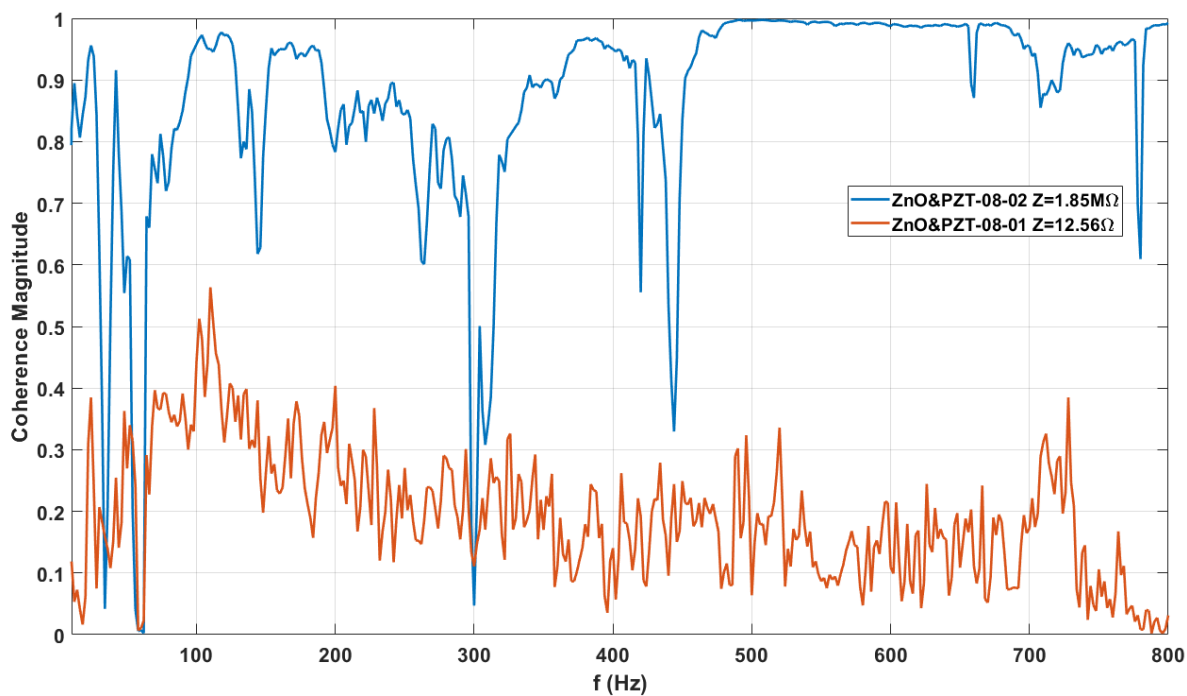
Figure 3-23. Coherence for ZnO NWs and PZT combination stepped device.
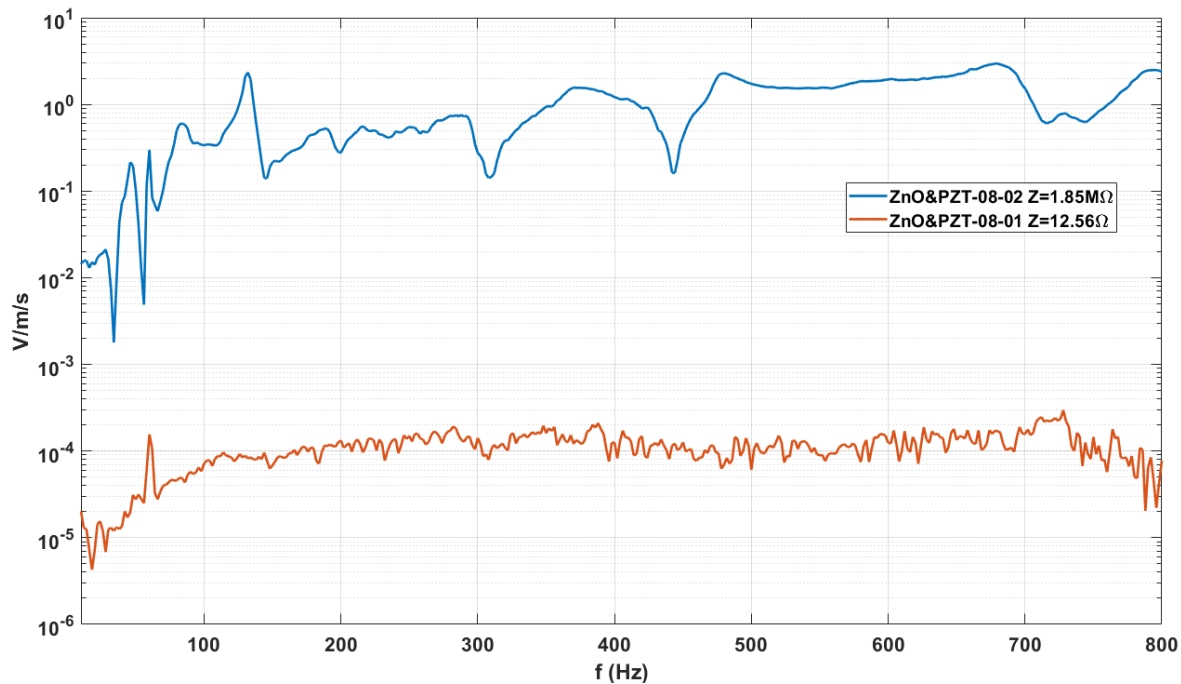
Figure 3-24. FRF for ZnO NWs and PZT combination stepped device.
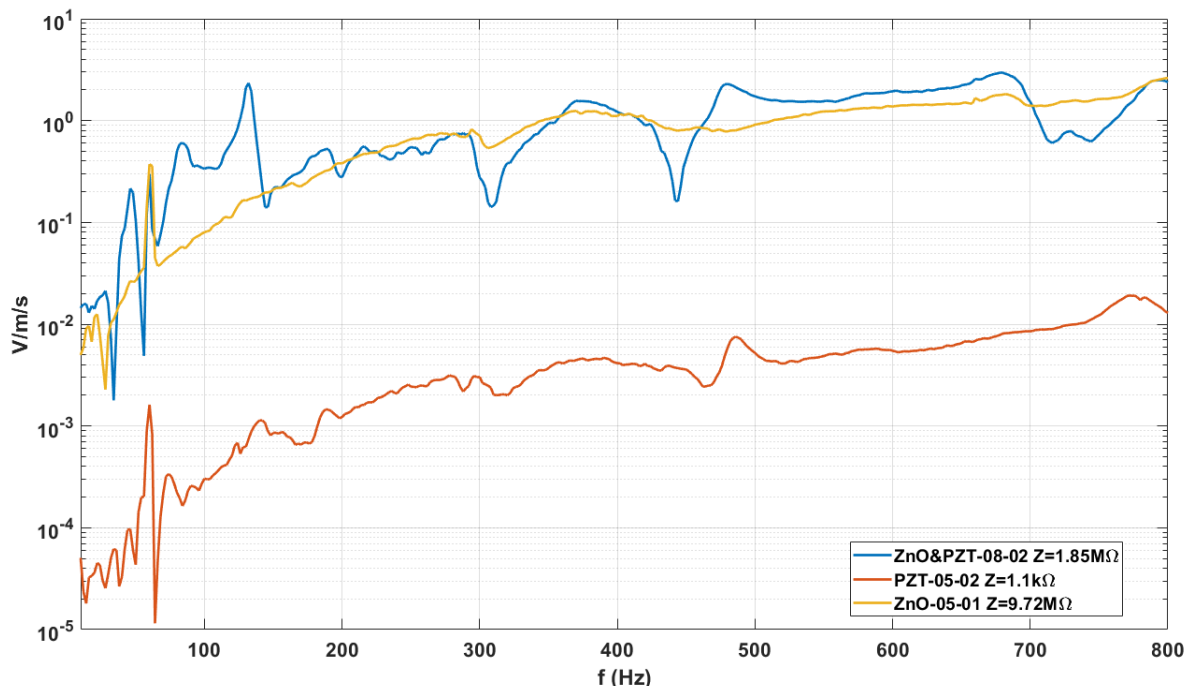
Figure 3-25. Comparison of the best performing device steps.

The FRF and coherence results show several noteworthy trends and elucidate the overall performance of the different devices over a broad spectrum of frequencies, which is an excellent base for further discussion. Neither the FRF nor coherence have been post-processed and are therefore showing the raw output of the device. The measurements were taken without a resistance load, and the power level achieved could therefore not be reported.

First, both the ZnO NWs and the combination device perform several orders of magnitude better than the pure PZT thin-film device. The ZnO NWs and PZT devices are particularly superior at the lower frequency band (up to 150 Hz). At best performance, the combined device delivers 2.961 V/m/s (at 680 Hz), a 47.63 % improvement over the ZnO NWs device which peaks perform up to 1.822 V/m/s (at 682 Hz). The difference in performance to the previous power taken from the current measurement could be attributed to several factors. In contrary to the pure ZnO NWs device step, the combo

device has its highest-performing level on the opposite side of the clamped end (step 2), and the steps were tested individually and not in series/parallel as earlier. Moreover, a lower impedance value for the combo device implies that an ideal device is still achievable. The first limitation here is of "superior" importance, as the induced strain at the clamped end is significantly higher than what seen at the free end. It is, therefore, safe to assume that a working combination device activated by the higher induced strain at the clamped edge will be superior to the pure ZnO NWs device.

The results pinpoint one of the significant issues of working with the nano infused piezoelectric devices as discussed here. As can be concluded, the difficulties of successfully isolating the piezoelectrical layer and avoid any short-circuiting are detrimental to the overall performance of the device.

Despite the limitation in the amount of sample data, the experiments have verified and highlighted several other noteworthy trends. More work on successfully engineering the circuiting could be worthy in improving the devices considerably without altering the materials used in this research.

Particularly noticeable is the hybrid composites ability to achieve higher input levels at high frequencies, in contradiction to patch based energy harvester that sees significant harvesting loose at higher frequencies, as evident in the benchmark problem. This high-frequency performance seems to agree well with trends observer by other research in hybrid-composites.

To have functioning devices in higher frequency spectra has several positive attributes. First of all, most of the aerospace structural system endure frequencies at the higher spectra (engine vibrations, shock loads, forced vibrations, etc.), which demonstrate

that these devices can harvest the vibration as mentioned above more efficiently.

Due to the limited relevant work available to compare the data with; Masghouni's (2014) work must be scrutinized again. Compared to that work, the devices developed here (other than the PZT device) exhibit better energy harvesting performance. He reported a maximum voltage output of 0.01 V/m/s with a resistor of 10.0 Ω, which is tremendously lower than what is reported for the ZnO NWs device here. The measurements taken here were carried out with an open circuit with no resistive load, but at 10.0 Ω that has nearly a negligible effect, leading to an evidence-supported conclusion that the process and design utilized in this thesis show great promises to the device.

Finally, for all the performance data plots, a stiff peak at around 60 Hz is observed. This is external noise from the electrical grid and can be ignored for all practical concerns related to this experiment.

3.4 Conclusions

In this chapter, several novel approaches and solutions have been verified to pave the road for further promising research into better performance hybrid composite energy harvesting devices. A considerable amount of work related to making efficient devices and benchmarking procedures that can verify the performance of the different hybrid devices with nano-piezoelectrical material infused were outlined.

From these methods, it was proven that the quick and low-cost growth of ZnO NWs with household microwave show decent, and even better, harvesting results compared to published hybrid composite research. New methods of enhancing the piezoelectric characteristics of the devices were probed. Here, a combination of ZnO NWs grown radially onto carbon fibers with a 200 nm PZT thin film sputtered on top

showed synergistic results. Neither the device, nor the circuiting were fully optimized for highest possible performances. The best device based on ZnO NWs/PZT combination achieved an open circuit voltage FRF of 2.961 V/m/s and parallel step circuiting of 1.75 nW. This amount to a 47.63 % increase in voltage and a 733.94 % increase in power compared to the pure ZnO NWs device. The pure PZT device achieved relatively mixed results, proving that the combination draws synergy effects enhancing both the PZT and ZnO NWs.

Considering the thickness of the piezoelectrical layers in this study (nanometers for PZT and sub-micron for ZnO NWS) and the possibilities of implementing this over several layers, together with further optimization of the applicable circuiting. The results show great promises into taking hybrid composites a further step into practical applications.

4. **FINITE ELEMENT ANALYSIS OF HYBRID COMPOSITES ENERGY HARVESTING CAPABILITIES**

4.1 Introduction

Finite Element (FE) method has been shown to be a versatile tool in analyzing the behavior of piezoelectric materials, multifunctional materials in addition to hybrid composites. Karagulle, Malgaca and Oktem (2004) showed how well ANSYS® simulations agree with their analytical vibration control results for a beam with a piezo material patch. Khalatkar, Gupta and Agrawal (2014) revealed that a piezoelectric patch on a beam analyzed using ANSYS® can be compared to experimental results exited at a given frequency.

Yang and Tang (2009) demonstrated furthermore how well FE compares with their analytical models for a wide variety of different patched beam designs with either multiple patches on rectangular-shaped beams or of trapezoid shapes. The models were compared over a defined range of frequencies through employing ANSYS® FRFs.

Finite element model effectiveness for a patch bounded to a plate over ranges of frequencies has been carried out by Bayik (2016) and Paknejad, Rahimi and Salmani (2018) showed how well their analytical solution for a composite plate with a patch performed compared to the numerical solution using ANSYS®.

On finite element analysis utilizing theories of coupled analysis with composite laminated plate theory, Detwiler, Shen and Venkayya (1995) showed in their work that the setup corresponded well with experimental and numerical results. Similar work was conducted by Narayanan and Balamurugan (2003), but has not been verified in ANSYS®.

Other researchers have focused on the micromechanical finite element analysis aspects. Dauksevicius, O'Reilly and Seifikar (2015) presented modeling for a single ZnO

NW. Berger et al. (2005) performed modeling of PZT-fibers embedded in a soft polymer, while Malakooti, Zhou and Sodano (2016) demonstrated the micromechanics modeling of hybrid multifunctional composite comprising carbon fiber with piezoelectric coating and matrix. Similar work was carried out by Masghouni (2014).

Nevertheless, far less demonstrations have been published where the numerical or analytical analysis of piezoelectric hybrid composites were verified against experimental results. Brockman (2009) outlined the theory needed for analytical solution. Ray and Mallik (2004) presented some development of finite element that can be used to analyze macroscale hybrid fiber composites. Their work is readily comparable to analytical solutions, but their setups cannot directly adaptable into commercially available finite element software.

In this chapter, a FE software ANSYS®, with support for coupled-field analysis, will be utilized to validate several experimental problems outlined earlier. Support for coupled-field analysis is useful for problems incorporating piezoelectrical materials. ANSYS® provides a plethora of tools for piezoelectric materials that can be numerically as analyzed for structural, harmonic, electrical and transient behaviors.

4.2 Setup, Method and Element Description

Finite element modeling of piezoelectric materials requires coupled field to account for the coupling between the structural and electrical field. The theory behind this coupling was introduced in section 1.6. For ANSYS® it is necessary to consider the difference in how the software treats the piezoelectric coefficients matrix and the elastic coefficients matrix compared to the most used standard format in this field; the IEEE standard (Board 1988). The elastic coefficients matrix could either be given in the form

of stiffness or compliance. Defining the rest of the materials properties follows the methods typically found in the relevant literature.

$$d_{IEEE}^{T} = \begin{bmatrix} d_{11} & d_{12} & d_{13} \\ d_{21} & d_{22} & d_{23} \\ d_{31} & d_{32} & d_{33} \\ d_{41} & d_{42} & d_{43} \\ d_{51} & d_{52} & d_{53} \\ d_{61} & d_{62} & d_{63} \end{bmatrix} \qquad d_{ANSYS}^{T} = \begin{bmatrix} d_{11} & d_{12} & d_{13} \\ d_{21} & d_{22} & d_{23} \\ d_{31} & d_{32} & d_{33} \\ d_{61} & d_{62} & d_{63} \\ d_{51} & d_{52} & d_{53} \\ d_{41} & d_{42} & d_{43} \end{bmatrix} \qquad (4\text{-}1)$$

$$C^{E}{}_{IEEE} = \begin{bmatrix} C_{11} & C_{12} & C_{13} & C_{14} & C_{15} & C_{16} \\ C_{21} & C_{22} & C_{23} & C_{24} & C_{25} & C_{26} \\ C_{31} & C_{23} & C_{33} & C_{34} & C_{34} & C_{36} \\ C_{41} & C_{42} & C_{43} & C_{44} & C_{45} & C_{46} \\ C_{51} & C_{52} & C_{53} & C_{54} & C_{55} & C_{56} \\ C_{61} & C_{62} & C_{63} & C_{64} & C_{65} & C_{66} \end{bmatrix} C^{E}{}_{ANSYS} = \begin{bmatrix} C_{11} & C_{12} & C_{13} & C_{14} & C_{15} & C_{16} \\ C_{21} & C_{22} & C_{23} & C_{24} & C_{25} & C_{26} \\ C_{31} & C_{23} & C_{33} & C_{34} & C_{34} & C_{36} \\ C_{61} & C_{62} & C_{63} & C_{64} & C_{65} & C_{66} \\ C_{51} & C_{52} & C_{53} & C_{54} & C_{55} & C_{56} \\ C_{41} & C_{42} & C_{43} & C_{44} & C_{45} & C_{46} \end{bmatrix} \qquad (4\text{-}2)$$

ANSYS® has two methods of coupled-field analysis available; namely direct coupling and sequential coupling (ANSYS Inc., 2005). The methods are different in that direct coupling includes all coupled and non-coupled degrees of freedom into one single matrix system, whereas the sequential coupling performs separate analysis for each physical field and then couples them by transferring the result from one field to another until convergence is achieved.

The latter method is useful when dealing with a wide variety of coupled fields at once, such as weakly coupled fields and non-linearity since it conserves processing power and memory. However, when dealing with a strong coupling such as piezoelectricity, direct coupling is advantageous (Bayik, 2016).

Therefore, the direct method will be adopted in this study. By utilizing the 3D, 20-node coupled field SOLID226 elements found in ANSYS® this can be achieved.
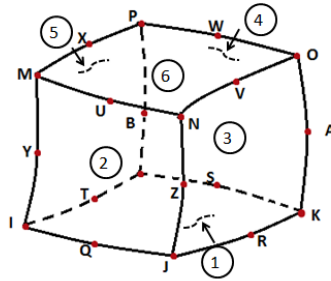
Figure 4-1. Geometry of SOLID226 element, reproduced from ANSYS element References (ANSYS Inc., 2005)

Four degrees of freedom (DOF) are applied for each node in *Figure 4-1* (red dots) which include translation in x, y and z directions in addition to voltage. The solutions include force and electrically charged values and element support static, modal, full harmonic, and full transient analyses.

The set of equations for direct coupling field elements is shown in equation (4-3).

$$\begin{bmatrix} [M] & 0 \\ 0 & 0 \end{bmatrix}\begin{Bmatrix} \{\ddot{u}\} \\ \{\ddot{V}\} \end{Bmatrix} + \begin{bmatrix} [C^u] & 0 \\ 0 & [C^v] \end{bmatrix}\begin{Bmatrix} \{\dot{u}\} \\ \{\dot{V}\} \end{Bmatrix} + \begin{bmatrix} [K^u] & [K^Z] \\ [K^Z]^T & [K^V] \end{bmatrix}\begin{Bmatrix} \{u\} \\ \{V\} \end{Bmatrix} = \begin{Bmatrix} \{F\} \\ \{L\} \end{Bmatrix} \quad (4\text{-}3)$$

Where M denotes mass matrix, C^u the damping matrix, and K^u the stiffness matrix. The dielectric terms are symbolized by permittivity matrix C^v, electrical potential vector V, electric charge vector L, and strong coupling by K^Z.

ANSYS reference manuals describe several examples of piezoelectric element analysis and utilizes the harmonic analysis tools with some postprocessing by APDL-commands to achieve FRF of the analyzed data (a coding example can be found in Appendix A). A harmonic analysis allows the user to run a problem through a wide spectrum of frequencies with different mechanical and electrical load cases.

Most of the inputs to the analysis will be calculated by the program based on material input and load situation, but α mass matrix multiplier and β stiffness matrix multiplier must be given manually. α and β are dimensionless uncoupled parameters

related to the excitation frequency of the system (as damping is frequency dependent) and can be found by applying the Rayleigh damping matrix approximation. α and β are related to the damping matrix as shown in equation (4-4), they are used in damped modal, transient and harmonic analyses.

$$[C] = \alpha[M] + (\beta + \beta_c)[K] + \sum_{j=1}^{NMAT} \beta_j[K_j] + \sum_{j=1}^{NEL}[C_k] + [C_\zeta] \qquad (4\text{-}4)$$

In equation (4-4), β_c denotes the variable stiffness matrix which allows users to set an alternative damping parameter for given frequencies, NMAT, number of materials with a fixed damping input and β_j which are these materials (K_j) respective fixed damping ratios. Furthermore, NEL is related to number of elements with specified damping and C_k is the element damping matrix while C_ζ is a frequency dependent damping matrix input by the user. For the analysis presented in this chapter only α, β and a fixed non-frequency dependent damping ratio -found from logarithmic descent-were used due to the complexity of establishing the other frequency dependent damping inputs as they require rigorous experimental testing on the device to be accurate.

Cai, Zheng, Khan and Hung have published an overview of how the different damping relates to analysis in ANSYS$^\circledR$ and provided a more comprehensive background. lieu of α and β, a constant structural damping coefficient, ζ, can be given which works reasonably better with simple systems, as will be shown later.

To utilize the coupled-piezoelectric tools in ANSYS, a circuit with elements CIRCU94 must be set up where the energy harvesting circuit can be represented by a resistive load directly attached to the piezoelectric FE-model. SOLID185 elements were used to model the composite layers, leaving the user with control of both layer thickness and fiber orientation, which afterward can be meshed according to the user input.

For contact elements between piezoelectrical elements and composites, the target element TARGE170 and the contact element CONTA174 were chosen as they support the harmonic analysis performed here. Johnson has written a comprehensive overview of contact elements (Johnson). His settings for a bonded contact were exploited in this analysis.

4.3 Modeling of the Benchmark Problem

Due to the limited literature dealing with experimental validation of either analytical or numerical models of piezo-based energy harvester, a necessity of creating a benchmark problem for later analysis arose. First, fundamental properties for the beam had to be established, including damping parameters. Some of the properties were taken from the literature, while the rest were found directly or imperatively from in-house experiments.

Table 4-1

Properties for the Carbon Fiber Composite

Properties	Unit
Dimensions: L×W×T	186mm×18mm×0.3mm
Young modulus, E_1 and E_2	45.01 GPa
Young modulus, E_3	20 GPa
Shear modulus, G_{xy}	2.9 GPa
Poisson ratio, v	0.35
Density	1100 kg/m^3

Table 4-2

Properties for the PZT Patch, Navy II, ref. (APC International, Ltd, 2019)

Properties	Unit
Diameter x thickness	186x18x0.3mm
Young modulus, E_1 and E_2	63 GPa
Young modulus, E_3	54 GPa
Poisson ratio, v	0.31
Density	7600 kg/m^3
Dielectric dissipation factor	2.00
Relative dielectric permittivity, ε	1900 F/m
d_{13} and d_{23}	-21.5281 C/m
d_{33}	-5.2386 C/m
d_{62} and d_{51}	-34.22 C/m
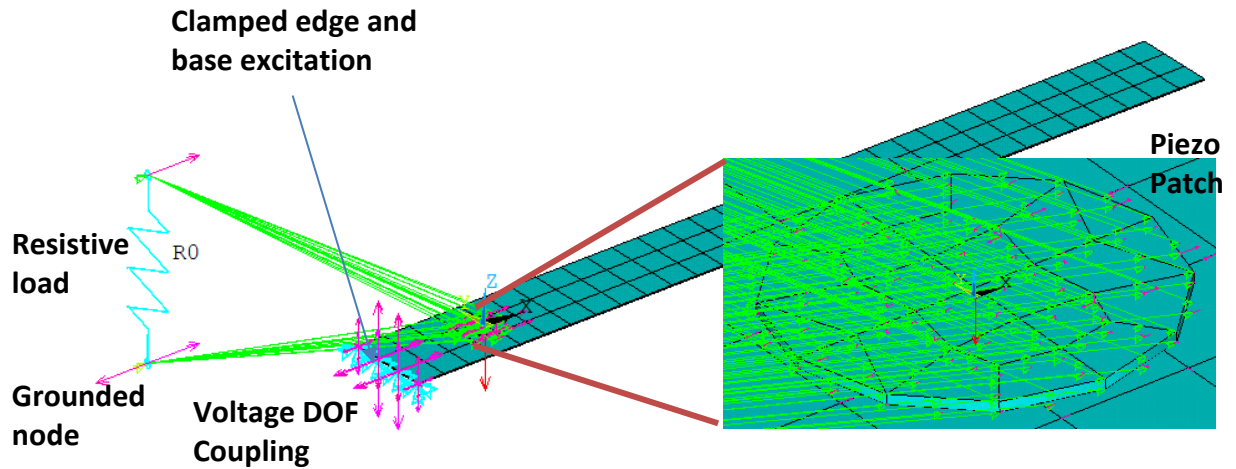
Figure 4-2. Finite element model of PZT patch glued to the carbon fiber composite beam. The final model would have a higher element division than portraited here.

The model was set up as shown in

Figure 4-2, where voltage DOF connect the piezo patch to a circuit. Grounding of

a node on the circuit is essential for the following relative calculation of obtained voltage.

To define the damping of the system, several experiments were run, taking the

logarithmic descent of exiting the beam tip by hand (i.e. free vibrations), and recording

the deflection with a laser was shown to be sufficient for the frequency ratio looked at

here. The damping was found to be ζ=0.0134.

4.3.1 Results and Experimental Validation

To assure that the model is detailed enough, a convergence study is necessary to

verify that the element sizing is subtle enough for giving stable results with small to no

deviation when the sizing of the elements is adjusted slightly. Such a study is presented in

Figure 4-3 and shows both convergences of first frequency and achieved $V/m/s^2$ at the 1st

frequency.
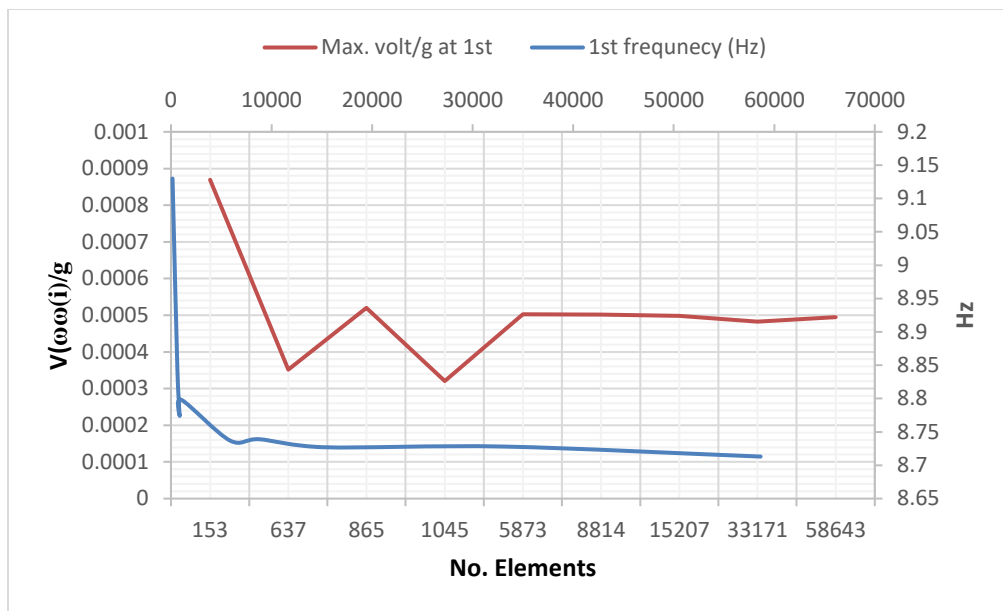
Figure 4-3. Convergence study of the benchmark problem.

The convergence study shows that for more than 5800 elements the solution is reasonably stable and alters insignificantly by applying a finer mesh. Taking the results from section 3.3.5 for a composite 2-layered beam with a patch and plotting it again together with the results from the harmonic analysis (
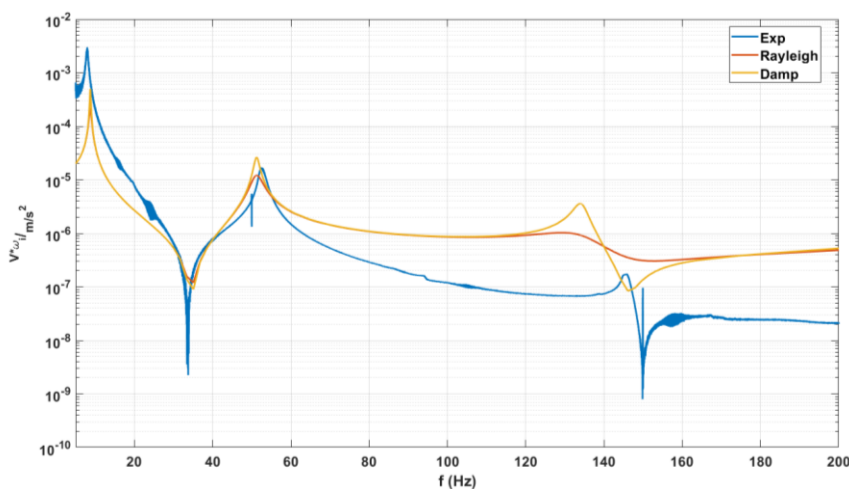
Figure *4-4*), it became evident that the behavior of the device can be foreseen.

However, additional work is required to build a more realistic model of the energy harvester experiment. The data from the numerical solution had to be divided by its

respective frequency to match the FRF-results. A flat base acceleration of 2g was applied in the numerical solution.
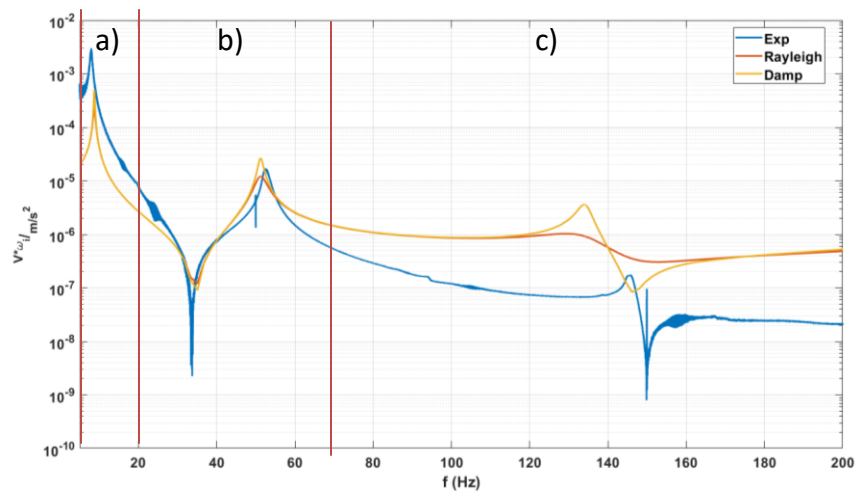
Figure 4-4. Comparison of experimental and numerical solution for a CF-beam with a patch.

As can be seen, the numerical solution matches reasonably well with the experimental results trend and somewhat in same order of magnitude for a specific part of the frequency bandwidth investigated here; part (b) in Figure 4-4. At low frequencies, part (a), the beam is likely to experience transient load cases due to the fluctuation of the beam and to the narrow bandwidth that 1st resonance frequency experiences. It is likely to assume some non-linearity, as the deflection at this point is significant. All these factors could have contributed to the significant offset seen at low frequencies.

However, most energy scavenging devices are not utilized at such low frequencies, and it is, therefore, encouraging to see the results match better in part (b) when not considering the drop seen around 35 Hz. This drop is likely due to the patch reaching a lower threshold where the weak current flow is not strong enough to force itself through the minimum flow barrier of the patch; referred to as the Schottky barrier, which the current FE-analysis does not account for. The 2nd natural frequency of the

device matches reasonably well and shows some correlation in the result.

For high frequencies, part (c), there are probably many factors that contributed to the overall offset. These include electromechanical losses, offset coupling factors, circuit power consumption together with material parameters inaccuracy (for example the manufacturer reports properties variation of ± 20 % for d_{33}). Other factors could be dielectric loss and corona discharge for the PZT-patch.

The error sources above are mostly frequency independent and could be addressed by correctly testing the patch before bonding to the device. In addition, other factors such as impedance fluctuations, unmatching of mechanical impedance, damping factors and device reflection are frequency-dependent and are difficult to model due to their high degree of non-linearity and substantial differences from one device to another.

Another likely source of deficiency for the analysis stems from the experimental setup. While this setup utilized an electrodynamic shaker applying a base acceleration to make the FE-setup easier, an opposite approach could be tried. Other researchers usually utilize a shaker attached to a point on the device, whereas the device itself is clamped to a rigid surface. Acceleration, velocity or force are measured at the shaker point of attachment, and would therefore not only read input, but would determine the resonance frequency of the device, bringing increased confidence to the output. Taking the resonance readings solely from the piezo output highlights a significant frequency shift, especially at higher frequencies, as evident in part (c). This is likely due to phase shifting between a sinusoidal mechanical vibration load and a sinusoidal voltage load in the circuit.

Similar attempts, in which a point load is utilized on a patch-based beam or plate

demonstrated overall better agreement. (Bayik, 2016); (Aridogan, Basdogan & Erturk, 2014); (Erturk & Inman, 2009); (Xu & Kim, 2016). Finally, it should be noted that a fixed damping ratio seems to be more accurate than utilizing Rayleigh damping in ANSYS, especially at higher frequencies.

4.4 Modeling of Different Stepped Hybrid Composite Devices

Due to the handmade nature of the hybrid devices, the material properties had to be supplied by a wide variety of sources. This introduced some degree of error, as the properties were documented on other substrates and environments utilized here. See Table 4-3. Additionally, to this the first step had a length to width of 119 x 32 mm, glass layer 151 x 31 mm and step two 154 x 31 mm. The respective layers had an offset from the clamped edge at 15 mm for glass, and 85 mm for CF on step 02. The piezoelectric layers were assumed to cover the full surface of each respective step.

Table 4-3

Properties of the ZnO NWs Stepped Device

	t, (mm)	E_1 and E_2(GPa)	E_3(GPa)	G_{xy}(GPa)	v	ρ, (kg/m^3)	d_{33} pm/V	ε_{11}, ε_{22}	ε_{33}
CF	0.12	45.01	20	2.9	0.35	1100			
Glass	0.12	22.99	5	2.26	0.3	1500			
ZnO NWs	5 µm	see eq. (4-5)	see eq. (4-5)	see eq. (4-5)	see eq. (4-5)	1160	14.3 a)	979.2 b)	1271.7 b)

Note. a) (Zhao, Wang & Mao, 2004), b) (Kobiakov, 1980)

$$C^E_{ANSYS_{ZnONW}} = \begin{bmatrix} 207 & 117.7 & 106.1 & 0 & 0 & 0 \\ 117.7 & 207 & 106.1 & 0 & 0 & 0 \\ 106.1 & 106.1 & 209.5 & 0 & 0 & 0 \\ 0 & 0 & 0 & 0 & 0 & 44.6 \\ 0 & 0 & 0 & 0 & 44.8 & 0 \\ 0 & 0 & 0 & 44.6 & 0 & 0 \end{bmatrix} GPa \qquad (4\text{-}5)$$

Equation (4-5) shows the orthotropic stiffness matrix for a ZnO crystal, as

presented by Morkoç and Özgur (2009) study on properties of ZnO crystals. The

thickness of the ZnO NWs represents the lowest possible applied thickness that could be

applied to the problem due to element scaling limitations. Scaling up the device would

not change this problem, as ANSYS® has limitations on how small certain elements can

be relative to others. Therefore, a thickness of 5 μm had to be utilized, which is 3.5 times

more than the thickness observed in the SEMs for the best growth results.
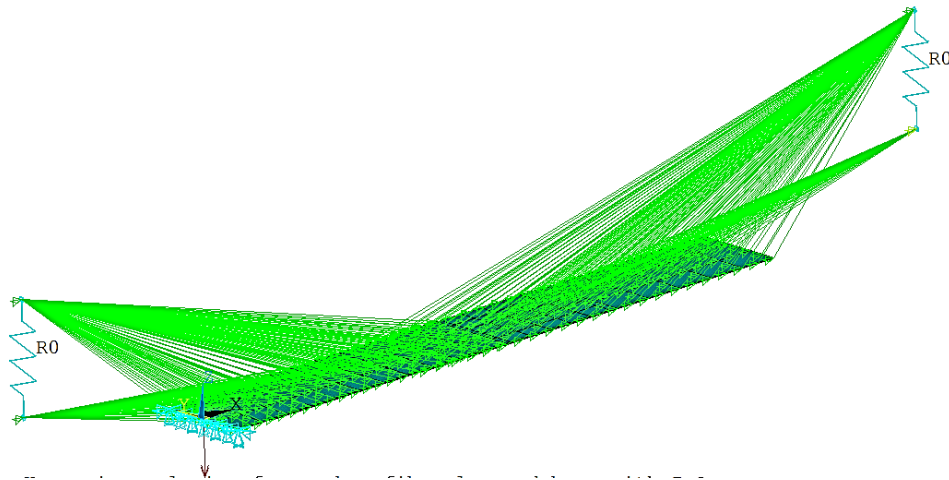
Figure 4-5. Finite element model for the stepped energy harvester based on ZnO NWs, witch enlargement on the piezoelectrical layers. See Figure 4-2 for element type and descriptions.

Fixed damping of ζ= 0.0114 was used, as obtained through logarithmic descent of

a free vibration test with a laser vibrometer and a clamped ZnO NWs device. Results are

presented together with the combined device in Figure 4-7. A resistance load of 1 Ω was

set to symbolize an open-circuit load case as seen for the experimental stepped device

setup.

Figure 4-6 show a closeup of how the layers were modelled in the region where

all layers are present at the midsection of the device.
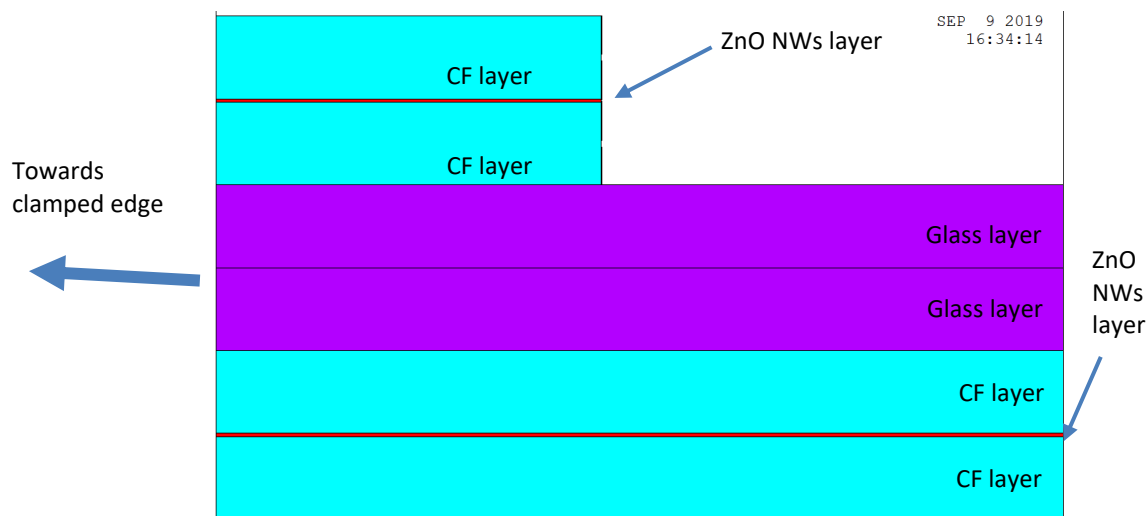
Figure 4-6. Layer wise make up of modelled stepped device with ZnO NWs layers.

4.4.1 ZnO NWs and PZT Hybrid Device

The device was modeled in the same manner as the previous device but would have a thin layer of PZT on top of the ZnO NWs layer as the only difference. Here again, even though a thickness of only 200 nm of PZT was sputtered on the tested devices, the analysis tool could not exploit a lower thickness than 5 μm. The minimum thickness was employed again, and from a vibro laser meter a damping ratio of ζ= 0.0143 was determined. Other properties were as given in Table 4-3. Table 4-4 conveys the properties of the PZT thin film taken from relevant literature. Noteworthy is that these properties are taken from ideal test specimens, tested in ideal conditions and with different thicknesses than studied here. The literature shows that the sputtered PZT thin film has piezoelectrical properties close to the commercially available patches.

Table 4-4

The Mechanical and Piezoelectric Properties of a PZT-thin Film

Properties	Unit
Thickness	5 μm
Young modulus, E	100 GPa[a]
Poisson ratio, ν	0.31[b]
Density	7600 kg/m^3 [b]
Relative dielectric permittivity, ε	850 F/m[c]
d_{33}	$^{2.08}$ /m^2 [d]

Note. a) (Delobelle, Fribourg-Blanc & Rèmiens, 2006) b) (APC International, Ltd, 2019) c) (Frunza, et al., 2011) d) (Tsuchiya, Toshiaki Kitagawa & Nakamachi, 2003)

       For mechanical properties of PZT films, Delobelle, Fribourg-Blanc and Rèmiens,

(2006), have conducted comprehensive studies on as-sputtered, after-treatment, and

measurements techniques for determining the strength of a PZT thin film and reported a

Young's modulus of 90 to 110 GPa for a low contact pressure on an 850 nm thick film.

Furthermore, due to the scarcity of PZT-thin films mechanical properties in available

literature, an isotropic material behavior will be assumed, even though PZT is reported to

behave more like an orthotropic material.

4.5 Results and Discussion on Stepped Device Numerical Solutions

Applying 2g of base acceleration to both experiments, Figure 4-7 shows the numerical solutions for both setups.
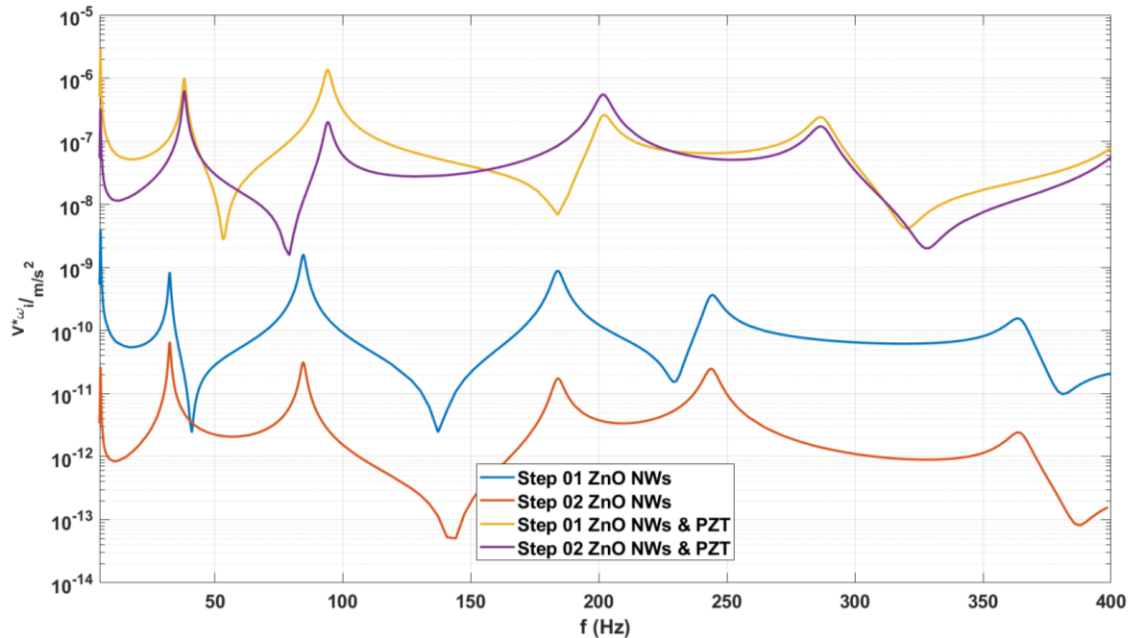
Figure 4-7. FEM analysis of FRP stepped devices with ZnO NWs and ZnO NWs/PZT.

In agreement with cited literature and previous experimental data, A significant increase in the voltage for the hybrid ZnO NWs/PZT thin film device in comparison to a device based only on ZnO NWs. Step 01 is seen to achieve an overall higher voltage than the second step for both devices. This makes sense as 1st step is closer the clamped edge and is therefore under more strain than the 2nd step.

From the plot, an improvement for the 1st frequency from 5.33 Hz, $0.00392 \frac{\mu V \omega_i}{m/s^2}$ to 5.35 Hz and $2.86 \frac{\mu V \omega_i}{m/s^2}$ can be observed. The increase in the 1st natural frequency is likely due to the thickness increase, while the 728.6 % increase in voltage agrees to some extent with experimental results from other researchers. No et al. (2013) showed an improvement from 0.5 nA to 270 nA for their combined device of PZT and ZnO over a

flat ITO-substrate. Nonetheless, the results do not correlate well with the experimental results presented in section 3.3.5, where a 47.63 % difference was reported. In addition, the trend of increased piezoelectrical effects at higher frequencies cannot be observed.

Both the numerical analysis and the No et al. specimens utilized a thicker layer of PZT, namely 5 μm for the numerical model and 2 μm for No et al., compared to 200 nm for the experimental device. The layers of piezoelectric numerical model were also modeled patch wise and did not enclose the ZnO NWs as seen both in No et al. (2013) research and via the SEM micrographs in this research. It is believed that enclosing the ZnO NWs could bring additional synergy effects.

Considering the piezoelectrical losses discussed earlier, in addition to the lower permittivity in thin-film sputtered PZT due to material imperfections, the reduced gain in the numerical analysis compared to other published investigations on other ideal surfaces, as well as the great discrepancies in data from these results compared to the experimental, indicates that further tweaking of FE model is required to make these approaches practical to demonstrate the mechanical and dynamical performances of hybrid FRPs more accurately. Some tweaking techniques were mentioned for the benchmarking device in section 4.3.1 which could be applicable for the analysis here too.

The test results could not be compared directly to the FE simulation as the shaker input was highly frequency dependent, and was measured in velocity, which is not applicable in ANSYS. As seen in Figure 3-25, where the best performing stepped devices were compared, Figure 4-7 does not display similar results neither in magnitude nor in the overall shape. The discrepancy in magnitude is due to the difference in obtained data readings, though the shape should have matched if the numerical analysis took account of

a realistic modelling of the stepped devices. This could not be observed and are likely due to limitation in the software to model hybrid composites accurately.

The implementation of the piezoelectric coupling was successfully employed on fibrous composites as shown by Hagood and Bent (1993), see Figure 4-8, Martinez, Artemev, Nitzsche and Geddes (2006) see Figure 4-9 and the FEM-model for dynamic characterization that Zheng, Duan and Zhou (2019). have developed could be an influential starting point.
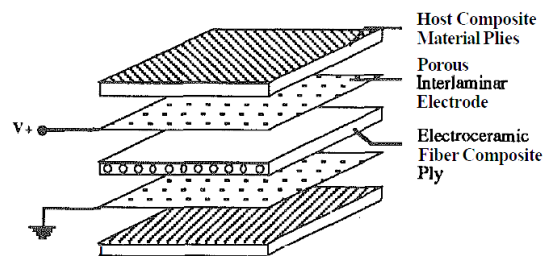
Figure 4-8. Schematic of the model of Hagood and Bent (1993) for analytical solution of active hybrid composites
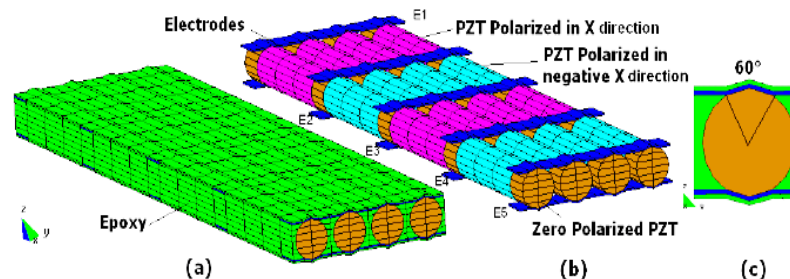
Figure 4-9. Finite element model of piezoelectrically actuated fiber composites. (Martinez, Artemev, Nitzsche & Geddes, 2006).

As seen in Figure 4-8 and Figure 4-9, these research seems promising for integration into an overall FEM solver, but they lack verification with experimental tests. While a full active fiber composites implementation option might not be available in any

available commercial FE-software currently, several promising studies can be conducted

with FE-analysis on a fiber-scale. Some representative studies include the work on the

multi-inclusion model done by Malakooti, Zhou and Sodano (2016), or representative

volume element (RVE) to see how the fiber form affects the general piezoelectric

characteristics of the hybrid composites (Kar-Gupta & Venkatesh, 2007) or RVE

utilization to evaluate the piezoelectrical and dielectric properties for composite

structures (Mishra, Krishna, Singh & Das, 2017).

4.6 Conclusions

In this chapter, utilizing FE-tools for potentially demonstrating the performance

of piezoelectric fiber composites for energy harvesting over different frequencies bands

and load cases was investigated. Even though the ANSYS® tool package shows great

promise in correctly predicting the behavior of isotropic beams and plates with

piezoelectrical patches, the analysis here shows that discrepancies arise when anisotropic

materials are utilized as the host material. The FE-analysis reveals both tendencies and

somewhat the same magnitudes as an experimental benchmark problem, but due to a

wide variety of unaccounted for factors, it does not accurately predict the behavior of the

device at all frequencies.

Exploiting the same FE-tool for a stepped device revealed that a significant

voltage gain of 728.6 % was possible by adding a thin layer of PZT on top of the ZnO

NWs. Due to limitations in the FE-software, neither the experimental thickness of PZT,

ZnO NWs nor the fibers could be accurately modelled, and the outcome should,

therefore, be interpreted qualitatively rather than an accurate result.

In summary, the commercially available software ANSYS® has significant

deficiencies when modeling hybrid FRPs. However, the work presented is not as fruitless as it might appear, because it demonstrates potentially viable next steps for more extensive research into numerical modeling of these types of hybrid fibrous composites.

5. CONCLUSIONS, RECOMMENDATIONS AND FUTURE WORK

5.1 Conclusions

This thesis has undertaken a comprehensive experimental and numerical analysis of hybrid fiber composites comprising one or more piezoelectric nanophases, ZnO NWs and PZT thin films. Numerous previous investigations have shown that there are significant advantages in growing ZnO NWs over carbon fibers. Although most of these studies rely on time-consuming processes that sometimes adversely affect the fibers themselves, this thesis has revealed that the production time, cost and harmful aqueous exposure could be significantly reduced for the hybrid FRPs by utilizing a microwave heating source.

While the new production process had no negative impact on the mechanical or dynamical performance of the ZnO NWs FRPs compared to other relevant literature, the addition of a 200 nm PZT thin film was shown to strengthen the apparent elastic modulus of the material by 25.8 % compared to plain-fiber FRPs, and an increase by 12.8 % compared to composites with ZnO NWs. The PZT thin film is likely acting as a stiffening support for the ZnO NWs, drastically improving the interfacing stiffness between CF-layers in a FRP.

The incorporation of ZnO NWs was shown to drastically improve the tan δ up to 168. 4% compared to plain FRP. The same trend could somewhat be seen for the combined hybrid, but at far less enhancement; an increment of 10.3 % for tan δ .This damping enhancement are largely attributed to frictional slippage being improved by the ZnO NWs as the addition of PZT was seen to worsen the damping characteristics and barely performing better than a plain FRP.

Although the addition ZnO NWs was seen to drastically reduce the storage modulus, a unique attribute of the ZnO NWs/PZT thin films hybrid, the inclusion of a PZT thin film was seen to restore and surpass the plain FRP in terms of storage modulus by 9.65 % according to DMA tests. Taking this into account, along with a power gain of 733.94 % compared to pure ZnO NWs devices, from 0.02101nW to 1.7523nW. The new hybrid composites have achieved synergy in energy harvesting performance which could open the possibility of utilizing the hybrid material in real-life applications.

Finally, a commercial FE-tool ANSYS® was utilized to determine the performance of potential revolutionary hybrid composites. While the model relatively accurately predicts the behavior of a benchmark problem, the same trends could not be obtained for the hybrid devices. A voltage gain of the 728.6 % for a combined hybrid FRP compared to pure ZnO NWs devices agrees to some extent with experimental results from other researchers on ideal substrates, however, could not be reproduced on the less optimal surface of CFs. The discrepancies are attributed to limitations both in the software as well as modeling of the fibrous composite that replenish the lab environment, indicating that further investigation is needed to successfully implement hybrid composites into an FE environment. Section 4.5 discuss several of these potential improvements.

5.2 Recommendations and Future Work

Several recommendations can be inferred from the thesis as time constraints, insufficient instrumentation, and knowledge deficiency did set some limitations on what could be achieved in the timeframe of a master thesis. Therefore, some recommendations are presented here:

- More work on the combination with different thicknesses of PZT could lead to a more optimized device

- Finding production methods that gain a lower weight fiber fraction would potentially lead to materials less prone to defects and result in better experimental readings.

- Working on RVE finite elements models together with available commercial FE-software would likely be more attractive in order to probe the difference in adding/setting up different types of piezoelectrical materials together with the respective fiber and epoxy matrix of interest. This could later be implemented in a layer wise numerical model utilizing elements such as the SOLID226-elements given in ANSYS®.

- Further care and work on isolating the devices electrodes and circuiting would likely improve some of the devices studied here drastically, as a low impedance was measured on several devices likely due to internal short-circuiting. Adding a layer of non-conductive glass fiber on the top and bottom of each hybrid FRPs layer would likely eradicate this problem, but at the cost of weaker interlaminar bonding.

6. REFERENCES

A.Pothan, L., Oommen, Z., & Thomas, S. (2003). Dynamic mechanical analysis of banana fiber reinforced polyester composites. *Composites Science and Technology, 63*(2), 283-293.

A.Song, S., Kwang Lee, C., Bang, Y. H., & Kim, S. S. (2016). A novel coating method using zinc oxide nanorods to improve the interfacial shear strength between carbon fiber and a thermoplastic matrix. *Composites Science and Technology, 134*(6), 106-114.

acoustics.co.uk. (n.d.). Retrieved 06 09, 2019, from https://www.acoustics.co.uk/pal/wp-content/uploads/2015/11/Properties-of-poled-PVDF.pdf

Adegoke, K. A., Iqbal, M., Louis, H., Jan, S. U., Mateen, A., & Bello, O. S. (2018). Photocatalytic Conversion of CO2 Using ZnO Semiconductor by Hydrothermal Method. *Pak. J. Anal. Environ. Chem. Vol. 19*, 1-27.

Advanced Electro Ceramics. (2019, 09 17). (CeramTec) Retrieved 06 16, 2019, from CeramTec.com: https://www.ceramtec.com/ceramic-materials/soft-pzt/

Aksel, E., & Jones, J. L. (2010). Advances in Lead-Free Piezoelectric Materials for Sensors and Acutators. *Sensors, 10*(3), 1935-1954.

ANSYS, Inc. (2005, 08). ANSYS Coupled-Field Analysis Guide. *ANSYS Release 10.0*. ANSYS, Inc. and ANSYS Europe.

APC International, Ltd. (2019, 08 22). *Physical and Piezoelectric properties of APC materials*. Retrieved from American Piezo: https://www.americanpiezo.com/apc-materials/physical-piezoelectric-properties.html

Aridogan, U., Basdogan, I., & Erturk, A. (2014). Analytical modeling and experimental validation of a structurally integrated piezoelectric energy harvester on a thin plate. *Smart Materials and Structures, 23*(4), 1-13.

Ayyagari, S., Al-Haik, M., & Rollin, V. (2018). Mechanical and Electrical Characterization of Carbon Fiber/Bucky Paper/Zinc Oxide Hybrid Composites. *Journal of Carbon Research, 4*(6), 1-18.

Baruah, S., & Dutta, J. (2009). Hydrothermal growth of ZnO nanostructures. *Science and Technology of Advanced Materials, 10*(1), 1-20.

BaTi03 Specifications. (2019, 09 17). Retrieved 06 17, 2019, from AmericanPiezo: https://www.americanpiezo.com/single-crystals-non-pzt-materials/bati03-specifications.html

Bayik, B. (2016). *Finite Element Modelling of a Piezo Patch Energy Harvester and Equivalent Circuit Modelling on a Thin Plate with AC-DC Conversion, MS Thesis.* Istanbul, Turkey: Koc University.

Bent, A. A., Hagood, N. W., & Rodgers, J. P. (1995). Anisotropic actuation with piezoelectric fiber composites. *Journal of Intelligent Material Systems and Structures, 6*(3), 338-349.

Berger, H., Kari, S., UlrichGabbert, Rodriguez-Ramos, R., Guinovart, R., A.Otero, J., & Bravo-Castillero, J. (2005). An analytical and numerical approach for calculating effective material coefficients of piezoelectric fiber composites. *International Journal of Solids and Structures, 42*(21-22), 5692-5714.

Boroujeni, A. Y., Al-Haik, M., Emami, A., & Kalhor, R. (2017). Hybrid ZnO Nanorod Grafted Carbon Fiber Reinforced Polymer Composites; Randomly versus Radially Aligned Long ZnO Nanorods Growth. *Journal of Nanoscience and Nanotechnology, 18*(6), 4182-4188.

Bowland, C., Zhou, Z., & Sodano, H. A. (2014). Multifunctional Barium Titanate Coated Carbon Fibers. *Advanced Functional Materials, 24*(40), 6303-6308.

Brockmann, T. H. (2009). *Theory of Adaptive Fiber Composites.* Donauworth, Germany: Springer.

Butler, J. L., & Sherman, C. H. (2006). *Transducer and arrays for underwater sound.* Cohasset, Massachuttes, US: Springer.

Cai, C., Zheng, H., Khan, M. S., & Hung, K. C. (n.d.). *Modeling of Material Damping Properties in ANSYS.* Singapore: Defense Systems Division, Institute of High Performance Computing.

Chan, K. H., & Hagood, N. W. (May 6, 1994). Modelling of nonlinear piezoceramics of structural actuation. *Proc. SPIE, Smart Structures and Materials 1994: Smart Structures and Intelligent Systems. 2190.* Orlando: SPIE.

Chang, Y., Yin, B., Qiu, Y., Zhang, H., Lei, J., Zhao, Y., Luo, Y., Hu, L. (2016). ZnO nanorods array/BaTiO3 coating layer composite structure nanogenerator. *Journal of Materials Science: Materials in Electronics, 27*(4), 3773-3777.

Dagdeviren, C., Joe, P., Tuzman, O. L., Park, K.-I., Lee, K. J., Shi, Y., Huang, Y., Rogers, J. A. (2016). Recent progress in flexible and stretchable piezoelectric devices for mechanical energy harvesting, sensing and actuation. *Extreme Mechanics Letter Part 1, 9*(1), 269-281.

Dauksevicius, R., O'Reilly, E., & Seifikar, M. (2015). Multiphysics Model of Encapsulated Piezoelectric-semiconducting Nanowire with Schottky Contacts and External Capacitive Circuit. *Procedia Engineering, 120*, 896-901.

Delobelle, P., Fribourg-Blanc, E., & Rèmiens, D. (2006). Mechanical properties determined by nanoindentation tests of [Pb(Zr,Ti)O3] and [Pb(Mg1/3Nb2/3)1−xTixO3] sputtered thin films. *Thin Solid Films 515*, 1385-1393.

Detwiler, D., Shen, M.-H., & Venkayya, V. (1995). Finite element analysis of laminated composite structures containing distributed piezoelectric actuators and sensors. *Finite Elements in Analysis and Design 20*, 87-100.

Dong, S., & Gauvin, R. (1993). Application of dynamic mechanical analysis for the study of the interfacial region in carbon fiber/epoxy composite materials. *Polymer Composites, 14*(5), 414-420.

Dutra, R. L., Soares, B. G., Campos, E. A., & Silva, J. L. (2000). Hybrid composites based on polypropylene and carbon fiber and epoxy matrix. *Polymer, 41*(10), 3841-3849.

Eovino, B. T. (May, 2015). *Design and Analysis of a PVDF Acoustic Transducer Towards an Imager for Mobile Underwater Sensor Networks, Report.* Berkley: University of California.

Erturk, A., & Inman, D. J. (2009). An experimentally validated bimorph cantilever model for piezoelectric energy harvesting from base excitations. *Smart Materials and Structures, 18*(2), 1-18.

Feih, S., & Mouritz, A. (2012). Tensile properties of carbon fibres and carbon fibre–polymer composites in fire. *Composites Part A Applied Science and Manufacturing, 43*(5), 765-772.

Frunza, R., Ricinschib, D., Gheorghiud, F., Apetreid, R., Lucad, D., Mitoseriud, L., & Okuyamab, M. (2011). Preparation and characterisation of PZT films by RF-magnetron sputtering. *Journal of Alloys and Compounds, 509*(21), 6242-6246.

Fujisawa, H., Iwamoto, Y., Nakashima, S., & Shimizu, M. (November, 2012). Fabrication of PZT/ZnO Core-Shell Nanowires by Metalorganic Chemical Vapor Deposition. *2012 Fifth International Conference on Emerging Trends in Engineering and Technology.* Himeji, Japan: IEEE.

Gao, J., Xue, D., Liu, W., Zhou, C., & Ren, X. (2017). Recent Progress on BaTiO3-Based Piezoelectric Ceramics for Actuator Applications. *Actuators, 6*(24), 1-20.

Gao, P. X., Song, J., & Jin Liu, Z. L. (2006, 12 12). Nanowire Piezoelectric Nanogenerators on Plastic Substrates as Flexible Power Sources for Nanodevices. *Advanced Materials, 19*(1), pp. 1-6.

Ghandi, K., & Hagood, N. W. (May, 1996). Nonlinear Finite Element Modeling of Phase Transitions in electro-mechanically coupled material. *In Proc of SPIE conference on Smart Structures and Materials: Mathematics and Control in Smart Structures. 2715*, pp. 121-140. San Diego: SPIE.

Glazounov, A. E., Zhang, Q., & Kim, C. (1998). A new torsional actuater based on shear piezoelectric response. *Proceedings of SPIE - The International Society for Optical Engineering. 3324*, pp. 82-91. San Diego: SPIE.

Goertzen, W., & Kessler, M. (2007). Dynamic mechanical analysis of carbon/epoxy composites for structural pipeline repair. *Composites Part B: engineering 38*, 1-9.

Guillon, O., Thiebaud, F., & Perreux, D. (2002). Tensile Fracture of Soft and Hard PZT. *International Journal of Fracture, 117*(3), 235-246.

Gullapalli, H., Vemuru, V. S., Kumar, A., Botello-Mendez, A., Vajtai, R., Terrones, M., . . . Ajayan, P. M. (2010). Flexible Piezoelectric ZnO–Paper Nanocomposite Strain Sensor. *Nano Micro Small, 6*(15), 1641-1646.

Haccart, T., Cattan, E., & Remiens, D. (2002). Dielectric, ferroelectric and piezoelectric properties of sputtered PZT thin films on Si substrates: influence of film thickness and orientation. *Semiconductor Physics, Quantum Electronics & Optoelectronics, 5*(1), 78-88.

Hagood, N., & Bent, A. (April 19-22, 1993). AIAA Development of Piezoelectric Fiber Composites for Structural Actuation. *34th Structures, Structural Dynamics and Materials Conference* (pp. 3625-3638). La Jolla, US: AIAA.

Hassan Elahi, A. P. (2014). Experimental Determination of Mechanical Quality Factor of Lead Zirconate Titanate (PZT- 5A4E) by Equivalent Circuit Method under various Thermal and Resistance Conditions. *Technical Journal, 19*(2), 1-4.

Hook, J. R., & Hall, H. E. (2010). *Solid State Physics 2nd edition.* Manchester, UK: Manchester Physics Series.

(1988). *IEEE Standard on Piezoelectricity.* New York: The insitute of Electrical and Electronic Engineers,INC.

Jackson, J. D. (1962). *Classical Electrodynamics.* New York: John Wiley and Sons INC.

Jin, L. (2011). *Broadband Dielectric Response in Hard and Soft PZT: Understanding Softening and Hardening Mechanisms, PHD Dissertation.* Lausanne, Switzerland: Ecole Polytechnique Federale de Lausanne.

Johnson, D. H. (n.d.). *Principles of Simulating Contact Between Parts using ANSYS, Report.* Erie, Pennsylvania: Penn State-Erie.

Kang, M.-G., Jung, W.-S., Kang, C.-Y., & Yoon, S.-J. (2016). Recent Progress on PZT Based Piezoelectric Energy Harvesting Technologies. *Actuators, 5*(5), 1-17.

Kao, M.-C., Chen, H. Z., Young, S.-L., Lin, C.-C., & Kung, C.-Y. (2012). Structure and photovoltaic properties of ZnO nanowire for dye-sensitized solar cells. *Nanoscale Research Letters, 7*(1), 240.

Karagulle, H., Malgaca, L., & Oktem, H. F. (2004). Analysis of active vibration control in smart structures by ANSYS. *Smart Mater. Struct. 13*, 661-667.

Kar-Gupta, R., & Venkatesh, T. A. (2007). Electromechanical response of 1–3 piezoelectric composites: a numerical model to assess the effects of fiber distribution. *Acta Materialia, 55*(4), 1275-1292.

Kawai, H. (1969). The piezoelectricity of Poly(vinylidene Fluoride). *Japanese Journal of Applied Physics, 8*(7), 975-976.

Ken-ichi Kakimoto, K. F. (2013). Fabrication of fibrous BaTiO3-reinforced PVDF composite sheet for transducer application . *Sensors and Acturators A: Physical, 200*(1), 21-25.

Kermani, M. R., Moallem, M., & Patel, R. V. (2008). *Applied Vibration Suppresion Using Piezoelectric Materials.* New York, US: Nova Science Publisher.

Khalatkar, A., Gupta, V. K., & Agrawal, A. (2014). Analytical, FEA, and Experimental Comparisons of Piezoelectric Energy Harvesting Using Engine Vibrations. *Smart Materials Research, 2014*(741280), 1-8.

Kholkin, A., Pertsev, N., & Goltsev, A. (2008). Piezoelectricity and Crystal Symmetry. In A. Safari, & E. K. Akdogan, *Piezoelectric and Acoustic Materials for Transducer Applications* (pp. 17-39). Boston, US: Springer.

Kim, S. J., & Kwak, M. K. (2004). The nonlinear behaviour of a piezoelectric wafer: constitutive equations and simulations. *Institute of Physics: Smart Materials and Structures, 13*(1), 184-190.

Klingshirn, C. F., Meyer, B. K., Waag, A., Hoffmann, A., & Geurts, J. (2010). *Zinc Oxide - from fundemental properties towards novel applications.* Karlsruhe, Germany: Springer-Verlag Berlin Heiderlberg.

Kobiakov, I. B. (1980). Elastic, Piezoelectric and Dielectric Properties of ZnO and CDS Single Crystals in a Wide Range of Temperatures. *Solid State Communications, 35*(3), 305-310.

Küpfer, J., & Finkelmann, H. (1991). Nematic liquid single crystal elastomers. *Die Makromolekulare Chemie, Rapid Communications, 12*(12), 717-726.

Lead Zirconate Titanate (PZT-5A). (1999). Retrieved 09 06, 2019, from efunda.com: https://www.efunda.com/materials/piezo/material_data/matdata_output.cfm?Material_ID=PZT-5A

Lee, H. J., Zhang, S., Bar-Cohen, Y., & Sherrit, S. (2014). High Temperature, High Power Piezoelectric Composite Transducers. *Sensors, 14*(8), 14526-14552.

Lee, M., Chen, C.-Y., Wang, S., Cha, S. N., Park, Y. J., Kim, J. M., Chou, M. K., Wang, Z. L. (2012). A Hybrid Piezoelectric Structure for Wearable Nanogenerators. *Advanced Materials, 24*(13), 1759-1764.

Liao, Q., Zhang, Z., Zhang, X., Mohr, M., Zhang, Y., & Fecht, H.-J. (2014). Flexible piezoelectric nanogenerators based on fiber/ZnO nanowires/ paper hybrid structure for energy harvesting. *Nano Research, 7*(6), 917-928.

Lin Hai-Bo, C. M.-S.-W.-L.-C. (2008). Enhanced mechanical behaviour of lead zirconate titanate piezoelectric composites incorporating zinc oxide nanowhiskers. *Chinese Physics B, 17*(2008), 4323-4327.

Lin, Y., & A. Sodano, H. (2008). Concept and model of a piezoelectric structural fiber for multifunctional composites. *Composites Science and Technology 68 (7-8)*, 1911-1918.

Lin, Y., & Sodano, H. A. (2009). Electromechanical characterization of a active structural fiber lamina for multifunctional composites. *Composites Science and Technology, 69*(11-12), 1825-1830.

Lin, Y., & Sodano, H. A. (2009). Fabrication and Electromechanical Characterization of a Piezoelectric Structural Fiber for Multifunctional Composites. *Advanced Functional Materials, 19*(4), 592-598.

Lin, Y., Ehlert, G., & Sodano, H. A. (2009). Increased Interface Strength in Carbon Fiber Composites through a ZnO Nanowire Interphase. *Advanced Functional Materials, 19*(16), 2654-2660.

Lippmann, M. (2009). On the principle of the conservation of electricity. *The London, Edinburgh, and Dublin Philosophical Magazine and Journal of Science, 11*(70), 474-475.

Liu, D., Zhou, B., Yoon, S. H., Kim, S.-B., Ahn, H., Prorok, B. C., Kim, S.-H., Kim, D.-J. (2011). Determination of the true Young's modulus of Pb(Zr0.52Ti0.48)O3 films by by Nanoindentation: Effects of Film Orientation and Substrate. *Journal of the American Ceramic Society, 94*(11), 3698-3701.

Liu, H., Zhong, J., Lee, C., Lee, S.-W., & Lin, L. (2018). A comprehensive review on piezoelectric energy harvesting technology: Materials, mechanisms, and applications. *Applied Physics Reviews, 5*(4), 1-29.

Liu, L., Hong, K., Ge, X., Liu, D., & Xu, M. (2014). Controllable and Rapid Synthesis of Long ZnO Nanowire Arrays for Dye-Sensitized Solar Cells. *The journal of Physical chemistry, 118*(29), 15551-15555.

Malakooti, M. H., & Sodano, H. A. (2013). Multi-Inclusion modeling of multiphase piezoelectric composites. *Composites Part: B, 47*, 181-189.

Malakooti, M. H., Zhou, Z., & Sodano, H. A. (March 20-24, 2016). Energy harvesting from vertically aligned PZT nanowire arrays. *Proceedings 9799, Active and Passive Smart Structures and Integrated Systems.* Las Vegas, US: SPIE.

Marshall., J. M., Mergen, S., Zhang, Q., Whatmore., R., Chima-Okereke, C., Roberts, W. L., . . . Reece, M. J. (2011). The electromechanical properties of highly [100] oriented [Pb(Zr0.52Ti0.48)O-3, PZT] thin films. *Integrated Ferroelectrics, 80*(1), 77-85.

Martinez, M., Artemev, A., Nitzsche, F., & Geddes, B. (2006). Finite element modeling of actuated fibre composites. *High Performance Structures and Materials III, 85*, 103-110.

Masghouni, N. (2014). *Hybrid Carbon Fiber/ZnO Nanowires Polymeric Composite for Structural and Energy Harvesting Applications, PhD Dissertation.* Blacksburg, US: Virginia Polytechnic Institute and State University.

Masghouni, N., & Al-Haik, M. (November 15-21, 2013). Vibration Damping Enhancement of Fiber Reinforced Polymer Composites With Surface Grown Zinc Oxide Nanorods. *ASME 2013 International Mechanical Engineering Congress and Exposition.* San Diego, US: ASME.

Masghouni, N., Bourton, J., Philen, M. K., & Al-Haik, M. (2015). Investigating the energy harvesting capabilities of a hybrid ZnO nanowires/carbon fiber polymer composite beam. *Nanotechnology, 26*(9), 1-8.

Mishra, N., Krishna, B., Singh, R., & Das, K. (2017). Evaluation of effective elastic, piezoelectric, and dielectric properties of SU8/ZnO nanocomposite for vertically integrated nano generators using finite element method. *Journal of Nanomaterials, 2017*(1924651), 1-14.

Morkoç, H., & Özgür, Ü. (2009). General Properties of ZnO. In H. Morkoç, & Ü. Özg€ur, *Zinc Oxide: Fundamentals, Materials and Device Technology* (pp. 1-71). Weinheim: WILEY-VCH Verlag GmbH & Co.

Mortada, O., Blondy, P., Orlianges, J.-C., Chatras, M., & Crunteanu, A. (May, 2015, 2). Quality Factor Optimization of Composite Piezoelectric Single-Crystal Silicon MEMS Resonators. *IEEE MTT-S International Microwave Symposium* (pp. 1-3). Phoenix, AZ, USA: IEEE.

Narayanana, S., & Balamurugan, V. (2003). Finite element modelling of piezolaminated smart structures for active vibration control with distributed sensors. *Journal of Sound and Vibration 262*, 529-562.

No, I.-J., Jeong, D.-Y., Lee, S., Kim, S.-H., Cho, J.-W., & Shin, P.-K. (2013). Enhanced charge generation of the ZnO nanowires/PZT hetero-junction based nanogenerator. *Microelectronic Engineering, 110*, 282-287.

Oliveira Araujo, L. A., Rollo, J. M., Foschini, C. R., & Fortulan, C. A. (2017). Study of Abrasive Cutting of Natural Quartz for Manufacturing Piezoelectric Power Generators. *Material Science Forum, 912*, 234-239.

Özgür, Ü., Alivov, Y. I., Liu, C., Teke, A., Reshchikov, M. A., Doğan, S., . . . Morkoç, H. (2005). A comprehensive review of ZnO materials and devices. *Journal of Applied Physics, 98*(4), 1-95.

Ozgur, U., Hofstetter, D., & Morkoc, H. (2010). ZnO Devices and Applications: A Review of Current Status and Future Prospects. *Proceedings of the IEEE, 98*(7), 1255-1268.

Paknejad, A., Rahimi, G., & Salmani, H. (2018). Analytical solution and numerical validation of piezoelectric energy harvester patch for various thin multilayer composite plates. *Arch Appl Mech, 88*(7), 1139–1161.

Pan, C., Li, Z., Guo, W., Zhu, J., & Wang, Z. L. (2011). Fiber-Based Hybrid Nanogenerators for/as Self-Powered Systems in Biological Liquid. *Angewandte Chemie, 50*(47), 11192-11196.

Petrović, M. M., Bobić, J., & Stojanović, B. D. (2008). History and Challenges of Barium Titanate: Part II. *Science of Sintering, 40*(3), 235-244.

Piezo Data: PZT-5H. (2019, 09 17). Retrieved from efunda.com: https://www.efunda.com/materials/piezo/material_data/matdata_output.cfm?Material_ID=PZT-5H

Piezo Data: Quartz. (2019, 09 17). Retrieved from efunda.com: https://www.efunda.com/materials/piezo/material_data/matdata_output.cfm?Material_ID=Quartz

Priya, S., Song, H.-C., Zhou, Y., Varghese, R., Chopra, A., Kim, S.-G., Kanno, I., Wu, L., Ha, S. H., Ryu J., Polcawich, R. G. (2017). A Review on Piezoelectric Energy Harvesting: Materials, methods and circuits. *Energy Harvesting and Systems, 1*(1), 1-38.

Qin, Y., Wang, X., & Wang, Z. L. (2008). Microfibre–Nanowire Hybrid Structure for Energy Scavenging. *Nature, 451, 451*(14), 809-814.

Ray, M. C., & Mallik, N. (2004). Finite element analysis of smart structuee containing piezoelectric fiber-reinforce composite actuators. *AIAA Journal, 42*(7), 1398-1405.

Saito, Y., Takao, H., Tani, T., Nonoyama, T., Takatori, K., Homma, T., Nagaya, T., Nakamura, M. (2004). Lead-free piezoceramics. *Nature, 432*(7013), 84-87.

Skandani, A. A., Masghouni, N., Case, S. W., Leo, D. J., & Al-Haik, M. (2012). Enhanced vibration damping of carbon fibers-ZnO nanorods hybrid composites. *Applied Physics Letters 101*, 1-4.

Sodano, H., Lloyd, J., & Inman, D. (2006). An experimental comparison between several active composite actuators for power generation. *Smart Materials and Structures, 15*(5), 1211-1216.

Song, J., Zhao, G., & Wang, B. L. (2017). Design optimization of PVDF-based piezoelectric energy harvesters. *Heliyon, 3*(9), 137-143.

Song, S. A., Lee, C. K., Bang, Y. H., & Kim, S. S. (2016). A novel coating method using zinc oxide nanorods to improve the interfacial shear strength between carbon fiber and a thermoplastic matrix. *Composites Science and Technology, 134*(6), 106-114.

Suvrajyoti Mishra, L. U. (2019). Advances in Piezoelectric Polymer Composites for Energy Harvesting Applications: A Systematic Review. *Materials and Engineering, 304*, 1-25.

Thomas, J. P., Keennon, M. T., DuPasquier, A., Qidwai, M. A., & Matic, P. (November 15-21, 2003). Multifunctional Structure-Battery Materials for Enhanced Performance in Small Unmanned Air Vehicles. *Proceedings of the ASME international mechanical engineering congress and R&D exposition* (pp. 289-292). Washington DC, US: ASME.

Tiwari, V., & Srivastava, G. (2015). Structural, dielectric and piezoelectric properties of 0–3 PZT/PVDF composites. *Ceramics International, 41*(6), 8008-8013.

Topolov, V. Y., Bisegna, P., & Bowen, C. R. (2018). *Piezo-Active Composites* (Vol. 271). Cham, Switzerland: Springer Series in Material Science.

Tsuchiya, K., Toshiaki Kitagawa, & Nakamachi, E. (2003). Development of RF magnetron sputtering method to fabricate PZT thin film actuator. *Precision Engineering 27*, 258-264.

TurkoV, B., V., K., Rudyk, P., & Rudyk, Y. V. (2016). Thermal Conductivity of Zinc Oxide Micro- and Nanocomposites. *Journal of Nano- and Electronic Physics, 8*(4), 02004-1-4.

Uchino, K. (2010). The Development of Piezoelectric Materials and the New Perspective. In *Advanced Piezoelectric Mater* (pp. 1-85). Pennsylvenia, US: Woodhead Publishing Limited.

Unalan, H. E., Hiralal, P., Rupesinghe, N., Dalal, S., Milne, W. I., & Amaratunga, G. A. (2008). Rapid Synthesis of Aligned Zinc Oxide Nanowires. *Nanotechnology 19*, 1-6.

Voigt, W. (1910). *Lehrbuch der Kristallphysik.* Leipzig & Berlin, Germany: Druck und Verlag Von B.G Teubner.

Wang, J., Neaton, J. B., Zheng, H. M., Valanoor, N., Ogale, S. B., Liu, B., . . . Ramesh, R. (2003). Epitaxial BiFeO3 Mutiferroic Thin Film Heterostructures. *Science, 299*(5613), 1719-1722.

Wang, R.-M., Zheng, S.-R., & Zheng, Y. (2011). *Polymer Matrix Composites and Technology 1st edition.* Bejing, China: Woodhead Publishing.

Wang, Z. (2008). Towards Self-Powered Nanosystems: From Nanogenerators to Nanopiezotronics. *Advanced Functional Materials, 18*(22), 3553-3567.

Wang, Z. L. (2004). Zinc oxide nanostructures: growth, properties and applications. *Journal of Physics: Condensed Matter , 16*(25), 829-858.

Wei, H., Wang, H., Xia, Y., Cui, D., Shi, Y., Dong, M., Liu, C., Ding, T., Zhang, J., Ma, Y., Wang, N., Wang, Z., Sun, Y., Wei, R., Guo, Z. (2018). An overview of lead-free piezoelectric materials and devices. *Journal of Materials Chemistry C, 7*(46), 12433-12760.

White, S. R., Sottos, N. R., Geubelle, P., Moore, J. S., Kessler, M. R., Sriram, S., Brown, E. N., Viswanathan, S. (2001). Autonomic healing of polymer composites. *Nature, 409*(6822), 794-797.

Wikimedia Commons . (2015, 02 09). Retrieved from Sphalerite unit cell depth fade 3D-balls : https://commons.wikimedia.org/w/index.php?title=File:Sphalerite-unit-cell-depth-fade-3D-balls.png&oldid=149521174

Xia, W., & Zhang, Z. (2018). PVDF-based dielectric polymers and their applications in electronic materials. *IET Nanodielectrics, 1*(1), 17-31.

Xiangqin Meng, C. Y. (2012). Preparation and electrical properties of ZnO/PZT films by radio frequency reactive magnetron sputtering. *Materials Letters, 83*, 179-182.

Xu, R., & Kim, S.-G. (2016). Modeling and Experimental Validation of Bi-Stable Beam Based Piezoelectric Energy Harvester. *Energy Harvesting and Systems, 3*(4), 313-321.

Xu, S., Adiga, N., Ba, S., Dasgupta, T., Wu, C. F., & Wang, Z. L. (2009). Optimizing and Improving the Growth Quality of ZnO Nanowire arrays guided by staticstical Design of Experiments. *ACSNano, 3*(7), 1803-1812.

Xu, S., Yeh, Y.-w., Poirier, G., McAlpine, M. C., Register, R. A., & Yao, N. (2013). Flexible Piezoelectric PMN−PT Nanowire-Based Nanocomposite and Device. *Nano Letters, 13*(6), 2393-2398.

Yang, Y., & Tang, L. (2009). Equivalent Circuit Modeling of Piezoelectric Energy Harvesters. *Journal of Intelligent Material Systems and Structures, 20*(18), 2223-2235.

Zhang, L., Bai, S., Su, C., Zheng, Y., Qin, Y., Xu, C., & Wang, Z. L. (2015). A High-Reliability Kevlar Fiber-ZnO Nanowires Hybrid Nanogenerator and its Application on Self-Powered UV Detection. *Advanced Functional Materials, 25*(36), 5794-5798.

Zhang, Q. Q., Djuth, F. T., Zhou, Q. F., Hu, C. H., Cha, J. H., & Shung, K. K. (2006). High frequency broadband PZT thick film ultrasonic transducers for medical imaging applications. *Ultrasonics, 44*(Supplement), 711-715.

Zhao, M.-H., Wang, Z.-L., & Mao, S. (2004). Piezoelectric characterization of individual zinc oxide nanobelt probed by piezoresponse force microscope. *Nano Letters, 4*(4), 587-590.

Zheng, J., Duan, Z., & Zhou, L. (2019). A Coupling Electromechanical Cell-Based Smoothed Finite Element Method Based on Micromechanics for Dynamic Characteristics of Piezoelectric Composite Materials. *Advances in Materials Science and Engineering, 4*, 1-16.

Zhong-xia DUAN, G.-q. Y.-b.-w.-y. (2011). Preparation and characterization of PZT thick film enhanced by ZnO nanowhiskers for MEMS piezoelectric generators. *Progress in Natural Science: Materials International, 21*(2), 159-163.

Zhou, Z., Tang, H., & Sodano, H. A. (2013). Vertically Aligned Arrays of BaTiO3 Nanowires. *ACS Applied Materials & Interfaces, 5*(22), 11894-11899.

Zhu, M., Worthington, E., & Njuguna, J. (2009). Analysis of power output of piezoelectric energy harvesting devices directly connected to a load resistor using a coupled piezoelectric curcuit finite element method. *IEEE Transactions on Ultrasonics, Ferroelectrics, and Frequency Control, 56*(7), 1309-1318.

A. Appendix: ANSYS Mechanical APDL commands

```
/CLEAR
/PREP7
/UIS,MSGPOP,3

/title, Harmonic analysis of a carbon-fibre layered beam with a PZT-patch
!----------------------------------------------------------!
!Element Types                               !
!----------------------------------------------------------!
!Composite layer element type
ET,1,SOLID185,,,1 !Remember to give same thickness in secdata as in the given volume
!Piezoelectric Element
ET,2,solid226,1001
!Contact elements:
ET,3,CONTA174
!Target elements:
ET,4,TARGE170
!Resistor Element
ET,5,CIRCU94,0

! ELement division:
!attribute for volume (Warning, picked lines cant be one same height)!
*set,plmesh,40  ! mesh for plate=number of segments
*set,pzmesh,8  ! mesh for pzt=number of  segments
*set,meshthc,1           !thickness of pzt mesh (do a mesh refined seperately)
tc=0.000120 ! layer thickness
BeamW = 0.0144
BeamL = 0.175


!----------------------------------------------------------!
!Material Properties                        !
!----------------------------------------------------------!
!Composite Beam Material Properties
MP,DENS,1,1100              ! From measurment of acutal beam
MP,EX,1,45.01e9             !Elastic modulus, x-direction
MP,EY,1,45.01e9             !Elastic modulus, y-direction
MP,EZ,1,20e9               !Elastic modulus, z-direction
MP,PRXY,1,0.35              !Major poisson's ratio, x-y plane
MP,PRYZ,1,0.2              !Major poisson's ratio, y-z plane
MP,PRXZ,1,0.35              !Major poisson's ratio, x-z plane
MP,GXY,1,2.892e9            !Shear modulus, x-y plane
MP,GYZ,1,2e9              !Shear modulus, y-z plane
MP,GXZ,1,2e9              !Shear modulus, x-z plane

!! Piezo material properties for PZT II
MP,DENS,2,7600
MP,EX,2,63e9
MP,PRXY,2,0.31 !Approx for all ceramics, ref. https://bostonpiezooptics.com/ceramic-materials-pzt

!Dielectric dissipation Factor: (2.00)
MP,LSST,2,2.00

! See material properties and lirarature overview to see where this is from
MP,PERx,2,1900
MP,PERy,2,1900
MP,PERZ,2,1900

TB,PIEZ,2,,,0   !TBOPT:1 Piezoelectric strain matrix [d] (converted to [e] form before use)
TBMODIF,1,1,
TBMODIF,1,2,
TBMODIF,1,3,-21.5281                        !e13
TBMODIF,2,1,
TBMODIF,2,2,
TBMODIF,2,3,-21.5281                        !e23
TBMODIF,3,1,
TBMODIF,3,2,
TBMODIF,3,3,-5.2386                         !e33
```

```
TBMODIF,4,1,
TBMODIF,4,2,
TBMODIF,4,3,
TBMODIF,5,1,-34.2200                                  !e51
TBMODIF,5,2,
TBMODIF,5,3,
TBMODIF,6,1,
TBMODIF,6,2,-34.2200                                  !e42 (from IEEE format)
TBMODIF,6,3,


!----------------------------------------------------------!
!Geometry Dimensions                           !
!----------------------------------------------------------!
!Composite layer 1
materid=1  !material id
ang=0                 !angel of layer in degrees
SECTYPE,1,shell,,layer1                !define which element type
SECDATA,tc,materid,ang                           !define thikncess and angle

!Piezo layer 1
PiezoH = 0.00028
Rpiezo=0.005

!Piezo and Expoy Offset from the clamped end (need to move beam to neg.side due to later symmetry command)
OffsetX = 0.0
Negoffset=0.023


!----------------------------------------------------------!
!Reserved Nodes for Circuit                     !
!----------------------------------------------------------!
!circuit dimension
cirdim = 0.02
n,1,-4*cirdim,0,3*cirdim
n,2,-4*cirdim,0,cirdim


!----------------------------------------------------------!
!FEM Domain Geometries                        !
!----------------------------------------------------------!
!Create Beam, Epoxy and Piezoelement
! CF layer 1
BLOCK,-Negoffset,(BeamL-Negoffset),-BeamW/2.0,BeamW/2.0,0,-tc,
! CF layer 2
BLOCK,-Negoffset,(BeamL-Negoffset),-BeamW/2.0,BeamW/2.0,(-tc),(-tc-tc),
! Piezopatch (rectengular)
!BLOCK,OffsetX,(OffsetX+PiezoL),-PiezoW/2.0,PiezoW/2.0,(tc+tc),(tc+tc+PiezoH),

!Circular patch:
CYL4,OffsetX,0,0,0,Rpiezo,90,PiezoH


!----------------------------------------------------------!
!Mesh                              !
!----------------------------------------------------------!
! Corner line meshing:
LSEL,S,LINE,,9,12,1              !SELECT CORNER LINES OF composite LAYER 1
LSEL,A,LINE,,21,24,1            !SELECT CORNER LINES OF composite LAYER 2
LESIZE,ALL,,,1                  !# OF ELEMENT DIVISION

!Composite layer 1 meshing
LSEL,S,LINE,,1,3,2              !SELECT SHORT LINES OF beam
LSEL,A,LINE,,6,8,2             !SELECT SHORT LINES OF beam
LESIZE,ALL,,,plmesh            !# OF ELEMENT DIVISION

LSEL,S,LINE,,2,4,2              !SELECT LONG LINES OF beam
LSEL,A,LINE,,5,7,2             !SELECT LONG LINES OF beam
LESIZE,ALL,,,(plmesh*(BeamL/BeamW))  !# OF ELEMENT DIVISION

!Composite layer 2 meshing
LSEL,S,LINE,,18,20,2            !SELECT SHORT LINES OF beam
LSEL,A,LINE,,13,15,2           !SELECT SHORT LINES OF beam
LESIZE,ALL,,,plmesh            !# OF ELEMENT DIVISION
```

```
LSEL,S,LINE,,17,19,2                    !SELECT LONG LINES OF beam
LSEL,A,LINE,,14,16,2                    !SELECT LONG LINES OF beam
LESIZE,ALL,,,(plmesh*(BeamL/BeamW))  !# OF ELEMENT DIVISION

!!PZT MESHING
LSEL,s,line,,31,33,1
LESIZE,all,,,meshthc
LSEL,all

LSEL,s,line,,27,28,1
LESIZE,all,,,pzmesh

LSEL,all

LSEL,s,line,,25,26,1
LESIZE,all,,,pzmesh

LSEL,s,line,,29,30,1
LESIZE,all,,,pzmesh

LSEL,all

VSEL,S,VOLU,,1                          !SELECT layer 1
VATT,1,,1                               !ASSIGN ELEMENT ATTRIBUTES

VSEL,S,VOLU,,2                          !layer 2
VATT,1,,1                               !ASSIGN ELEMENT ATTRIBUTES

VSEL,S,VOLU,,3                          !SELECT PIEZO PATCH  1
VATT,2,,2                               !ASSIGN ELEMENT ATTRIBUTES

VSEL,S,VOLU,,1,2,1
VMESH,1,2,1

VSEL,S,VOLU,,3,
VSWEEP,3
VSYMM,x,3
VSYMM,y,3,4,1
VGLUE,3,4,5,6
NUMMRG,NODE
NUMMRG,KP

*get,Epz,elem,,count              ! Get all the number of solid elements

!----------------------------------------------------------!
!Merge Nodes On the Interfaces of carbon fiber composites (this can probably be rewritten into layered structure) !
!----------------------------------------------------------!
nsel,s,loc,x,Negoffset,(BeamL-Negoffset)
nsel,r,loc,y,-BeamW/2.0,BeamW/2.0
nsel,r,loc,z,tc
NUMMRG,node,,,,HIGH
alls

!Define Target surface and elements for bonding of PZT to Composite beam:
!------------------------------------------------------------------------
! Define bonded contact, (from Principles of Simulating Contact Between Parts using ANSYS)
KEYOPT,3,2,1
KEYOPT,3,6,0
KEYOPT,3,7,0
KEYOPT,3,8,2
KEYOPT,3,9,1
KEYOPT,3,11,0
KEYOPT,3,12,5                          ! Keyopt 12 set to 5 is a bonded always condition

!Target surface:
ASEL,S,AREA,,13                        ! Select area at the bottom electrode of the patch
ASEL,A,AREA,,18
ASEL,A,AREA,,23
ASEL,A,AREA,,28
TYPE,4                                 ! Selectn element type
```

```
real,3                                    ! Sets the element real constant set attribute pointer
NSLA,S,1                       ! Select those nodes associated with the selected areas
ESLN,S,0                       ! Select those elements attached to the selected nodes
ESURF,ALL                                   ! Generate elements overlaid on the free faces of selected nodes
!Contact surface
ASEL,S,AREA,,2
type,3
real,3
NSLA,S,1
ESLN,S,0
ESURF,ALL

!End of contact pair creation and re-oriantation, check:
http://www.xansys.org/forum/viewtopic.php?p=45383&sid=7276be9ea93de4bc15375cd73c6ddbad


!--------------------------------------------------------!
!Voltage Coupling: Setup Electrodes on Piezo          !
!--------------------------------------------------------!
ASEL,S,AREA,,13                   ! Select area at the bottom electrode of the patch
ASEL,A,AREA,,18
ASEL,A,AREA,,23
ASEL,A,AREA,,28                   ! Voltage coupling for bottom electrode (-) PZT 1
NSLA,S,1
*get,n_bot,node,0,num,min
cp,n_bot,volt,all
alls

ASEL,S,AREA,,14                   ! Select area at the top electrode of the patch
ASEL,A,AREA,,19
ASEL,A,AREA,,24
ASEL,A,AREA,,29                   ! Voltage coupling for top electrode (-) PZT 1
NSLA,S,1
*get,n_top,node,0,num,min
cp,n_top,volt,all
ALLSELL,ALL,ALL


!--------------------------------------------------------!
!--------------------------------------------------------!
!---------   Open-Circuit Modal Analysis    --------------!
!--------------------------------------------------------!
!--------------------------------------------------------!
/SOLU
antyp,modal
nmodes = 6
MODOPT,LANB,nmodes,0,1000
MXPAND,nmodes     !Specifies the number of modes to expand and write for a modal or buckling analysis.

!--------------------------------------------------------!
!Load & Boundary Conditions                       !
!--------------------------------------------------------!
!Structural BCs
nsel,s,loc,x,-Negoffset
d,all,ux,0
d,all,uy,0
d,all,uz,0
alls
!Open-circuit configuration
d,n_bot,volt,0

solve
finish

*dim,NF_OC,array,1,nmodes

*do,i,1,nmodes
*get,NF_OC(1,i),mode,i,freq
*enddo

*do,i,1,nmodes
*CFOPEN,'open-circuit-resonance-frequencies', 'txt'
```

```
*VWRITE,i,NF_OC(1,i)
(f4.0,'   ', f8.3)
*enddo
*CFCLOS
!---------------------------------------------------------!
!---------------------------------------------------------!
!---------   Short-Circuit Modal Analysis    -------------!
!---------------------------------------------------------!
!---------------------------------------------------------!
/SOLU
!---------------------------------------------------------!
!Load & Boundary Conditions                       !
!---------------------------------------------------------!
!Short-circuit configuration
d,n_top,volt,0

solve
finish

*dim,NF_SC,array,1,nmodes

*do,i,1,nmodes
*get,NF_SC(1,i),mode,i,freq
*enddo

*CFOPEN,'short-circuit-resonance-frequencies', 'txt'
*do,i,1,nmodes
*VWRITE,i,NF_SC(1,i)
(f4.0,'   ', f8.3)
*enddo
*CFCLOS
!---------------------------------------------------------!
!---------------------------------------------------------!
!---------   Harmonic Analysis with resistor   -------------!
!---------------------------------------------------------!
!---------------------------------------------------------!
/PREP7
ddele,n_top,volt
ddele,n_bot,volt
CPDELE,n_bot,n_top,,ANY
alls

!Create resistor & connect directly to piezo electrodes
!Default resistor parameter
*SET, Resistance, 2e3
r,5, Resistance
type,5  $  real, 5
e,2,1

ASEL,S,AREA,,13              ! Select area at the bottom electrode of the patch
ASEL,A,AREA,,18
ASEL,A,AREA,,23
ASEL,A,AREA,,28              ! Voltage coupling for bottom electrode (-) PZT 1
NSLA,S,1
nsel,a,node,,2
CP,2,VOLT,all
alls

ASEL,S,AREA,,14              ! Select area at the top electrode of the patch
ASEL,A,AREA,,19
ASEL,A,AREA,,24
ASEL,A,AREA,,29              ! Voltage coupling for top electrode (-) PZT 1
NSLA,S,1
nsel,a,node,,1
CP,1,VOLT,all
alls

nsel,s,loc,x,0.0
nsel,r,loc,y,0.0
nsel,r,loc,z,(tc+tc+PiezoH)
```

```
*get,topc_pt,node,0,num,min
alls

nsel,s,loc,x,(BeamL-Negoffset)
nsel,r,loc,y,0.0
nsel,r,loc,z,(tc+tc)
*get,free_end_pt,node,0,num,min
alls
!--------------------------------------------------------!
!Load & Boundary Conditions                     !
!--------------------------------------------------------!
!Bot Electrode BC
d,2,volt,0
!Base Vibration Acceleration/Force
accelx=0.0
accely=0.0
accelz=-2
ACEL,accelx,accely,accelz

/SOLU
antyp,harm                      !starts harmonic analysis,
ALPHAD,2.928,
BETAD,0.0001528
!DMPRAT,0.0134
alls

NF_previous=0
NF_next=0
!--------------------------------------------------------!
!Load Steps
!--------------------------------------------------------!
substep_sparse_zone=15
substep_cluster_zone=30

*do,i,1,nmodes
*IF, i, EQ, nmodes, THEN
NF_next=NF_SC(1,nmodes)*1.4
*ELSE
NF_next=NF_SC(1,i+1)
*ENDIF

! harfrq defines frequency range in a harmonic analysis
harfrq,(NF_previous+(NF_SC(1,i)-NF_previous)*0.3),(NF_previous+(NF_SC(1,i)-NF_previous)*0.9)
nsubst,substep_sparse_zone      !defines the number of substeos to be taken in this load step
KBC,1                                           !specifies ramped or stepped loading withing a load step
HROPT,FULL                                      !spacifies harmonic analysis options, full method
HROUT,OFF                                       !Specifies the harmonic analysis output options, off=print complex displacements as
amplitude and phase angle
LUMPM,0                                         !Specifies a lumped mass matrix formulation, 0=off use the element dependent default
mass matrix formulation
OUTPR,ALL,ALL,                                  !Controls the solution printout. All means all.
LSWRITE,(i-1)*5+1,              !write load and load step option data to a file

harfrq,(NF_previous+(NF_SC(1,i)-NF_previous)*0.9),(NF_previous+(NF_SC(1,i)-NF_previous)*0.992)
nsubst,substep_sparse_zone
KBC,1
HROPT,FULL
HROUT,OFF
LUMPM,0
OUTPR,ALL,ALL,
LSWRITE,(i-1)*5+2,

harfrq,(NF_previous+(NF_SC(1,i)-NF_previous)*0.992), (NF_OC(1,i)+(NF_next-NF_OC(1,i))*0.002)
nsubst,substep_cluster_zone
KBC,1
HROPT,FULL
HROUT,OFF
LUMPM,0
OUTPR,ALL,ALL,
LSWRITE,(i-1)*5+3,
```

```
harfrq,(NF_OC(1,i)+(NF_next-NF_OC(1,i))*0.002), (NF_OC(1,i)+(NF_next-NF_OC(1,i))*0.025)
nsubst,substep_sparse_zone
KBC,1
HROPT,FULL
HROUT,OFF
LUMPM,0
OUTPR,ALL,ALL,
LSWRITE,(i-1)*5+4,

harfrq,(NF_OC(1,i)+(NF_next-NF_OC(1,i))*0.025), (NF_OC(1,i)+(NF_next-NF_OC(1,i))*0.25)
nsubst,substep_sparse_zone
KBC,1
HROPT,FULL
HROUT,OFF
LUMPM,0
OUTPR,ALL,ALL,
LSWRITE,(i-1)*5+5,

NF_previous=NF_OC(1,i)
*enddo

total_substep=nmodes*(substep_cluster_zone+4*substep_sparse_zone)
total_ls=nmodes*5

LSSOLVE,1,total_ls,1,  !reads and solve multiple load steps
FINISH

/post26
/UI,COLL,1                    !activate specified GUI dialog boxes, collapse main menu after finish command
NUMVAR,200                    !number of variables allowed in POST26
SOLU,191,NCMIT    !enters the solution process
STORE,MERGE                   !stores data in the database for the defined variables
FILLDATA,191,,,,1,1           !fills a variable vy a ramp function

!--- voltage
nsol,200,1,VOLT,voltage !Specifies nodal data to be stored from the results !file.
!--- voltage amplitude
abs,2,200,,,volt_amp  !forms aqbsolute value of a variable,

!--- voltage phase
ATAN,199,200
FILLDATA,198,,,,3.1415926,0
QUOT,197,199,198
FILLDATA,196,,,,180,0
PROD,3,197,196,,volt_phase

!--- power
prod,198,2,2,,volt_amp_square
filldata,197,,,,Resistance,0
quot,4,198,197,,Power

!--- deflection
nsol,200,free_end_pt,U,Z,deflection
!--- deflection_amp
abs,5,200,,,defl_amp

!--- deflection phase
ATAN,199,200
FILLDATA,198,,,,3.1415926,0
QUOT,197,199,198
FILLDATA,196,,,,180,0
PROD,6,197,196,,defl_phase

!--- strain amplitude at top center
ANSOL,7,topc_pt,EPEL,X,e11
!--- deflection_amp
abs,8,7,,,e11_amp

!--- strain phase at top center
```

```
ATAN,199,7
FILLDATA,198,,,,3.1415926,0
QUOT,197,199,198
FILLDATA,196,,,,180,0
PROD,9,197,196,,e11_phase

*DIM,EXPORT_DATA,TABLE,total_substep,8
VGET,EXPORT_DATA(1,0),1
VGET,EXPORT_DATA(1,1),2
VGET,EXPORT_DATA(1,2),3
VGET,EXPORT_DATA(1,3),5
VGET,EXPORT_DATA(1,4),6
VGET,EXPORT_DATA(1,5),8
VGET,EXPORT_DATA(1,6),9
VGET,EXPORT_DATA(1,7),4

/OUTPUT,readings,'xls','.',append
*VWRITE, '**************','**************'
%14C%14C
*VWRITE, 'RLoad=',Resistance
%14C%10.3G
*VWRITE,'FREQ','volt_amp','voltage_phase','deflection_amp','deflection_phase','top_center_e11_amp','top_center_e11_phase','power
','curr_amp'
%14C %14C %14C %14C %14C %14C %14C  %14C  %14C
*VWRITE,EXPORT_DATA(1,0),EXPORT_DATA(1,1),EXPORT_DATA(1,2),EXPORT_DATA(1,3),EXPORT_DATA(1,4),EXPO
RT_DATA(1,5),EXPORT_DATA(1,6),EXPORT_DATA(1,7),EXPORT_DATA(1,8)
%14.5G %14.5G %14.5G %14.5G %14.5G %14.5G %14.5G %14.5G %14.5G
/OUTPUT,TERM
```